2011

A long breathing lean NOx trap for diesel after-treatment supplemental energy reduction

Marko Jeftic
University of Windsor

A LONG BREATHING LEAN NOX TRAP FOR DIESEL AFTER-TREATMENT SUPPLEMENTAL ENERGY REDUCTION

by

Marko Jeftić

A Thesis
Submitted to the Faculty of Graduate Studies
through the Department of Mechanical, Automotive, and Materials Engineering
in Partial Fulfillment of the Requirements for
the Degree of Master of Applied Science at the
University of Windsor

Windsor, Ontario, Canada

2011

Your file Votre référence
ISBN: 978-0-494-81739-1
Our file Notre référence
ISBN: 978-0-494-81739-1

AUTHOR'S DECLARATION OF ORIGINALITY

I hereby certify that I am the sole author of this thesis and that no part of this thesis has been published or submitted for publication.

I certify that, to the best of my knowledge, my thesis does not infringe upon anyone's copyright nor violate any proprietary rights and that any ideas, techniques, quotations, or any other material from the work of other people included in my thesis, published or otherwise, are fully acknowledged in accordance with the standard referencing practices. Furthermore, to the extent that I have included copyrighted material that surpasses the bounds of fair dealing within the meaning of the Canada Copyright Act, I certify that I have obtained written permission from the copyright owner(s) to include such material(s) in my thesis and have included copies of such copyright clearances to my appendix.

I declare that this is a true copy of my thesis, including any final revisions, as approved by my thesis committee and the Graduate Studies office, and that this thesis has not been submitted for a higher degree to any other University or Institution.

ABSTRACT

A long breathing strategy was investigated as a method for reducing the supplemental energy consumption of a diesel lean NOx trap (LNT). Empirical tests were performed on a heated flow bench set-up. The test results indicated that the LNT adsorption (breathing) time increased exponentially when the nitrogen oxide (NOx) level in the feed gas was reduced. Longer adsorptions led to supplemental energy savings due to less frequent LNT regeneration. In these tests, supplemental energy savings of over 70% were achieved with a long breathing LNT compared to a traditional LNT. Additional empirical tests investigated the concept of on-board hydrogen generation due to its potential benefits to an after-treatment system. The test findings revealed that the reformer temperature was a critical factor for on-board hydrogen generation. Further numerical and empirical tests revealed the benefits of utilizing a flow reversal system for hydrogen generation.

DEDICATION

To my parents with all my heart.

ACKNOWLEDGEMENTS

I would like to express a deep sense of gratitude towards my thesis advisors, Dr. Ming Zheng and Dr. Graham T. Reader. I am most thankful for the motivation, the direction, and the guidance they provided, without which this work would have been impossible.

I would like to thank the thesis committee members, Dr. Xiaohong Xu and Dr. Jimi Tjong, for giving me constructive criticism and helping me improve my thesis.

I am also grateful to all of my current and former colleagues at the Clean Diesel Engine Laboratory at the University of Windsor: Dr. Meiping Wang, Dr. Shui Yu, Xiaoye Han, Kelvin Xie, Dr. Usman Asad, Dr. Zhongwei Meng, Tongyang Gao, Yuyu Tan, Fangfang Lin, Prasad Divekar, Xiaoxi Zhang, Arturo Mendoza, Clemens Griebel, Michael Barkey, and Geraint Bryden.

I would like to acknowledge the University of Windsor staff members Bruce Durfy, Andrew Jenner, and Michael Charron for their help.

I would also like to thank the University of Windsor and the Ontario Ministry of Training, Colleges, and Universities for the funding support they provided. Additionally, all of the Clean Diesel Engine Laboratory sponsors: Auto21, the Natural Sciences and Engineering Research Council of Canada (NSERC), the Canada Research Chairs program (CRC), Canada Foundation for Innovation (CFI), Ontario Innovation Trust (OIT), and other industrial sponsors and OEM companies.

Ultimately, I would like to thank my parents for their support in every aspect and in every step of my life.

TABLE OF CONTENTS

LIST OF TABLES

LIST OF FIGURES

LIST OF ABBREVIATIONS

Uppercase

A	Cross Sectional Area (m^2)
AFR	Air-to-Fuel Ratio
CA	Crank Angle
CA50	Crank Angle of 50% Heat Released
CARB	California Air Resources Board
CLD	Chemiluminescence Detector
CO	Carbon Monoxide
DPF	Diesel Particulate Filter
DOC	Diesel Oxidation Catalyst
EGR	Exhaust Gas Recirculation
EPA	Environmental Protection Agency
FID	Flame Ionization Detector
FSN	Filter Smoke Number
FT-IR	Fourier Transform Infrared Spectroscopy
HSV	Hourly Space Velocity
IMEP	Indicated Mean Effective Pressure
ISO	International Organization for Standardization
LHV	Lower Heating Value
LNT	Lean NOx Trap
LTC	Low Temperature Combustion
M	Molar Mass (g/mol)

MAF	Mass Air Flow
NDIR	Non-dispersive Infrared Detector
NOx	Nitrogen Oxide(s)
Pinj	Injection Pressure
PM	Particulate Matter
POx	Partial Oxidation
SCR	Selective Catalytic Reduction
SR	Steam Reforming
T	Temperature
THC	Total Hydrocarbons
ULSD	Ultra Low Sulphur Diesel
V	Volume (m^3)
WGS	Water Gas Shift Reaction

Lowercase

bar abs	Absolute Pressure (bar)
c	Heat Capacity (J/kg·K)
c_h	Channel Hydraulic Diameter (m)
h	Convective Heat Transfer Coefficient ($W/m^2 \cdot K$)
k	Thermal Conductivity (W/m·K)
m	Mass (kg)
$\dot{m}$	Mass Flow Rate (kg/s)
ppm	Parts per Million
$\dot{q}$	Heat Generation (W)

rpm	Revolutions per Minute
t	Time (s)
x	Axial Dimension (m)

Greek

ε	Compression Ratio
λ	Excess Air Ratio
ρ	Density (kg/m^3)

Subscripts

ads_in	Cumulative NOx Mass Into the LNT during the Adsorption Phase
ads_slip	Cumulative NOx Slip Mass during the Adsorption Phase
g	Gas Phase
m	Axial Node Number
regen_in	Cumulative NOx Mass Into the LNT during the Regeneration Phase
regen_slip	Cumulative NOx Slip Mass during the Regeneration Phase
s	Solid Phase

Superscripts

n	Calculation Step

CHAPTER 1: INTRODUCTION

1.1 Objectives and Motivation

The main objective of this study was to utilize a long breathing lean NOx trap (LNT) to reduce the supplemental energy consumption of an LNT and thus attain a combined engine and after-treatment system with an overall lower fuel consumption. The motivation for this work originated from the reality that emission reducing strategies, such as low temperature combustion (LTC) and conventional LNTs, typically incur fuel consumption penalties [1,2] and have reduced the overall thermodynamic efficiency of the modern diesel engine (including after-treatment) compared to traditional diesel engines which did not require emission control.

In addition, it was proposed to investigate on-board hydrogen generation since literature [3,4] suggested that hydrogen could provide several benefits to an LNT, such as improved regeneration and desulfation efficiencies. Thus, an objective of this study was to investigate whether hydrogen can be generated with typical diesel exhaust conditions. Furthermore, a flow reversal reactor was proposed for improved on-board hydrogen generation. A summary of the objectives was as follows:

- Determine if the adsorption time of the LNT can be prolonged by reducing the nitrogen oxide (NOx) concentration in the feed gas
- Investigate if supplemental energy savings can be obtained with a long breathing LNT

- Compare the fuel consumption of the overall system (engine with after-treatment) of the long breathing strategy with that of the conventional LNT strategy and the low temperature combustion strategy
- Determine if hydrogen can be generated with typical diesel exhaust conditions
- Explore if using a flow reversal reactor could provide benefits for on-board hydrogen generation compared to a conventional unidirectional flow reactor

1.2 Emission Regulations

Increasing concerns about human health and environmental sustainability have led regulating bodies, such as the United States Environmental Protection Agency (EPA) and the California Air Resources Board (CARB), to impose emission regulations in an attempt to mitigate the environmental impacts of technology [5]. Consequently, the EPA enforced progressively stringent vehicle emission standards over the past couple of decades [6], particularly in the heavy duty sector as shown in Figure 1.1. In particular, the EPA demanded over 95% reductions in both nitrogen oxide (NOx) and particulate matter (PM) emissions for heavy duty on-highway vehicles from 1988 to 2010 [7]. EPA's stringent emissions standards presented a challenge for diesel engine manufacturers to develop technologies which would reduce the traditionally high diesel engine particulate matter and nitrogen oxide emissions [8].

Over the past couple of decades, engine manufacturers and research institutions typically focused on developing in-cylinder and after-treatment emission reducing technologies [9-13]. In-cylinder technologies included the use of exhaust gas recirculation (EGR), different kinds of fuels, dual fuels, and advanced fuel injection

systems. After-treatment technologies included the diesel particulate filter (DPF), selective catalytic reduction (SCR), and the lean NOx trap. The lean NOx trap was the focus of this study.

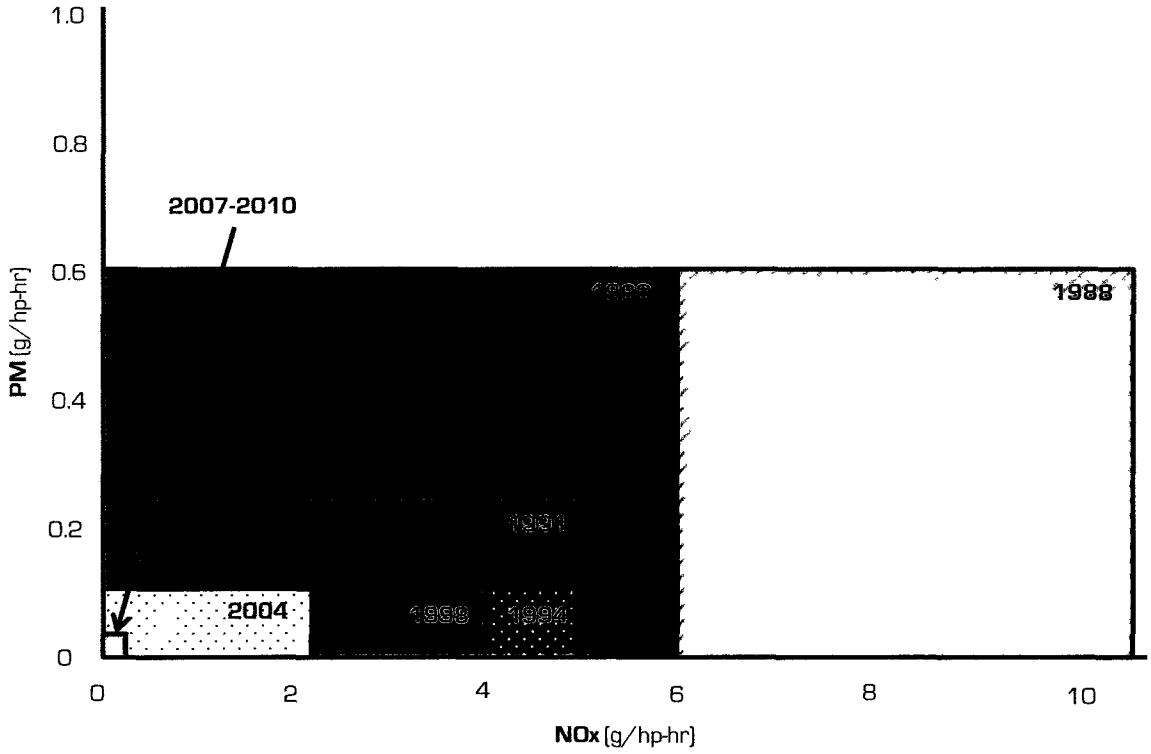

Figure 1.1: EPA's Heavy Duty Diesel On-Highway Emission Standards [7]

1.3 Lean NOx Trap

A lean NOx trap is a diesel deNOx after-treatment device which operates on periodic cycling of lean adsorption and fuel-rich regeneration [1]. Typical LNT cycle times for engine-out NOx levels of a couple of hundred parts per million (ppm) are on the order of one minute of lean adsorption and ten seconds of fuel-rich regeneration [1,14] but lean adsorption cycles as short as 20 seconds have been proposed [1]. During lean operation (Figure 1.2), the LNT operates in the adsorption mode, also referred to as the

storage, the breathing, or the trapping mode. In the adsorption mode, NOx passes through the LNT and reacts with a metal oxide (barium oxide (BaO) will be used as an example henceforth) to form barium nitrate ($Ba(NO_3)_2$) [14]. At optimum conditions, over 90% of NOx can be trapped in the LNT as a nitrate while the remainder slips through the LNT. However, as the barium sites saturate with nitrates, more and more NOx slips through the LNT and the NOx storage efficiency declines.

To free up the barium sites, the LNT must undergo fuel-rich regeneration as shown in Figure 1.3. During this time, supplemental fuel is provided either through late in-cylinder post injection or through supplemental exhaust fuel injection [1,14]. The fuel is typically a hydrocarbon fuel since it is readily available on-board a vehicle. Under fuel-rich conditions, the LNT experiences increased temperatures and with the help of a catalyst, usually of precious metal, the nitrates are released from the barium and reduced to nitrogen (N_2) while the barium is restored to barium oxide [3]. However, not all of the nitrates reduce to nitrogen, some slips through as NOx. The regeneration efficiency of an LNT is below 100%, usually in the range above 80% if the process occurs at optimum conditions.

Therefore, the use of an LNT is associated with an energy penalty due to the use of supplemental fuel for LNT regeneration [1]. The focus of this study was to investigate a strategy for reducing the supplemental energy requirements of an LNT. The strategy for the LNT supplemental energy reduction was centred on the concept of a long breathing LNT.

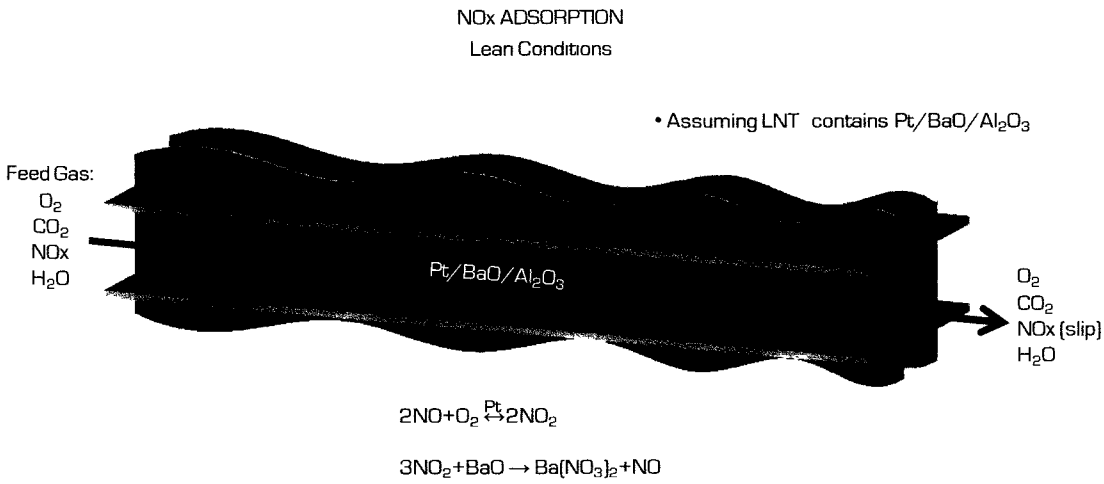

Figure 1.2: LNT Basic Reaction Chemistry during Adsorption

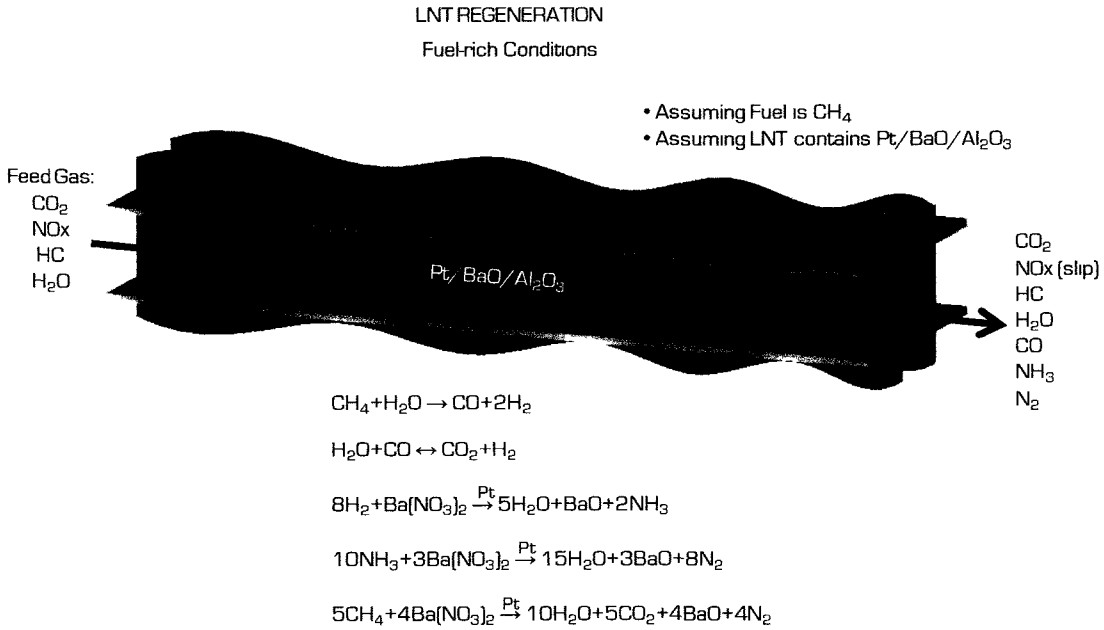

Figure 1.3: LNT Basic Reaction Chemistry during Regeneration

1.4 Long Breathing LNT

A long breathing LNT is an LNT which has a prolonged adsorption cycle compared to traditional LNTs. The prolonged adsorption (breathing) time of the LNT

would be enabled by the application of in-cylinder technologies such as exhaust gas recirculation. As mentioned earlier, the typical lean-rich cycle time for a conventional LNT exposed to hundreds of ppm of NOx is of the order of one minute for lean adsorption and ten seconds for rich regeneration. It was proposed that through moderate EGR application, the engine-out NOx could be reduced to below 100 ppm, thereby reducing the NOx input to the LNT and extending the adsorption time of the LNT. With this method, the rich regeneration would occur less frequently and thus the periodic use of supplemental fuel would be reduced.

To demonstrate an example for suitable application of a long breathing LNT, engine tests were done on a diesel test engine (specifications given in Table 4.1). The results (Figure 1.4) showed that at low EGR levels, the engine-out NOx were on the order of hundreds of ppm and a conventional LNT would be required to satisfy the EPA's diesel heavy duty on-highway emission regulations and the associated LNT fuel penalty would be incurred. When high levels of EGR were applied, low temperature combustion was achieved and NOx and soot emissions were reduced to simultaneously low levels, capable of satisfying the EPA's heavy duty on-highway emission regulations without after-treatment. However, with LTC there was a significant increase in carbon monoxide (CO) and hydrocarbon (THC) emissions (Figure 1.6) which was an indication of poor thermal efficiency. Thus, both the conventional LNT and the low temperature combustion strategies incurred a fuel consumption penalty. A long breathing LNT with moderate EGR application was proposed for achieving simultaneously low NOx and soot while reducing the overall fuel consumption of the combined engine and after-treatment

system. A long breathing LNT would be more fuel efficient than a conventional LNT due to less frequent fuel-rich regeneration.

With moderate EGR application, the engine-out NOx were reduced to a range of 40 ppm to 70 ppm (Figure 1.4) while the soot was below the DPF tolerant limit of 2.5 filter smoke number (FSN) (Figure 1.5). More importantly, with moderate EGR levels, the high THC penalty was not incurred as with LTC (Figure 1.6). Since moderate EGR application was not capable of reducing NOx to low enough levels to meet the EPA's heavy duty emission regulations, a long breathing lean NOx trap was proposed as the technology for further NOx reduction.

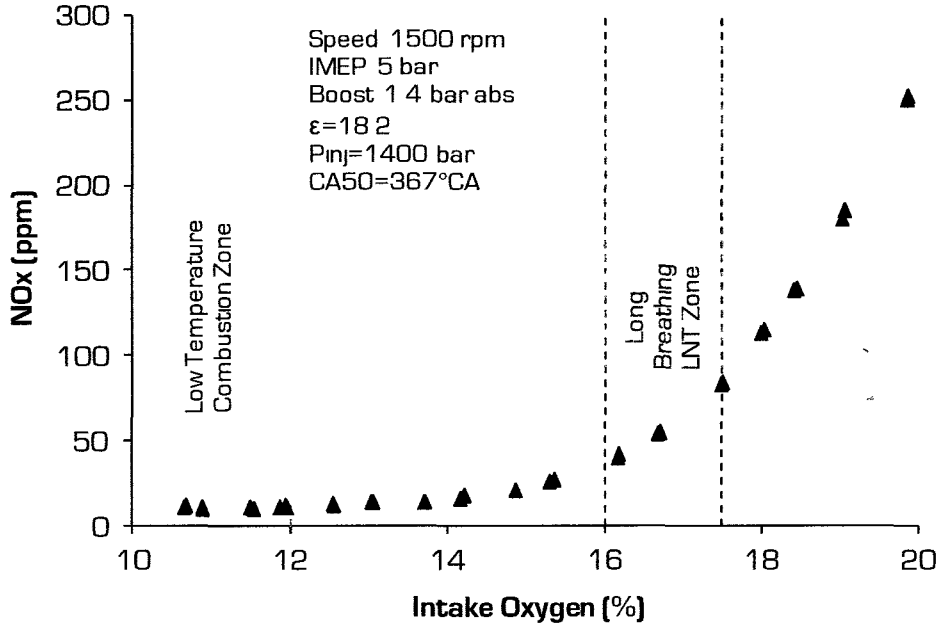

Figure 1.4: Effects of EGR Application on NOx Emissions

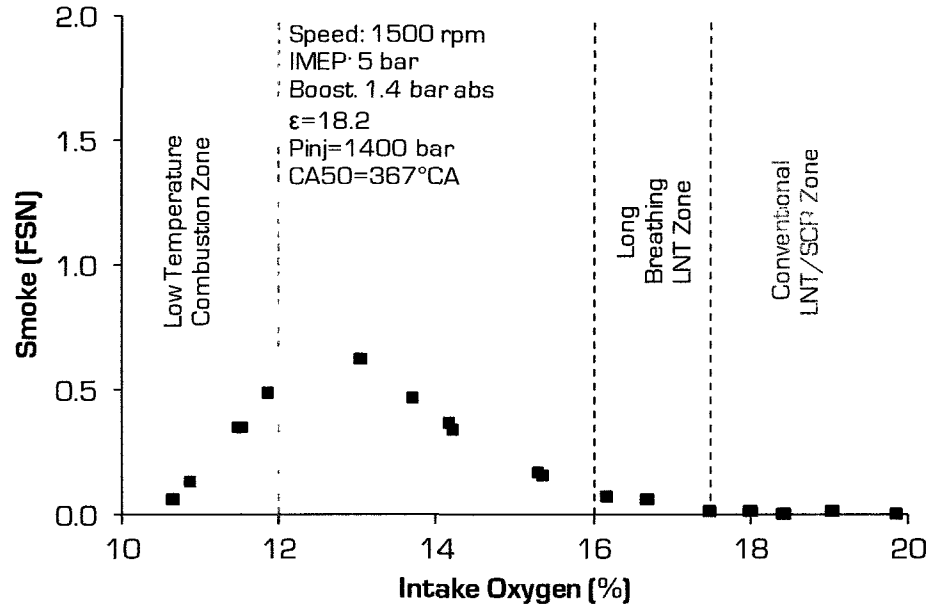

Figure 1.5: Effects of EGR Application on Soot Emissions

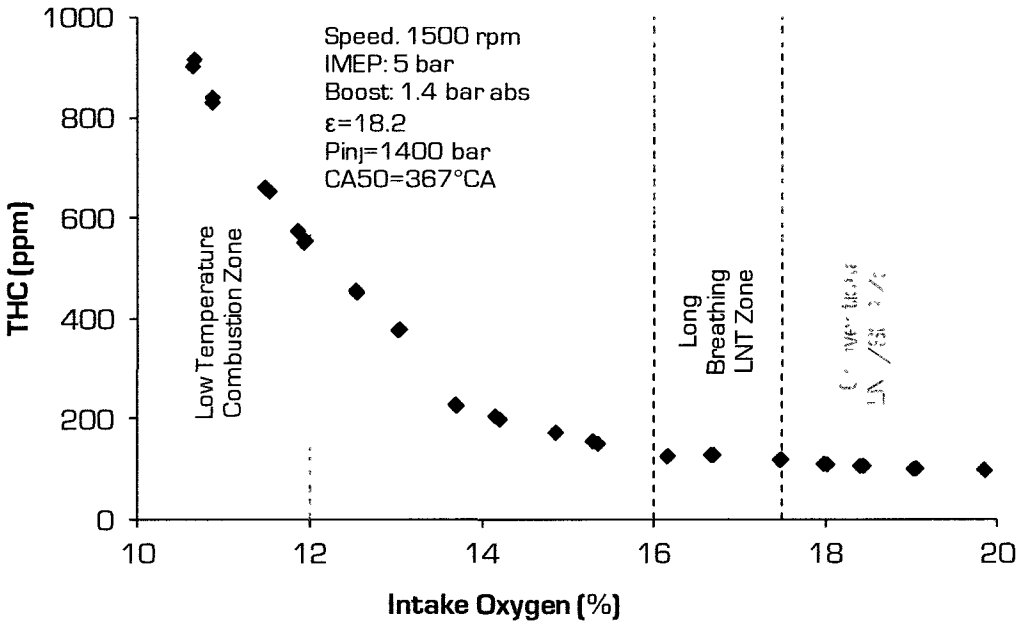

Figure 1.6: Effects of EGR Application on THC Emissions

With NOx in the range of 40 ppm to 70 ppm, the work load of an LNT installed downstream of the engine would have been reduced compared to levels of several

hundreds of ppm of NOx if EGR was not applied. It was hypothesized that with reduced engine-out NOx levels, the LNT lean adsorption time would be longer and the saturation of the barium sites would be much slower. This would lead to a less frequent need for rich regeneration of the LNT and the supplemental fuel addition for the LNT would be reduced.

1.5 On-board Hydrogen Generation

The benefits of hydrogen fuel for deNOx after-treatment have been discussed in numerous studies [3,4,15-18]. Hydrogen presence during the LNT desulfation was concluded to be of critical importance for removing unwanted sulphur compounds from barium containing storage catalysts [4]. It was observed in [4] that catalyst desulfation was only effective if either water or hydrogen were present; water being capable of producing hydrogen via the water gas shift reaction (WGS). In the absence of both, sulphur was not removed. Hydrogen was described in [17] as a more capable reductant of NOx during the LNT regeneration process. In [17] it was noticed that the location of the largest reduction of NOx in the LNT coincided with the location of the highest hydrogen depletion. The study in [18] compared the use of hydrogen with the use of diesel fuel for LNT NOx reduction and the results showed a superior performance with hydrogen as the reductant. With hydrogen, a higher overall NOx conversion efficiency was achieved compared to diesel based reduction. Also, hydrogen based NOx reduction was capable of achieving high NOx conversion efficiencies even at low diesel exhaust temperatures, as low as 145°C, at which diesel based NOx reduction was not effective at all.

Due to the challenges of on-board hydrogen storage, extensive research has been done on the topic of on-board hydrogen generation [19,20]. On-board hydrogen generation can be achieved by utilizing catalytic reactors in the exhaust stream. With the help of a catalyst, hydrogen can be produced on-board a vehicle through various reaction mechanisms such as partial oxidation (POx), steam reforming (SR), and the water gas shift reaction.

In steam reforming, hydrogen is produced when high temperature steam reacts with a hydrocarbon fuel to produce hydrogen and carbon monoxide [21] as shown in Equation 1.1. Steam reforming is considered a high yielding hydrogen reaction because it has the highest hydrogen to carbon monoxide yield ratio of all the reaction mechanisms. Steam reforming is frequently used in the industry and there is a lot of familiarity with its use [22,23]. However, since steam reforming is an endothermic reaction, it requires energy addition [21,22]. This potentially makes the steam reforming reaction less energy efficient than the exothermic reaction mechanisms. Also, steam reforming typically requires the use of a catalyst and care must be used to prevent catalyst poisoning and deactivation [22]. Overall, steam reforming has a high potential for producing hydrogen.

$$\text{Steam Reforming: } C_\alpha H_\beta + \alpha H_2O \rightarrow \alpha CO + \left(\alpha + \frac{\beta}{2}\right) H_2 \qquad (1.1)$$

Another common reaction for hydrogen production is partial oxidation. In partial oxidation, oxygen reacts with a hydrocarbon fuel to produce carbon monoxide and hydrogen as shown in Equation 1.2. This reaction mechanism is especially suitable for lean burn engines because they have oxygen readily available in the exhaust. Partial

oxidation can be achieved even without a catalyst; however, this typically occurs only at extremely high temperatures such as between 1300°C-1500°C [22].

$$\text{Partial Oxidation: } C_\alpha H_\beta + \frac{\alpha}{2} O_2 \rightarrow \alpha CO + \frac{\beta}{2} H_2 \qquad (1.2)$$

By comparing the balanced equations for SR and POx, it can be seen that the partial oxidation reaction has a lower hydrogen to carbon monoxide yield ratio than the steam reforming reaction. However, in contrast to the steam reforming reaction, partial oxidation is an exothermic reaction and therefore it does not require additional energy to be supplied. To generate hydrogen with partial oxidation, the temperature and the oxygen content have to be controlled to prevent complete oxidation from occurring [21] which would not yield any hydrogen as shown in Equation 1.3.

$$\text{Complete Oxidation: } C_\alpha H_\beta + \left(\alpha + \frac{\beta}{4}\right) O_2 \rightarrow \alpha CO_2 + \frac{\beta}{2} H_2 O \qquad (1.3)$$

Autothermal reforming is a combination of the steam reforming and the partial oxidation reactions [22,23]. With autothermal reforming both steam and oxygen react with a hydrocarbon fuel to generate carbon monoxide and hydrogen as shown in Equation 1.4. In autothermal reforming the additional energy required by the steam reforming reaction is supplied by the partial oxidation reaction and the net result is a slightly exothermic autothermal reforming reaction [22,23]. The theoretical hydrogen to carbon monoxide yield ratio is lower than steam reforming but higher than partial oxidation. A catalyst is required to promote the reaction. Autothermal reforming is a relatively new concept and there is not as much industrial experience as with the partial oxidation and steam reforming reactions [22].

$$\text{Autothermal Reforming: } C_\alpha H_\beta + \frac{\alpha}{2} H_2 O + \frac{\alpha}{4} O_2 \rightarrow \alpha CO + \left(\frac{\alpha}{2} + \frac{\beta}{2}\right) H_2 \qquad (1.4)$$

Another hydrocarbon based reaction is the dry reforming reaction. In dry reforming, a hydrocarbon fuel reacts with carbon dioxide to generate carbon monoxide and hydrogen as shown in Equation 1.5. By comparing the balanced equation with the previous hydrocarbon based reaction mechanisms, it is apparent that dry reforming has the lowest hydrogen to carbon monoxide yield ratio. This reaction also requires the use of a catalyst and very high reaction temperatures, in excess of 800°C [21]. With this reaction, there is also a tendency for high carbon deposits to occur and this tends to reduce the effectiveness of the catalyst [24,25]. These challenges, along with the low hydrogen to carbon monoxide yield ratio, make dry reforming a less desired reaction mechanism for hydrogen production.

$$\text{Dry Reforming: } C_\alpha H_\beta + \alpha CO_2 \rightarrow 2\alpha CO + \frac{\beta}{2} H_2 \qquad (1.5)$$

The water gas shift reaction (Equation 1.6) is a hydrogen producing reaction which does not require the use of hydrocarbon fuel. In this reaction, carbon monoxide and steam react with the help of a catalyst to produce carbon dioxide and hydrogen [21,22]. The catalyst is typically copper, iron, molybdenum, palladium, or platinum based [22]. The reaction is slightly exothermic so it does not require additional energy to be supplied [22]. Because carbon monoxide is generated by the partial oxidation and the steam reforming reactions, it is a common practice to install a downstream water gas shift reactor which would utilize the produced carbon monoxide as a reactant for producing hydrogen [22]. The main challenge with the water gas shift reaction is that it is a reversible reaction. If the reaction conditions are not controlled, specifically the temperature, the reverse reaction could be more favoured than the forward reaction [22]. This would be highly undesirable for hydrogen production since the reverse reaction

would consume hydrogen to generate water. Thus, the upper limit of the temperature is usually limited to approximately 750°C [21].

$$\text{Water Gas Shift: } CO+H_2O \leftrightarrow CO_2+H_2 \qquad (1.6)$$

Due to the previously described benefits of hydrogen for an LNT, it was decided to investigate whether hydrogen generation would be possible on-board a diesel vehicle under typical diesel exhaust conditions. Thus, tests investigated the effects of various exhaust gas parameters, such as temperature and hourly space velocity (HSV), on the hydrogen yield of an unoptimized DOC reactor. If the results show that hydrogen generation is possible, it is suggested for future work to design a more optimized reactor and to combine on-board hydrogen generation with a long breathing LNT.

1.6 Flow Reversal

On-board hydrogen generation from practical diesel fuels typically requires temperatures in the range of 500°C to over 1000°C. However, diesel engine exhaust temperatures often fluctuate and can be as low as 200°C. Additional energy would have to be supplied to maintain the fuel reformer at a suitable temperature range for on-board hydrogen generation. A standard method would be to supply supplemental fuel which would combust inside the reactor and thus raise the reactor temperature. However, the oxidation of most diesel fuels would be difficult at temperatures as low as 200°C.

Flow reversal can be used as a method to prevent the quick cooling down of a reactor. By periodically alternating the flow direction through the reactor, a temperature trap is created in its central portion. This enables the central section of the reactor to remain at elevated temperatures when the reactor is exposed to a cold feed gas. Thus,

with flow reversal, the reactor temperature generally becomes less sensitive to the feed gas temperature [26,27]. The flow direction through the reactor is typically controlled by a valve as shown in Figure 1.7. The temperature retention ability of a flow reversal system could be of benefit for on-board hydrogen generation where high temperatures are typically required. Therefore, empirical and numerical tests were done to compare the temperature response of a flow reversal reactor and a conventional unidirectional flow reactor.

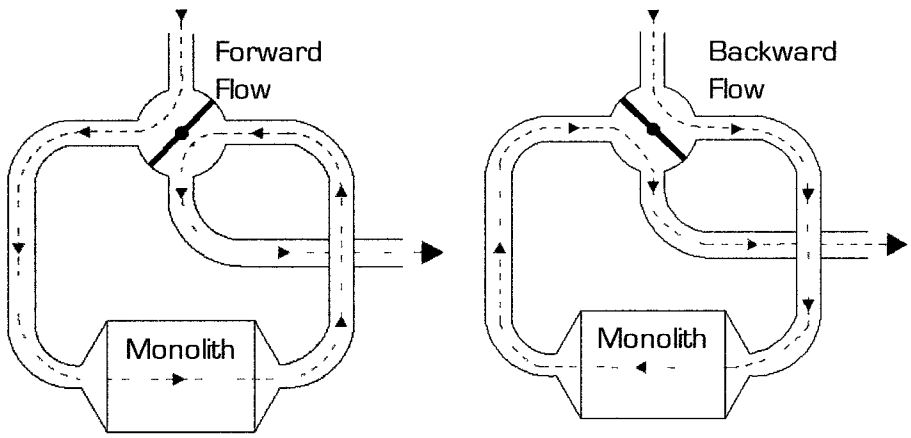

Figure 1.7: Valve Controlled Flow Reversal

CHAPTER 2: TEST OUTLINE

Figure 2.1 illustrates the general test outline while Table 2.1 and Table 2.2 summarize the basic test conditions for the long breathing LNT, the hydrogen generation, and the empirical flow reversal tests. Test 1 and Test 2 investigated the validity of the long breathing LNT concept by measuring the LNT adsorption time with respect to different levels of NOx in the feed gas. Due to expediency reasons, the feed gas was a simple composition of air mixed with NOx. The NOx was composed of 99.5% nitrogen monoxide (NO) and 0.5% nitrogen dioxide (NO_2). Three different NOx levels were chosen according to the engine test results shown in Figure 1.4: 110 ppm corresponding to low EGR and conventional LNT application; 70 ppm corresponding to moderate EGR and the upper NOx limit of the long breathing LNT range; and 50 ppm corresponding to moderate EGR application and a mid-range value of the long breathing LNT range.

The LNT temperature was maintained at 300°C and the hourly space velocity at 90,000. These values were chosen in consideration of the equipment capability and of the typical diesel exhaust gas conditions. Also, literature [28] suggested that a high NOx storage efficiency could be obtained at 300°C. For LNT regeneration, a ten second fuel injection at a λ of 0.7 was utilized. These values were chosen as initial unoptimized values. It should be noted that in these and in subsequent tests the regeneration strategy, the LNT catalyst, and the test process were primitive and unoptimized since the focus of these tests was not on obtaining optimal results but on determining whether the long breathing LNT concept was valid or not.

Test 3 and Test 4 explored the validity of the long breathing LNT concept with a feed gas simulating diesel exhaust gas. This was achieved by adding 8.5% carbon

dioxide and 6% water to the LNT feed gas. The LNT temperature was kept at 300°C but the hourly space velocity was reduced from 90,000 to 75,000. The HSV was reduced to conserve resources while still maintaining it in a range representative of a typical diesel exhaust condition. For the regeneration, the ten second fuel injection strategy was changed to fifteen seconds because results in Test 11 indicated that a longer fuel injection duration generated more hydrogen which could be beneficial in terms of the NOx conversion efficiency. Also, the λ value was changed from 0.7 to 0.82 because the air-to-fuel ratio sweep in Test 8 indicated that the maximum hydrogen yield was achieved with λ=0.82. Test 5 measured the adsorption time of an LNT exposed to 300 ppm of NOx. This was chosen as a representative condition for a traditional LNT strategy where the LNT is exposed to hundreds of ppm of NOx.

The effects of hourly space velocity on the adsorption time of a long breathing LNT were studied in Test 6. The LNT temperature was constant at 300°C while the HSV was varied from 75,000 to 120,000. The lower limit of the HSV range was restricted to 75,000 because the flow bench heater was not able to maintain a 300°C below an HSV of 75,000. The upper limit of the HSV range was chosen as 120,000 to conserve consumable resources such as CO_2 and NOx. In Test 7, the adsorption time was measured while the LNT temperature was varied from 190°C to 310°C. The upper limit of the temperature range was limited due to the flow bench heater capabilities. The lower limit was chosen as 190°C based on the typical diesel exhaust temperature range.

Literature suggested that the LNT regeneration and desulfation efficiencies could be improved by using hydrogen as a reductant. Thus, hydrogen generation with an unoptimized DOC reactor was explored. The DOC was installed on the flow bench

system and hydrogen generation tests were done to investigate the effects of the DOC temperature, the hourly space velocity, the air-to-fuel ratio, and the fuel injection duration on the hydrogen yield of the DOC. The hydrogen generation tests were not concerned with achieving high hydrogen yields but rather on determining if hydrogen could be generated under typical diesel exhaust conditions. High hydrogen yields, in excess of 3.75%, were actually undesirable due to the possible danger of hydrogen reacting with oxygen and causing unexpected and uncontrolled combustion. Therefore, the hydrogen level was measured and carefully monitored throughout the tests.

Test 8 explored the effect of the air-to-fuel ratio on hydrogen yield. The reactor was maintained at a constant temperature of 300°C. This temperature was chosen as a representative diesel exhaust temperature while considering the capabilities of the flow bench heater. The hourly space velocity was kept constant at 130,000. The excess air ratio was varied from 0.54 to 1.11. The upper limit was chosen as slightly lean because on-board hydrogen generation typically requires rich air-to-fuel ratios but one slightly lean test point was chosen to observe if any hydrogen would be generated under lean conditions. The lower limit was chosen as 0.54 due to the fuel injector calibration.

An on-board hydrogen generation temperature sweep was done in Test 9. The temperature range was from 257°C to 373°C. The lower temperature limit was chosen as 257°C because it was observed that the diesel fuel did not combust below this temperature and no hydrogen was generated. The upper temperature limit was selected based on the maximum temperature output of the flow bench heater. The HSV was kept constant at 130,000. This value was chosen because the flow bench heater was not able to generate temperatures above 350°C at lower space velocities.

The effect of HSV on hydrogen yield was studied in Test 10. A steady reactor temperature of 300°C was selected as a representative diesel exhaust temperature. The HSV was varied from 75,000 to 130,000. The lower limit was chosen as 75,000 because the flow bench heater could not maintain a 300°C reactor temperature below an HSV of 75,000. The upper value of 130,000 was chosen to conserve consumable resources such as bottled carbon dioxide and nitrogen.

In Test 11, the effect of the fuel injection duration on the hydrogen generation at a constant reactor temperature and three different HSV was investigated. The reactor temperature was kept constant at 300°C while the HSV was adjusted from 75,000 to 115,000. The fuel injection duration was selected as ten or fifteen seconds. The upper limit was selected as fifteen seconds due to concerns of generating reactor temperatures in excess of 1000°C and thermally damaging the hardware. For the same reason the HSV was limited to 115,000.

Flow reversal tests (Test 12) were done to compare the temperature response of a flow reversal reactor and a conventional unidirectional flow reactor. In this test, a cold reactor was heated by a warm feed gas. Heating values of 200 W and 500 W were selected as representative results from a broader testing range which extended from 100 W to 700 W. The maximum heating capacity of the heaters was 700 W. Air was chosen as the feed gas for expediency. The flow rate was selected as 2 g/s and the flow reversal time was selected as 10 seconds as initial unoptimized values. The purpose of these tests was to confirm the numerical test trends. Optimization is suggested for future tests.

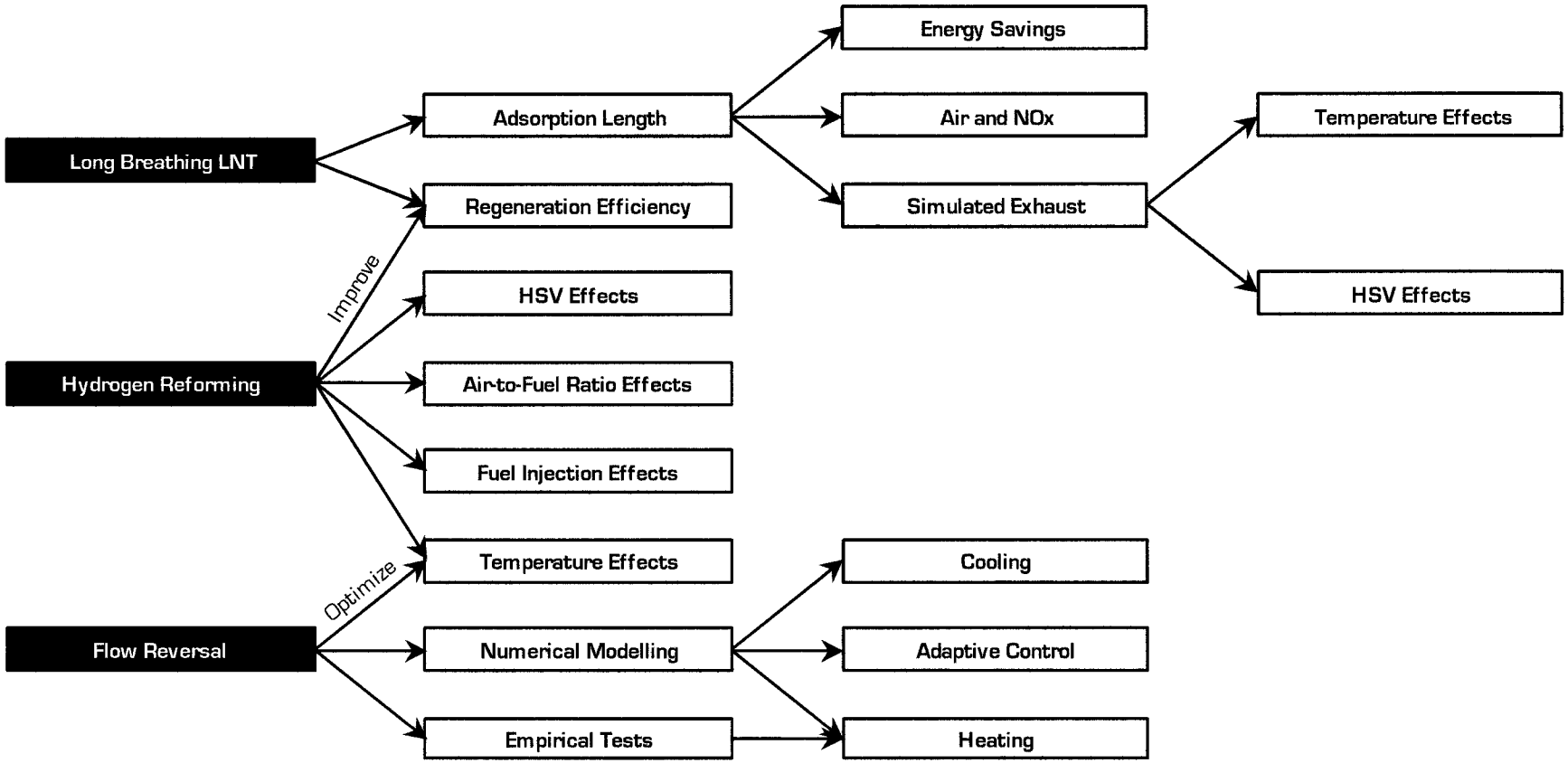

Figure 2.1: Block Diagram of the Test Outline

Table 2.1: Outline of the Long Breathing LNT and the Hydrogen Generation Tests

Test	Reactor Temp.	HSV	λ	Fuel Injection	Feed Gas Composition			
					NOx	CO_2	O_2	Water
	°C	$h^{-1} \cdot 10^3$		seconds	ppm	%	%	%
1 Long Breathing with Air & NOx	300	90	0.70	10	110	0	21	0
	300	90	0.70	10	70	0	21	0
	300	90	0.70	10	50	0	21	0
2 Long Breathing with Air & NOx	300	90	0.70	10	80	0	21	0
Confirmation Tests	300	90	0.70	10	60	0	21	0
	300	90	0.70	10	50	0	21	0
	300	90	0.70	10	40	0	21	0
	300	90	0.70	10	30	0	21	0
	300	90	0.70	10	30	0	21	0
3 Long Breathing with Simulated	300	75	0.82	10	110	8.5	17	6
Exhaust Gas	300	75	0.82	10	70	8.5	17	6
	300	75	0.82	10	50	8.5	17	6
4 Long Breathing Repeatability	300	75	0.82	15	110	8.5	17	6
Test	300	75	0.82	15	70	8.5	17	6
	300	75	0.82	15	50	8.5	17	6
5 High NOx Test	300	75	0.82	15	300	8.5	17	6
6 Long Breathing HSV Sweep	300	75	0.82	15	50	8.5	17	6
	300	90	0.82	15	50	8.5	17	6
	300	105	0.82	15	50	8.5	17	6
	300	120	0.82	15	50	8.5	17	6
7 Long Breathing Temperature	190	105	0.82	15	50	8.5	17	6
Sweep	235	105	0.82	15	50	8.5	17	6
	265	105	0.82	15	50	8.5	17	6
	290	105	0.82	15	50	8.5	17	6
	300	105	0.82	15	50	8.5	17	6
	310	105	0.82	15	50	8.5	17	6
8 Hydrogen Generation AFR	300	130	0.54	10	0	8.5	16	6
Sweep	300	130	0.72	10	0	8.5	16	6
	300	130	0.82	10	0	8.5	16	6
	300	130	0.92	10	0	8.5	16	6
	300	130	1.11	10	0	8.5	16	6
9 Hydrogen Generation	257	130	0.82	10	0	8.6	16	6
Temperature Sweep	275	130	0.82	10	0	8.5	16	6
	296	130	0.82	10	0	8.5	16	6
	310	130	0.82	10	0	8.5	16	6
	311	130	0.82	10	0	8.5	16	6
	311	130	0.82	10	0	8.5	16	6
	324	130	0.82	10	0	8.5	16	6
	351	130	0.82	10	0	8.5	16	6
	373	130	0.82	10	0	8.5	16	6
10 Hydrogen Generation HSV	300	75	0.82	10	0	8.5	16	6
Sweep	300	100	0.82	10	0	8.5	16	6
	300	115	0.82	10	0	8.5	16	6
	300	130	0.82	10	0	8.5	16	6
	300	130	0.82	10	0	8.5	16	6
11 Hydrogen Generation Fuel	300	115	0.82	10	0	8.5	16	6
Injection Duration Test	300	100	0.82	10	0	8.5	16	6
	300	75	0.82	10	0	8.5	16	6
	300	115	0.82	15	0	8.5	16	6
	300	100	0.82	15	0	8.5	16	6
	300	75	0.82	15	0	8.5	16	6

Table 2.2: Outline of the Empirical Flow Reversal Tests

					Feed Gas Composition			
	Temperature	Flow Rate	Heater Power	Reversal Time	NOx	CO_2	O_2	Water
	°C	g/s	W	s	ppm	%	%	%
12 Flow Reversal Tests	25	2	200	0	0	0	21	0
	25	2	200	10	0	0	21	0
	25	2	500	0	0	0	21	0
	25	2	500	10	0	0	21	0

CHAPTER 3: EXPERIMENTAL SET-UP

3.1 Flow Bench Set-up

All of the tests shown in Table 2.1 and Table 2.2 were done on a flow bench set-up. The schematic diagrams of the test set-up for each of the tests are shown in Figure 3.1 through Figure 3.5. In all of the tests, the feed gas was heated by a Leister Hot Air Tool heater which was capable of providing steady outlet gas temperatures. The maximum temperature output of the heater was dependant on the mass flow rate of the feed gas; at higher mass flow rates the heater was capable of heating the feed gas to higher temperatures. The mass flow rate of the feed gas was measured by a mass air flow (MAF) sensor which was installed upstream of the heater. The MAF sensor was a Bosch model 0281002619. It was intended to also use a high precision orifice flow meter to measure the mass flow rate. An orifice flow meter was designed according to the ISO 5167-2:2003 standard. However, the orifice flow meter required rigorous machining requirements and the machining was not completed in time for these tests. The orifice flow meter design is reported in the appendix.

The various feed gas mixtures were obtained from a compressed air supply available at the Clean Diesel Engine Laboratory and nitrogen oxide, carbon dioxide, and nitrogen gas cylinder tanks from Praxair. The flow was controlled through a series of pressure regulators to provide a steady flow to the system. An NGK NTK 22010 oxygen sensor was installed downstream of the LNT/DOC to provide information about whether the gas mixture was rich or lean; a fuel-rich mixture was essential for LNT regeneration. Omega k-type thermocouples were used for temperature measurements.

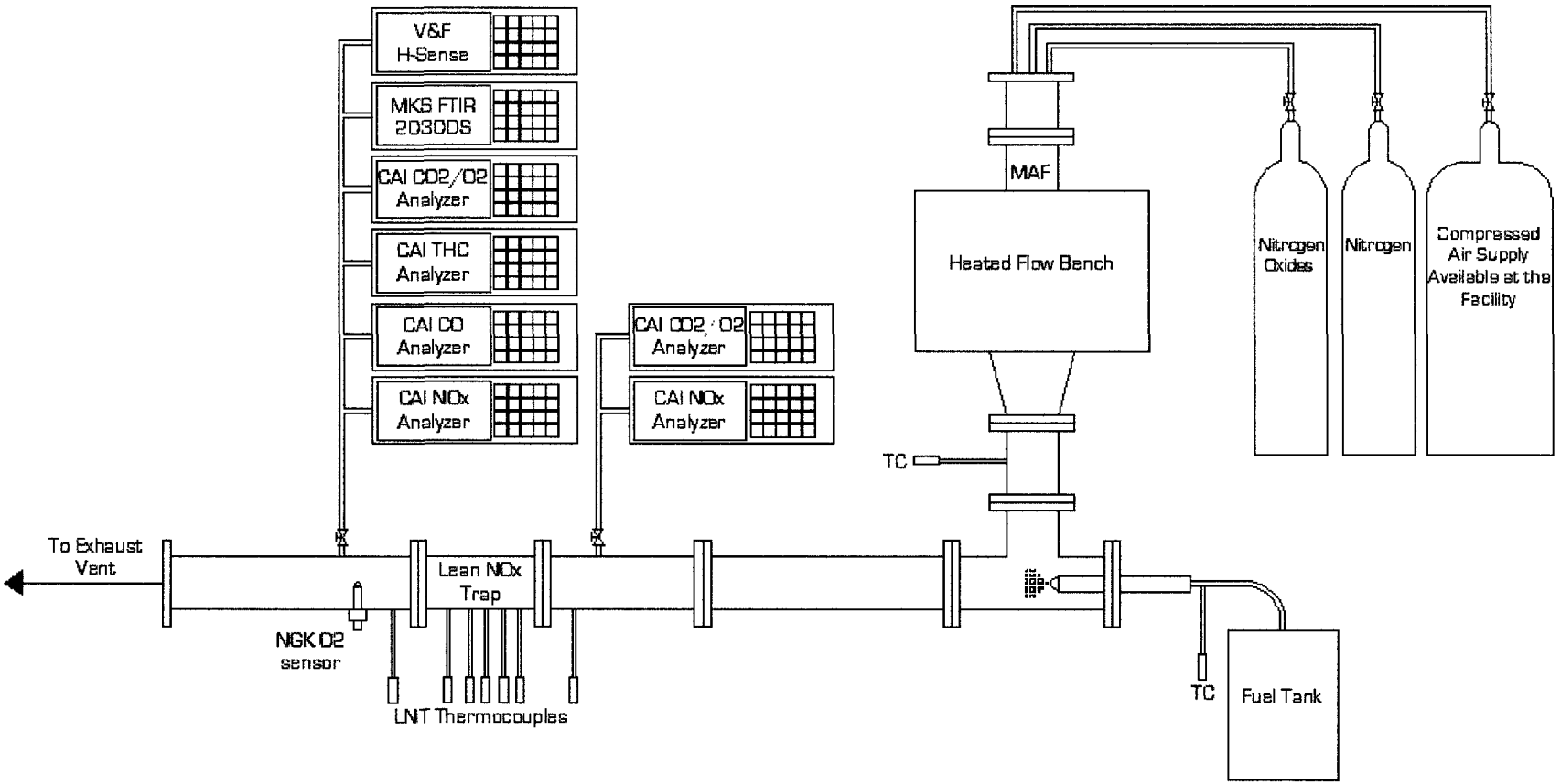

Figure 3.1: Schematic Diagram of the Experimental Set-up for Test 1 and Test 2

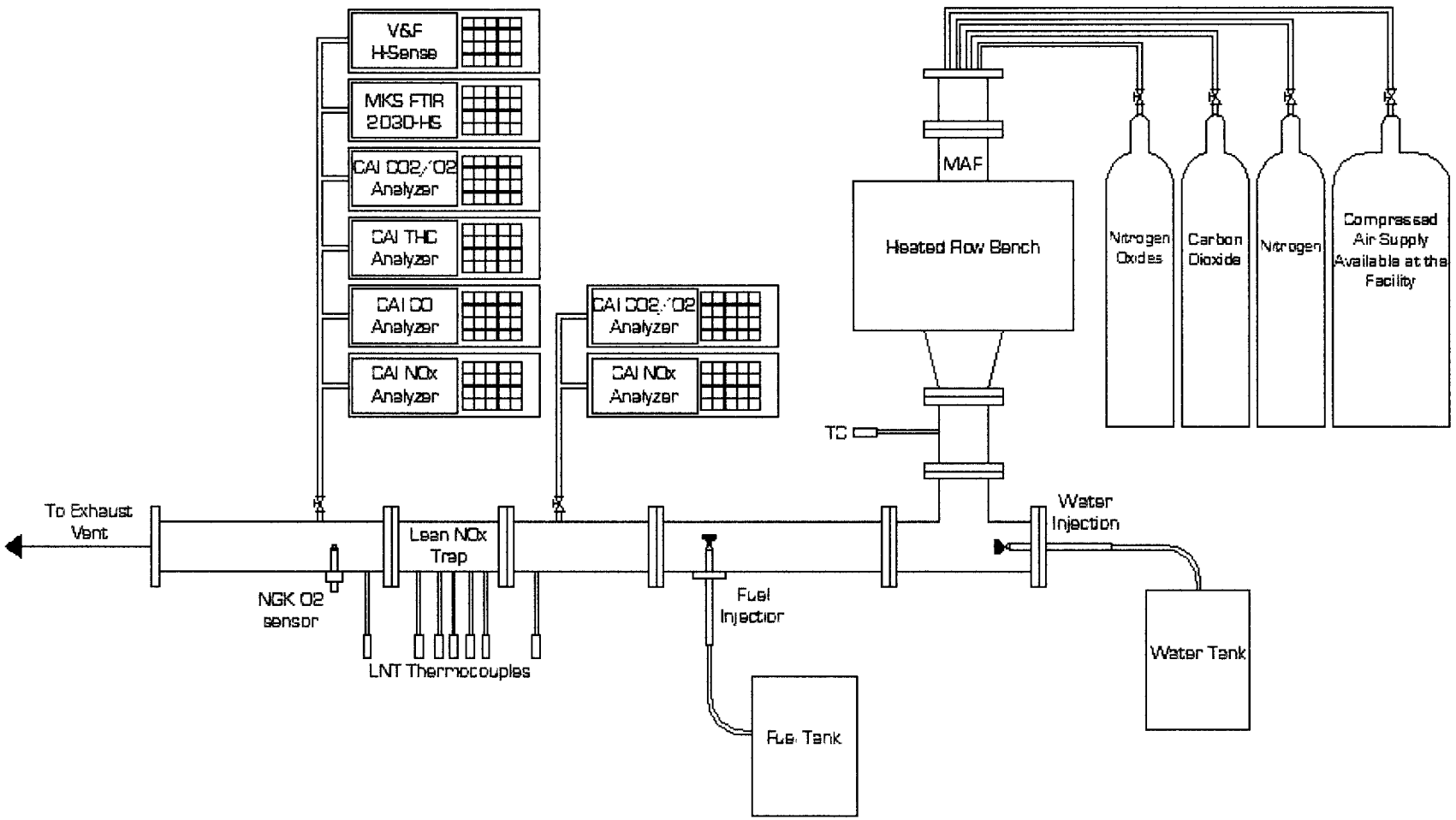

Figure 3.2: Schematic Diagram of the Experimental Set-up for Test 3

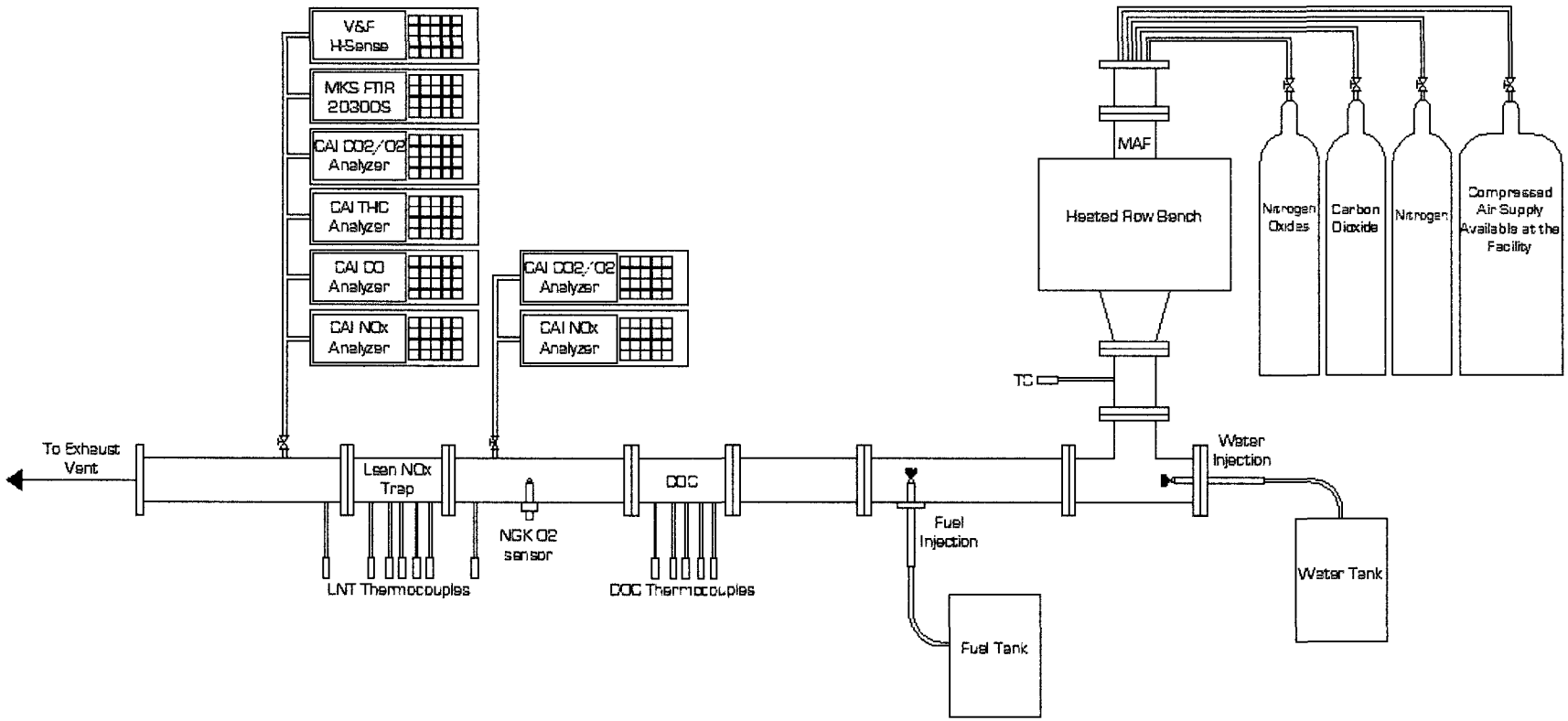

Figure 3.3: Schematic Diagram of the Experimental Set-up for Tests 4-7

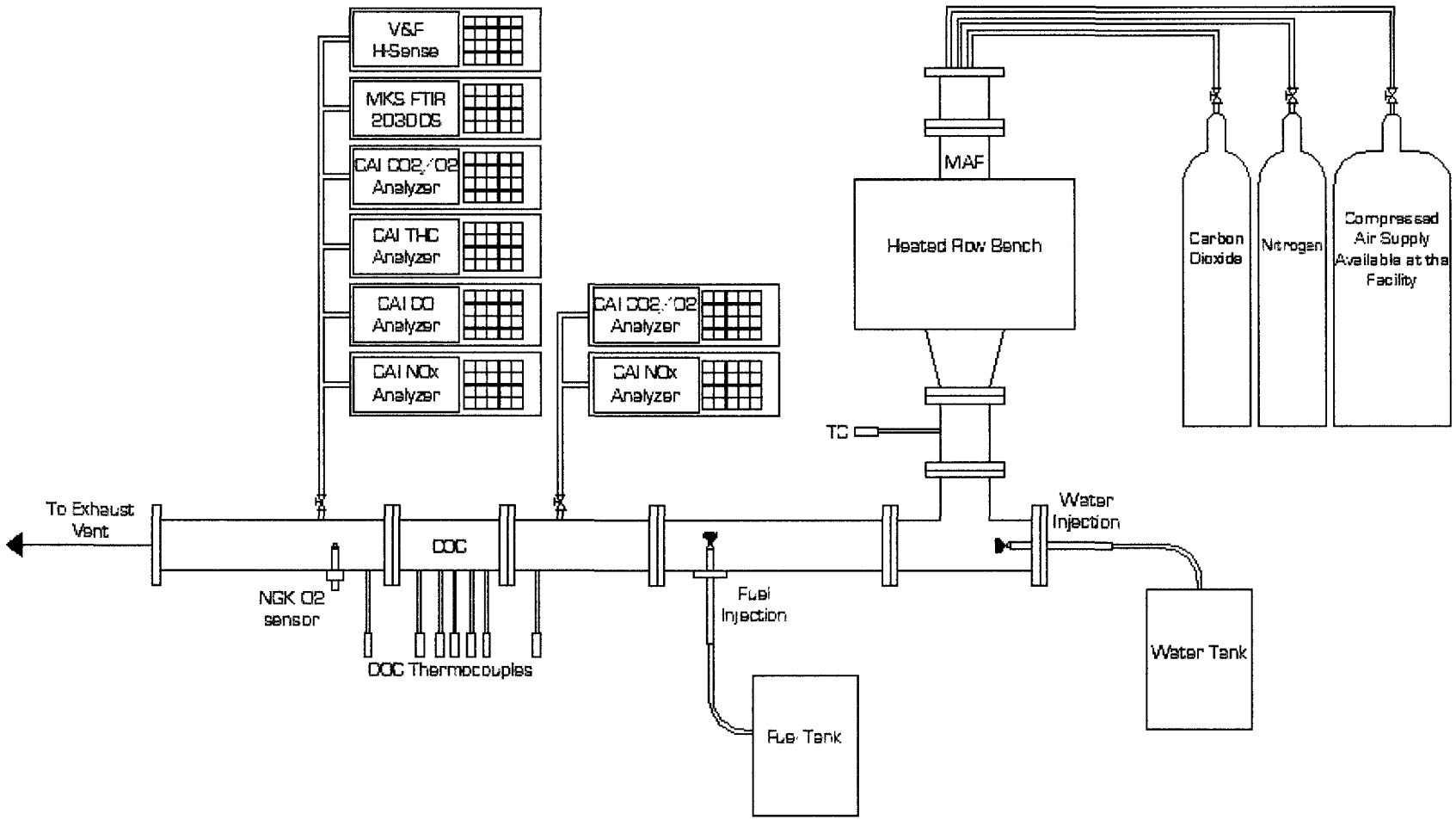

Figure 3.4: Schematic Diagram of the Experimental Set-up for Tests 8-11

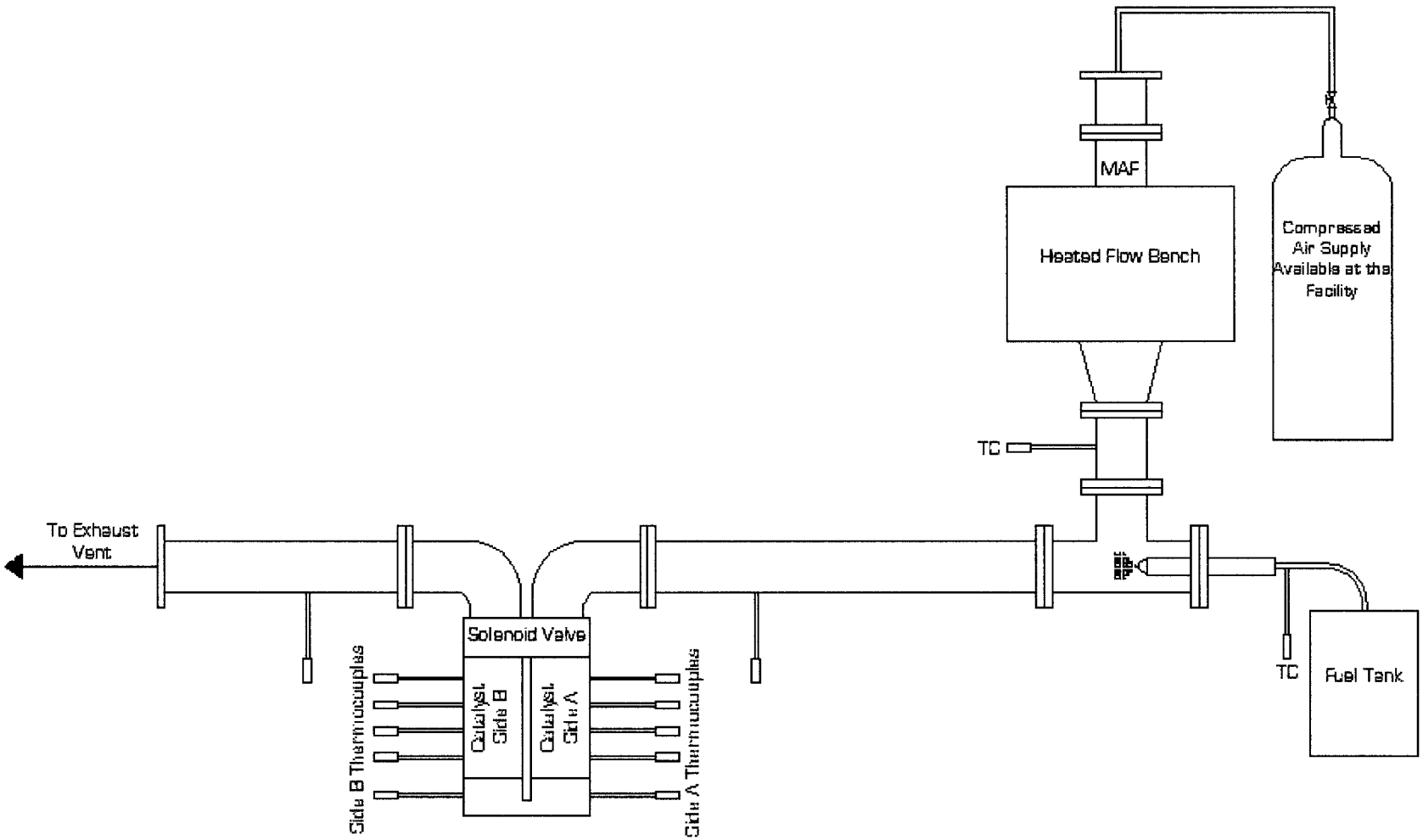

Figure 3.5: Schematic Diagram of the Experimental Set-up for Test 12

3.2 Data Acquisition and Fuel Injection

Test monitoring, data acquisition, and data recording were done through National Instruments (NI) hardware and LabVIEW software. A National Instruments SCXI-1303 terminal block and an SCXI-1102 thermocouple module were used for acquiring the thermocouple voltage signals and converting them to a temperature output. The module had a 32 channel capacity with each channel capable of managing one thermocouple. An SCXI-1302 module was used for collecting the voltage signals from the MAF and the oxygen sensors. Calibration tables, provided from the manufacturer, were then used to convert the MAF voltage to a flow rate. The SCXI-1302 module was connected to a SCXI-1349 adapter. The SCXI-1302, SCXI-1303, and SCXI-1349 were all installed in a SCXI-1000 chassis which was connected by a PCI-6220 card to a Windows XP system. A photo of the National Instruments SCXI-1000 chassis with three SCXI-1303 and SCXI-1102 modules and one SCXI-1302 module is shown in Figure 3.6.

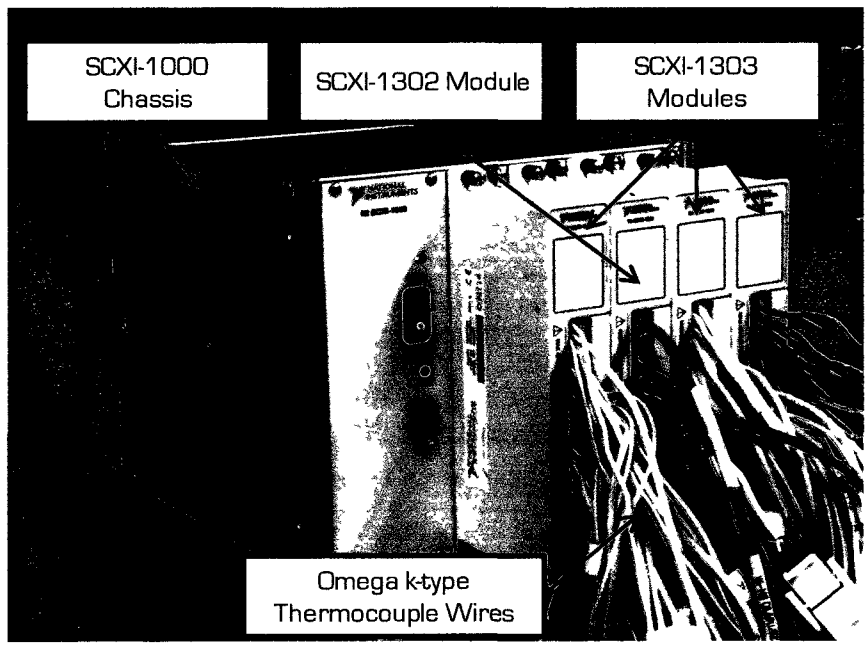

Figure 3.6: National Instruments SCXI-1000 Chassis with Modules

In Windows, a program was developed in LabVIEW 7.1, a visual programming language, for collecting and recording the data acquired by the aforementioned National Instruments modules. The data collected by the program included the thermocouple, the MAF, and the oxygen sensor signals as well as the gas sampling data from the numerous gas analyzers used during the testing. Screenshots of the front panel and the LabVIEW code written by the author are shown in Figure 3.7 and in Figure 3.8 respectively.

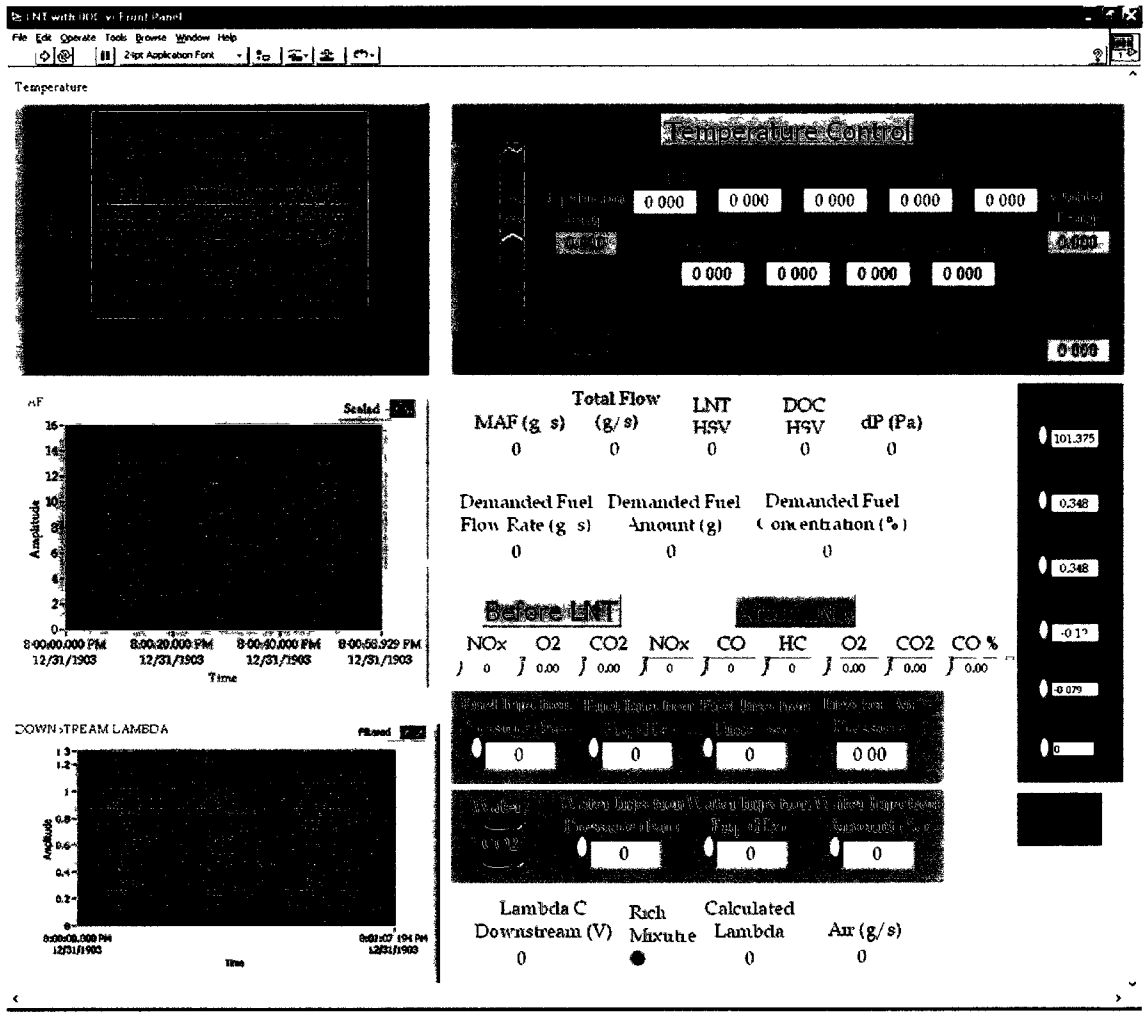

Figure 3.7: LabVIEW Front Panel for Monitoring and Storing the Acquired Data

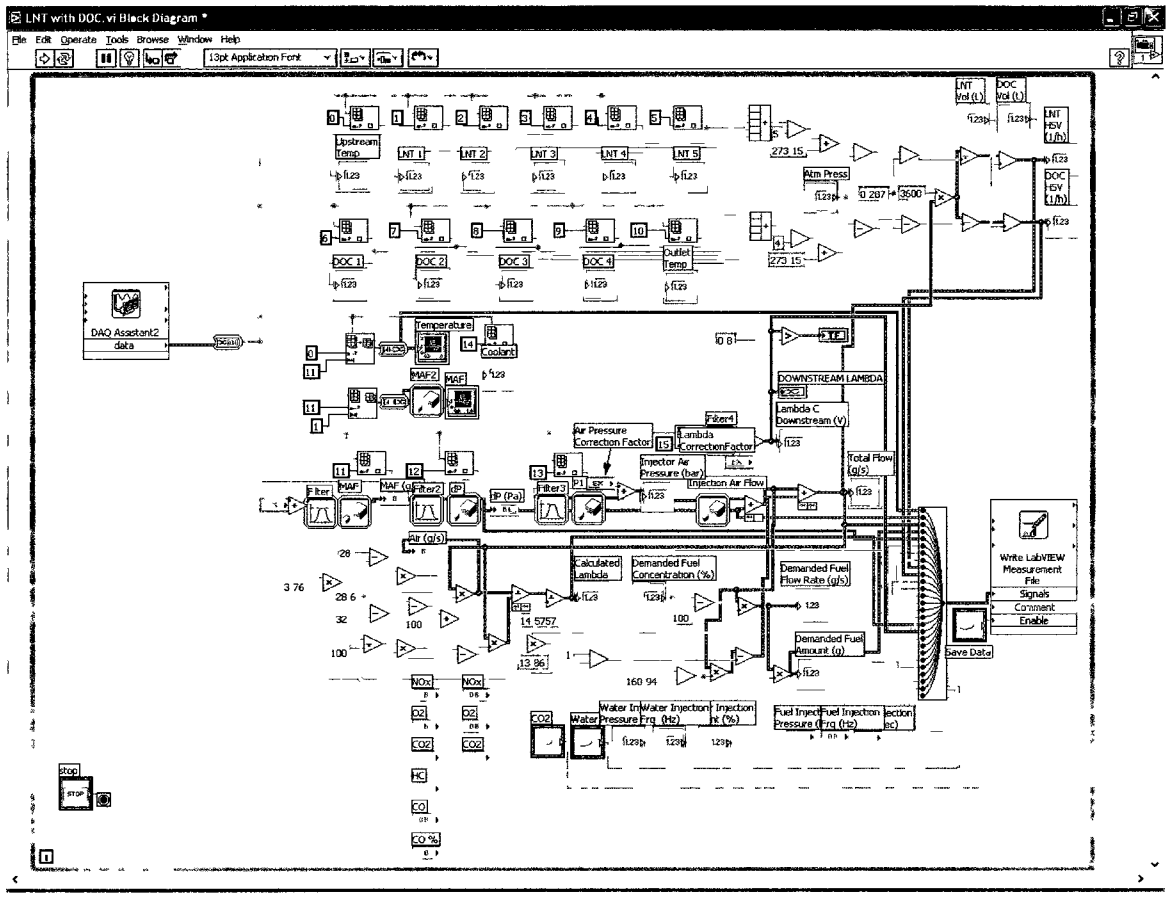

Figure 3.8: LabVIEW Code for Monitoring and Storing the Acquired Data

A separate LabVIEW program was developed by Dr. Shui Yu of the Clean Diesel Engine Laboratory for controlling the fuel and water injectors. The front panel of this program is shown in Figure 3.9. An ethernet cable was used for communication between the LabVIEW program, a National Instruments cRIO-9002 real-time controller, and a cRIO-9474 digital output module which was used to provide the command signals for the injectors. A photo of the cRIO-9002 and the cRIO-9474 modules is shown in Figure 3.10. In all of the tests, a 4 bar injection pressure was used for both the water and the fuel injectors. Deionized water was used for the water injection and an ultra low

sulphur diesel (ULSD) fuel with a fuel density of approximately 0.8465 kg/L and a cetane number of approximately 44.95 was used for the fuel injection.

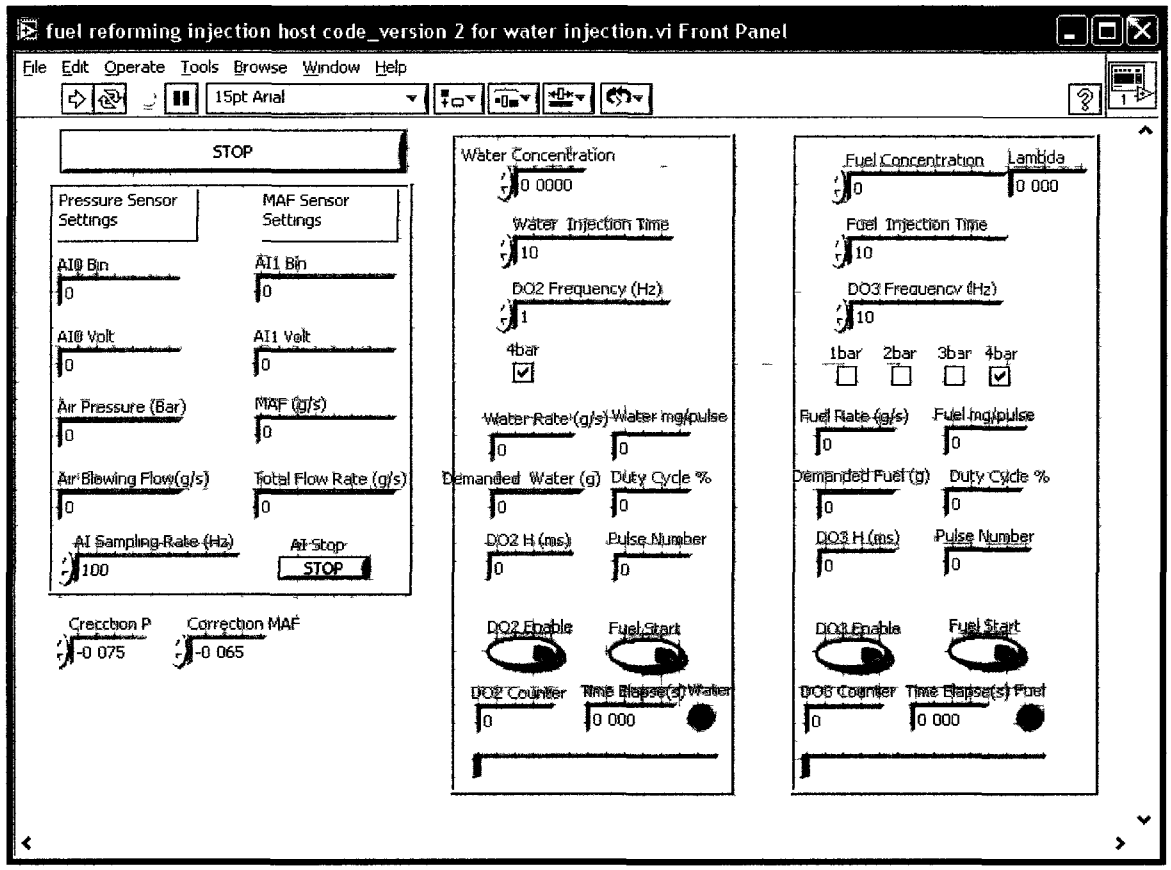

Figure 3.9: LabVIEW Front Panel for Fuel and Water Injection Control

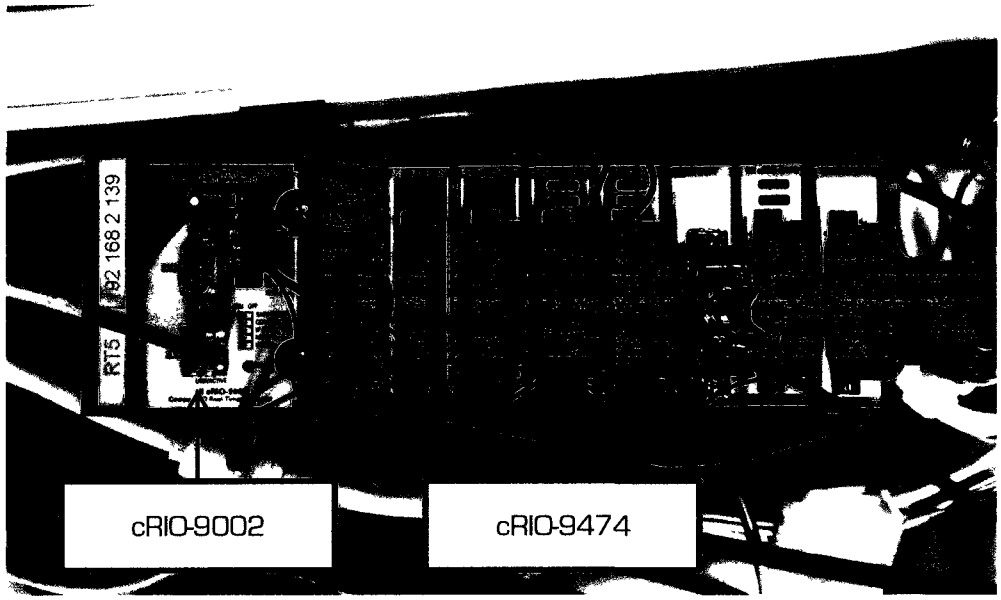

Figure 3.10: National Instruments cRIO-9002 and cRIO-9474

3.3 Lean NOx Trap and Flow Reversal

For the LNT tests, a modified Umicore NGK honeycomb substrate was used. The original monolith had a 144 mm diameter and a 152 mm length (Figure 3.11). The monolith was then modified by reducing its size so that the total volume of the modified LNT was suitable for the flow rate range of the flow bench system. The length of the monolith was kept the same while the diameter was reduced to 54 mm by cutting the monolith brick into a smaller portion as shown in Figure 3.12. A similar procedure was followed for the DOC monolith so that the final dimensions of the DOC and the LNT were the same. The main LNT monolith properties are given in Table 3.1. It should be mentioned that this LNT catalyst was intended for use in a conventional LNT and was not optimized for use in a long breathing LNT.

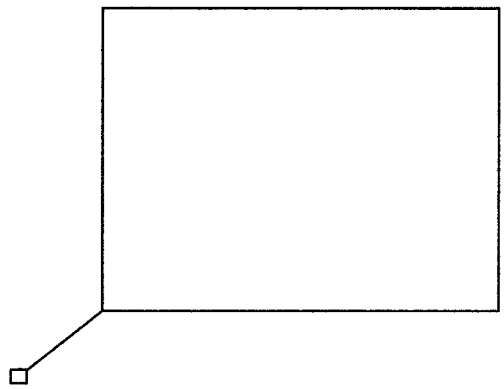

Figure 3.11: Umicore Lean NOx Trap Monolith

Table 3.1: Lean NOx Trap Properties

LNT	
Monolith Type	Umicore NGK Substrate
Length	152 mm
Diameter	54 mm
Volume	0.348 L
Cells per Square Inch	400
Catalyst Loading	110 g/ft^3 of Pt/Rh

Figure 3.12: Cutting of the Lean NOx Trap

For the flow reversal tests, two DOC monoliths, labelled as catalyst side A and catalyst side B in Figure 3.13, were fitted inside a flow reversing canister. The canister was divided in two halves by a wall and an air gap. The flow direction was controlled through a solenoid valve as shown in Figure 3.13. The solenoid valve was controlled through National Instruments hardware and LabVIEW software. Two heating elements were installed inside the canister at thermocouple locations C1 and C2 as shown in Figure 3.13. The heating elements were located in the air gap between the two DOC monoliths so that only one monolith was heated at a time; catalyst side B was heated with forward flow while catalyst side A was heated with reverse flow. The design of the flow reversal canister, the implementation of the solenoid valve mechanism, the installation of the heating elements, and the development of the LabVIEW program were the work of Dr. Usman Asad and Mr. Xiaoye Han.

Further work was done by the author to instrument the flow reversal canister with thermocouples and to develop a LabVIEW program for monitoring and recording the temperature and the flow data. Each thermocouple was labelled according to its position inside the canister. Thermocouples labelled with the letter A corresponded to those installed along DOC catalyst A, thermocouples labelled with the letter B corresponded to those installed along DOC catalyst B, and thermocouples labelled with the letter C corresponded to those installed along the air gap by the heating elements. A photo of the flow reversal canister installed on the flow bench system is shown in Figure 3.14.

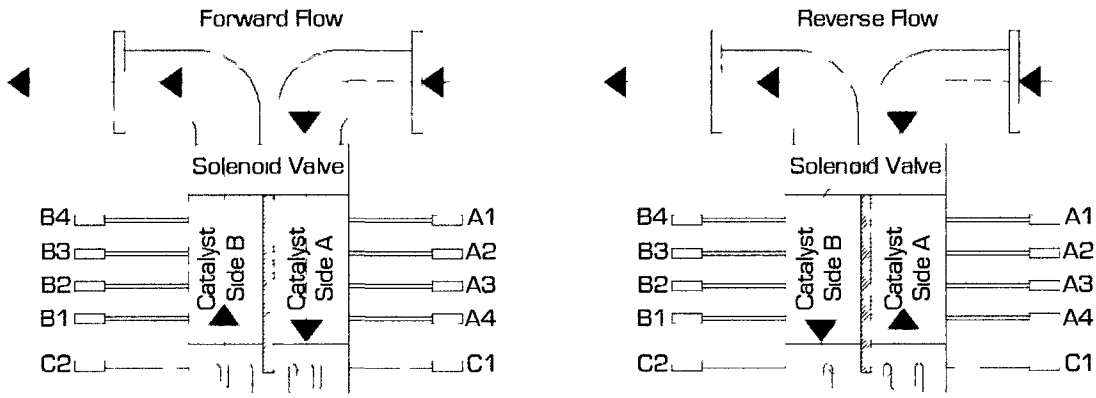

Figure 3.13: Schematic Diagram of the Flow Reversal Reactor Set-up

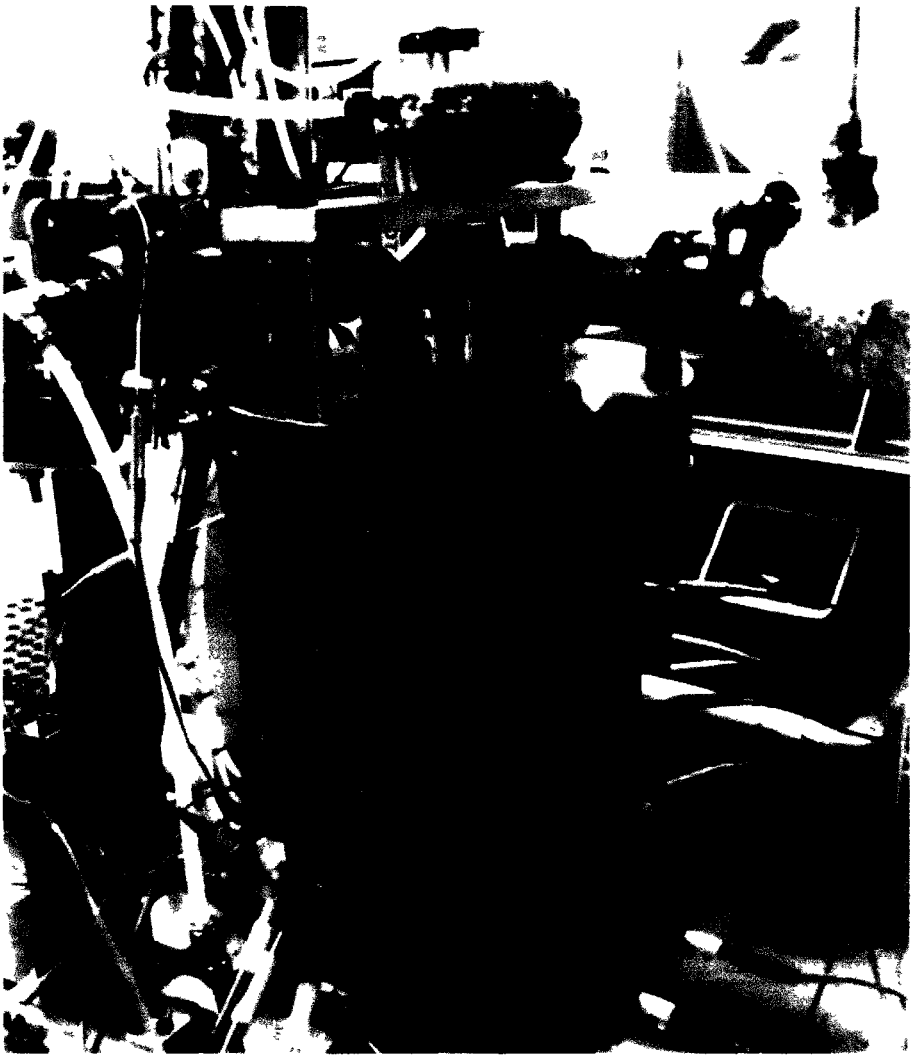

Figure 3.14: Flow Reversal Canister Installed on the Flow Bench System

3.4 Gas Analyzers

For Tests 1 through 11, gas sampling upstream and downstream of the LNT and the DOC monoliths was done as indicated in Figure 3.1 through Figure 3.4. The gas was drawn from the flow bench system by a KNF Neuberger pump. The gas sampling was done with a cold sampling train. Analysis of the sampled gas was done by a California Analytical Instruments (CAI) sampling bench, an MKS 2030-DS Fourier Transform

Infrared Spectroscopy (FT-IR) analyzer, and a V&F H-Sense analyzer. A photo of the CAI sampling bench is shown in Figure 3.15.

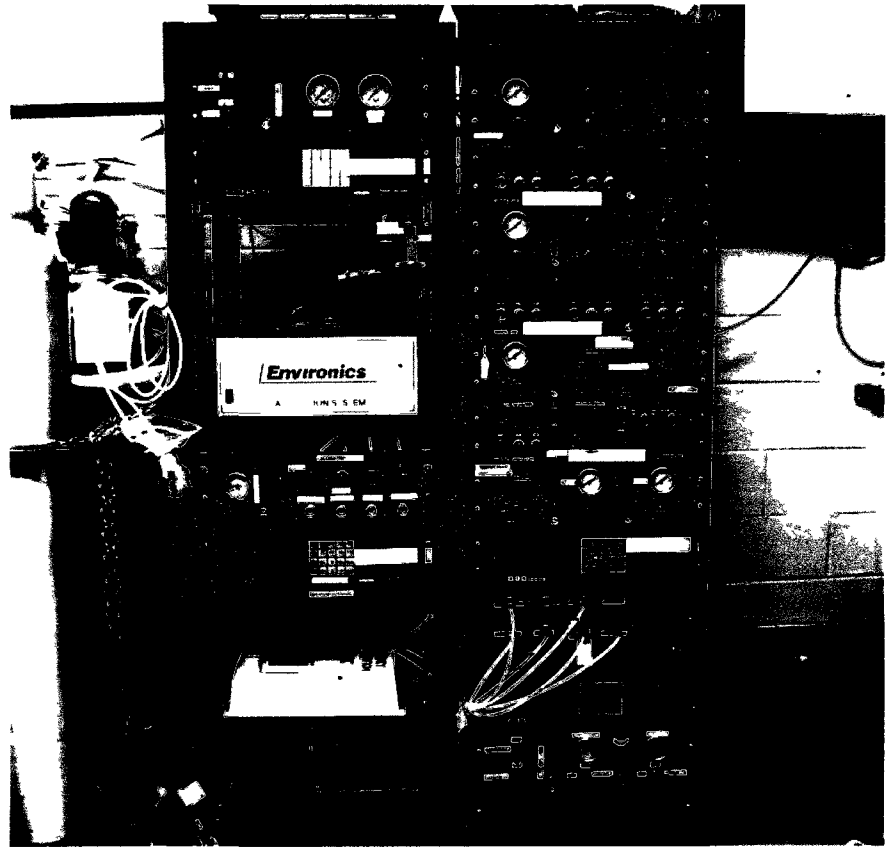

Figure 3.15: California Analytical Instruments Gas Analyzer Bench

The sampling bench consisted of two heated chemiluminescence detectors (CLD), three non-dispersive infrared detectors (NDIR), and one heated flame ionization detector (FID). The heated chemiluminescence detector was utilized for measuring the nitrogen oxide (NOx) content of the sampling gas. The CLD had a 0.01 ppm resolution and an analysis range of 0 to 3000 ppm NOx. One CLD was used for measuring the NOx before the LNT and the other was used for measuring the NOx after the LNT. The three NDIRs were used for measuring the carbon monoxide, the carbon dioxide, and the oxygen concentrations. Oxygen and carbon dioxide were measured both before and after the

LNT/DOC while the carbon monoxide was only measured downstream of the monoliths. The NDIRs were capable of measuring oxygen concentration in the range of 0-25%, carbon monoxide in the range of 0-5000 ppm, and carbon dioxide in the range of 0-40%. The FID measured the hydrocarbon concentration downstream of the LNT/DOC. It had an analysis range of 0-3000 ppm.

One of the purposes of the FT-IR was to confirm the calibration of the water injector by measuring the water concentration of the feed gas. To measure the water concentration, a temporary heated sampling train was used. The FT-IR was also used to measure the downstream concentrations of NOx, carbon dioxide, carbon monoxide, ammonia, and hydrocarbon species. A photo of the FT-IR analyzer is shown in Figure 3.16. A V&F H-Sense analyzer was used for measuring the hydrogen concentration of the sampling gas downstream of the DOC. The H-Sense analyzer was capable of measuring hydrogen concentrations from 0-100%. A photo of the analyzer is shown in Figure 3.17.

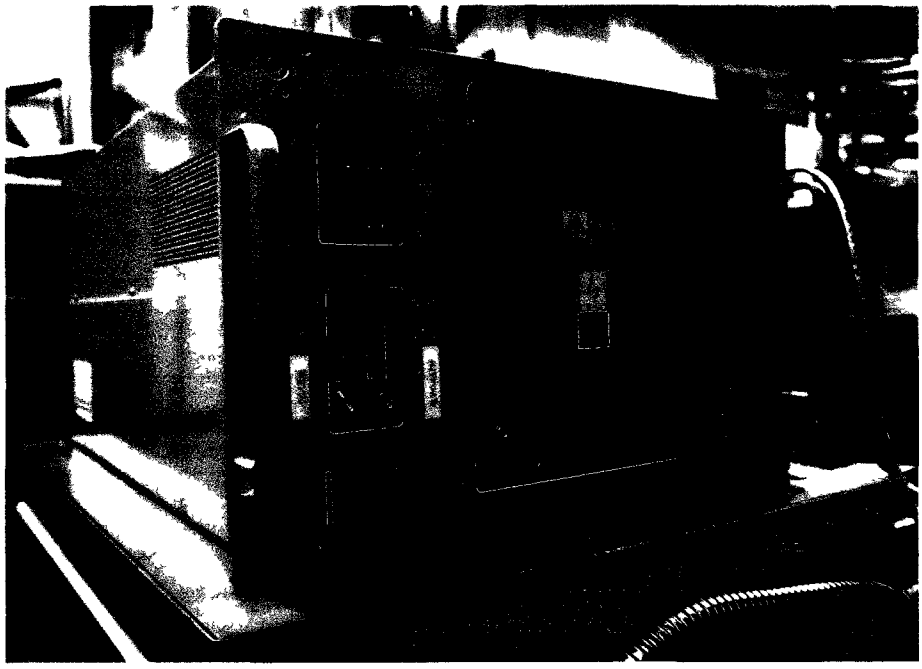

Figure 3.16: MKS 2030-DS Fourier Transform Infrared Spectroscopy Analyzer

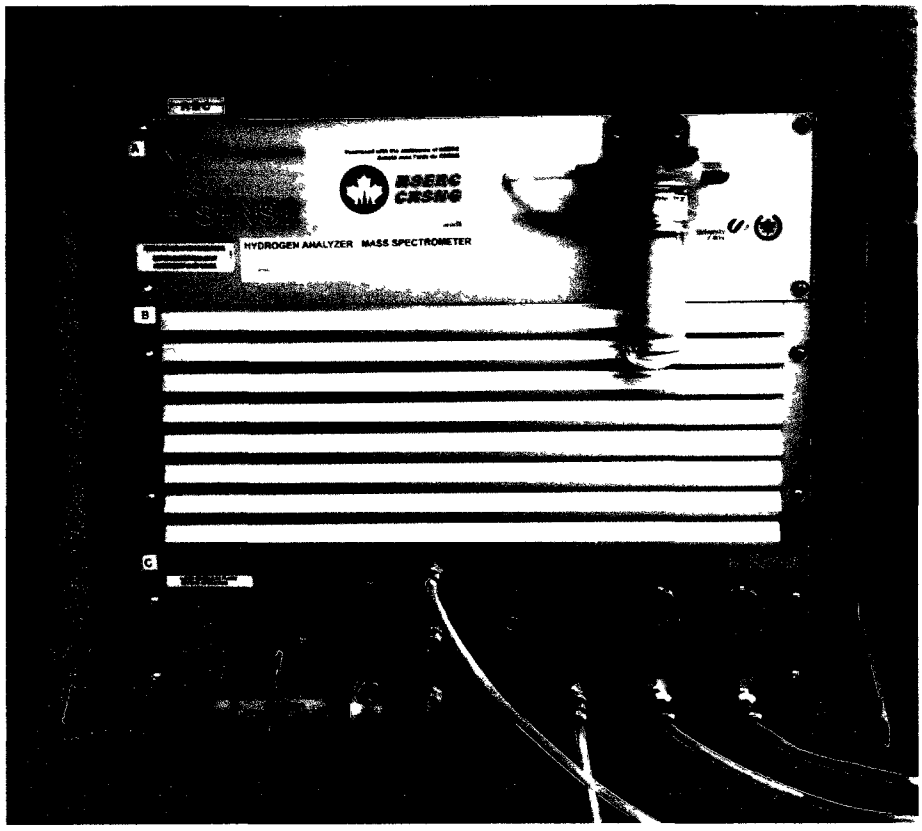

Figure 3.17: V&F H-Sense Hydrogen Analyzer

CHAPTER 4: LONG BREATHING LEAN NOX TRAP TESTS

4.1 Investigation of the Long Breathing LNT Concept

The first set of tests focused on validating the long breathing Lean NOx Trap concept. The LNT was installed on the flow bench system and supplied with a heated feed gas consisting of air mixed with NOx as shown in Figure 3.1. Three different feed gas NOx levels were utilized: 110 ppm, 70 ppm, and 50 ppm. The adsorption time of the LNT was measured for each NOx level and it was proposed that longer LNT adsorption times would be achieved with lower feed gas NOx levels. The adsorption time was defined as the time it took a freshly regenerated LNT to reach a NOx slip value of 20 ppm. The reason 20 ppm NOx slip was chosen as the target cut-off for the LNT adsorption derived from correlated diesel engine tests (Figure 4.1) with test engine specifications as shown in Table 4.1.

Table 4.1: Correlated Test Engine Specifications

Engine Specifications	
Engine Type	4 Cylinder Ford DuraTorq "Puma"
Injection System	Diesel Common-Rail Direct Injection
Maximum Injection Pressure	160 MPa
Compression Ration	18.2:1
Bore	86 mm
Stroke	86 mm

Figure 4.1 shows the proposed long breathing zone in relation to the modified cut-off line for the 2010 EPA's heavy-duty emission NOx standard. The 2010 EPA heavy duty emission standard for NOx is 0.2 g/bhp·hr (~0.27g/kW·hr) but a voluntary cut-off value of 0.15 g/kW·hr was chosen. The reason for this was because the EPA standards are expressed in terms of brake power while the data obtained from the engine (and plotted in Figure 4.1) was in terms of indicated power. Thus, a more rigorous NOx standard of 0.15 g/kW·hr, in terms of indicated power, was utilized instead of the EPA standard defined in terms of brake power.

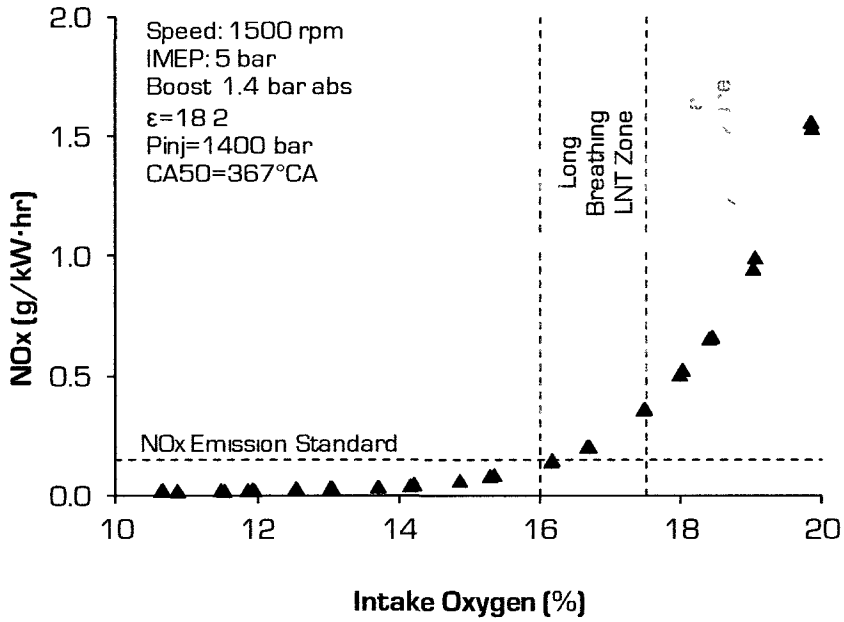

Figure 4.1: Example of a Suitable Long Breathing LNT Zone

The results in Figure 4.1 indicated that at the lower limit of the long breathing zone, at 16.0% intake oxygen, the engine-out NOx emissions were close to meeting the NOx emission standard. However, at the upper limit of the long breathing zone, at 17.5% intake oxygen, it was observed that the engine-out NOx emissions moderately exceeded the NOx emission standard. For the engine test results and conditions shown in Figure

4.1, calculations suggested that an LNT with a minimum NOx conversion efficiency of 45% would be required to meet the EPA's heavy duty NOx emission standard throughout the entire long breathing zone. At a 50 ppm feed gas NOx level, a 45% NOx conversion efficiency corresponded to a NOx slip value of 27.5 ppm but a more conservative value of 20 ppm was chosen to account for inefficient and unoptimized LNT regeneration. For this reason, the LNT adsorption cycle was measured as the time for a NOx slip of 20 ppm to be reached.

The adsorption took place at steady state conditions, an LNT temperature of 300°C and an hourly space velocity of 90,000. This temperature and HSV were chosen based on typical diesel exhaust condition. Typical diesel exhaust temperatures are in the range of 200°C to 600°C and typical HSVs are in the range of 15,000 to 150,000. Mid-range values were selected while considering the capabilities of the flow bench system. Once the cut-off NOx slip level was reached, the LNT was regenerated through diesel fuel injection. The regeneration consisted of a ten second fuel injection event at an excess air ratio (λ) of 0.7. The test conditions were summarized in Table 2.1.

Figure 4.2 shows the adsorption response of the LNT to 110 ppm of NOx in the feed gas. From this figure, it was observed that the initial NOx slip was very low, in the range of 1 to 2 ppm of NOx. This indicated that there was initially a high NOx storage efficiency. As the LNT continued to be supplied with 110 ppm of NOx, the saturation of barium sites was approached and the NOx storage efficiency declined. This was confirmed by the increase in NOx slip with time as shown in Figure 4.2. The NOx slip continued to increase until the cut-off value of 20 ppm was reached after approximately 12.5 minutes of adsorption.

Once 20 ppm NOx slip was reached, the LNT was regenerated. To reduce the fuelling and to ensure fuel-rich regeneration, nitrogen gas was added to the feed gas to reduce the air concentration. Due to unoptimized regeneration, a significant increase in NOx slip was observed, up to 1600 ppm of NOx, indicating a low NOx regeneration efficiency. It was determined from calculations that the NOx regeneration efficiency was on the order of 10%. This was far below the NOx conversion levels of 75% or more as commonly found in literature [1,13]; however, the focus of these tests was on the adsorption period of the LNT and not on the regeneration. Thus, a primitive regeneration strategy with low NOx regeneration efficiency was tolerable for these tests. After the regeneration was completed, the NOx slip reverted back to 1 to 2 ppm.

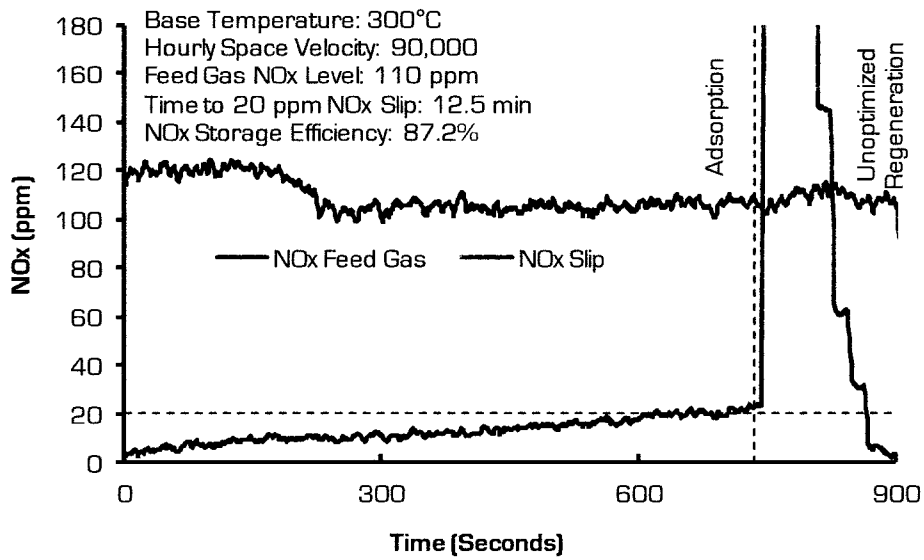

Figure 4.2: Adsorption Time for 110 ppm of NOx with Balance Air

The test was repeated for a feed gas composition of 70 ppm of NOx with balance air. This NOx level corresponded to the far right region of the long breathing LNT zone as shown in Figure 4.1. The adsorption response of the LNT is shown in Figure 4.3.

With 70 ppm of NOx, the initial NOx slip was 1 to 2 ppm, as was the case with 110 ppm of NOx. However, with 70 ppm of NOx, barium saturation was much slower, indicated by a less rapid increase in the NOx slip level. With 70 ppm of NOx, the cut-off slip level of 20 ppm was reached after approximately 17.5 minutes.

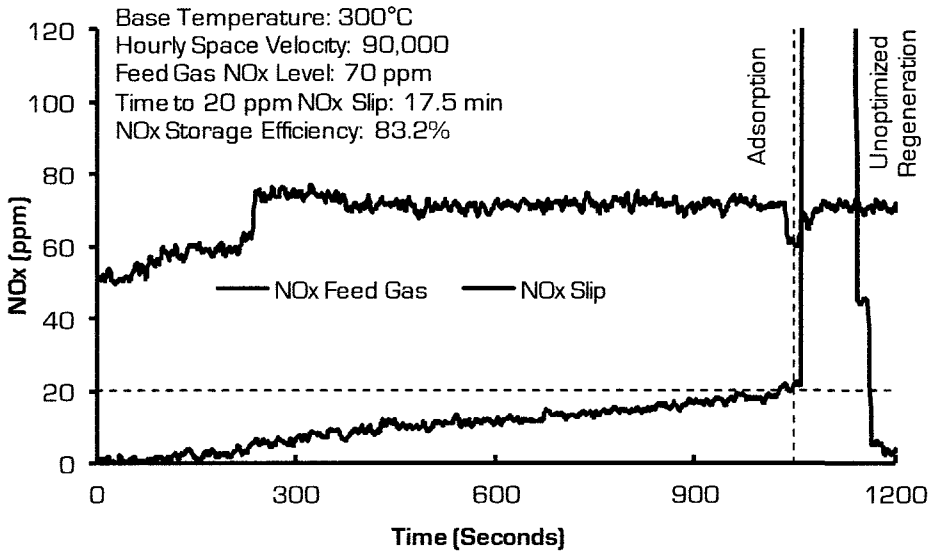

Figure 4.3: Adsorption Time for 70 ppm of NOx with Balance Air

A similar trend was observed when the LNT was exposed to 50 ppm of NOx (Figure 4.4). Again, there was an initial NOx slip of 1 ppm but the rate of increase of NOx slip was much slower than with the previous two tests. This time, the cut-off of 20 ppm was reached after 48 minutes of adsorption. Also, just as with the previous two tests, the NOx regeneration efficiency was low as indicated by a rapid NOx slip increase during regeneration.

A summary of the experimental test results is shown in Figure 4.5. In this figure, the feed gas NOx level was plotted against the corresponding adsorption time. It was observed that the relationship of the feed gas NOx level to the adsorption time was not

linear. It appeared to be closer to an exponential relationship with the adsorption time increasing exponentially as the feed gas NOx level was reduced. The exponential increase in adsorption time was attributed to an improved NOx storage efficiency of the long breathing LNT. The conventional LNT exposed to 110 ppm of NOx had a NOx storage efficiency of 87.2% during the adsorption cycle (Figure 4.2) while the long breathing LNT exposed to 50 ppm of NOx had a NOx storage efficiency of 80.0% during the adsorption cycle (Figure 4.4). From these values it would appear that the conventional LNT had a better NOx storage efficiency. However, this was the result of defining the adsorption cycle in terms of a constant NOx slip cut-off value of 20 ppm.

For a fair comparison, the NOx storage efficiency should be compared over a constant time period. For the conventional LNT exposed to 110 ppm of NOx, the NOx storage efficiency was 87.2% for a 12.5 minute adsorption cycle and for the long breathing LNT exposed to 50 ppm NOx, the NOx storage efficiency was 94.0% for the first 12.5 minutes of adsorption. Thus, the long breathing LNT had a better storage efficiency for the first 12.5 minutes of adsorption.

Further testing (Test 2) was done to confirm the exponential relationship between the adsorption time and the feed gas NOx level; the results are shown in Figure 4.6. Comparing Figure 4.5 and Figure 4.6, it was observed that even though the absolute values for the adsorption time were different at a given NOx level, there was an exponential relationship between NOx level and adsorption time in both sets of tests.

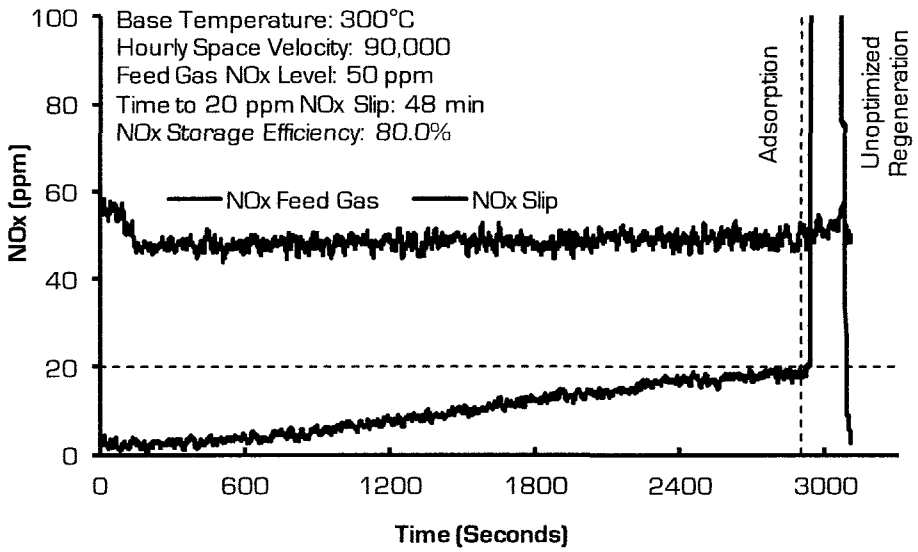

Figure 4.4: Adsorption Time for 50 ppm of NOx with Balance Air

The discrepancy in the adsorption times between Test 1 and Test 2 at a given NOx level was attributed to sulphur poisoning of the catalyst and/or thermal aging of the LNT since it was observed, shortly after the start of Test 3, that the LNT was no longer effectively storing NOx; the NOx slip was 100% even with a freshly regenerated LNT. For subsequent tests, a fresh LNT monolith with the same geometric and catalyst properties (Table 3.1) was used.

The supplemental energy savings of the long-breathing LNT are shown in Figure 4.7. In this figure, the energy consumption was normalized with respect to the amount of injected supplemental fuel. Thus, the figure shows the energy consumption of the LNT per gram of consumed supplemental fuel. This normalization was done to account for different regeneration fuelling strategies.

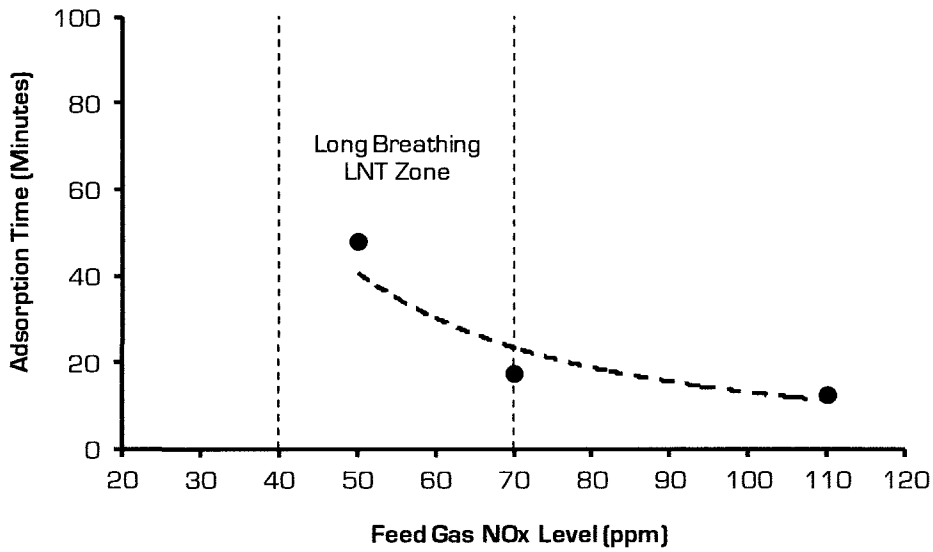

Figure 4.5: Summary of Test Results for Test 1

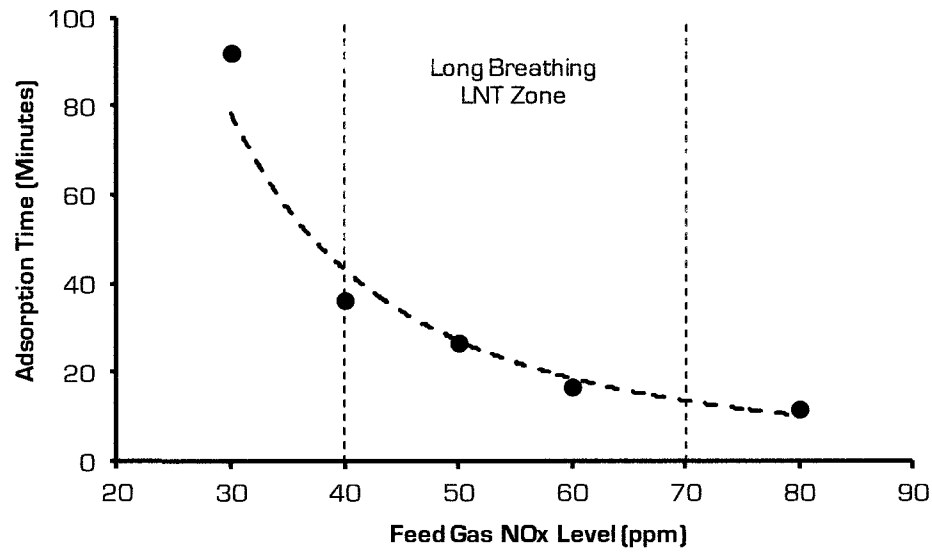

Figure 4.6: Results of the Confirmation Tests

From Figure 4.7 it was observed that the energy consumption of the LNT was greatly reduced as the NOx level was reduced. With 110 ppm of NOx, the energy consumption of the LNT was 57 J/s per gram of injected fuel while at a level of 50 ppm

NOx, the energy consumption of the LNT was 15 J/s per gram of injected fuel. By reducing the NOx level from 110 ppm to 50 ppm of NOx, supplemental energy savings of 73% were achieved. Thus, the initial experimental investigation validated the long breathing LNT concept by demonstrating the energy saving potential of a long breathing LNT.

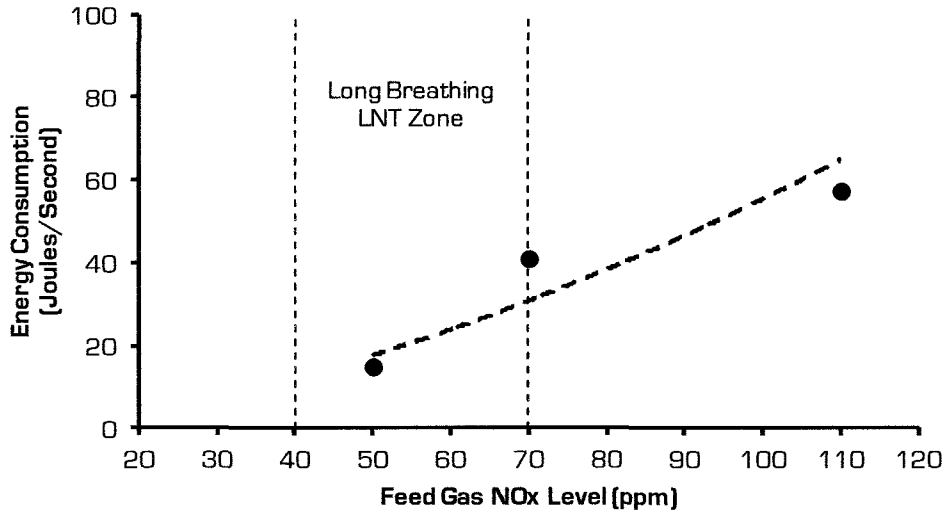

Figure 4.7: Supplemental Energy Consumption of the LNT

4.2 Further Investigations with Simulated Exhaust Gas

The first two sets of tests established that the long breathing LNT concept was valid. However, these tests were done with a feed gas consisting of NOx mixed with air. Further testing was done with a feed gas which more closely approximated real diesel exhaust by adding carbon dioxide from a cylinder source and by injecting liquid water as shown in the experimental set-up in Figure 3.2. For these test, the feed gas consisted of 50/70/110 ppm of NOx, 6% water, 8.5% carbon dioxide, and balance air. During regeneration, nitrogen was also added. The test conditions for Test 3 were shown in

Table 2.1. The LNT temperature was 300°C while the hourly space velocity was 75,000. For these tests, a hot sampling train was temporarily used to confirm the calibration of the water injector with the FT-IR spectroscopy measurements.

Figure 4.8 shows the adsorption time of the LNT for a level of 110 ppm of NOx. A similar trend was observed compared to Figure 4.2; the initial NOx slip was very low, on the order of 1 to 2 ppm followed by a steady increase until the cut-off value of 20 ppm was reached. However, compared to Test 1, the adsorption time for 110 ppm of NOx was significantly shorter with the simulated feed gas. Previously the adsorption time was 12.5 minutes but with the simulated feed gas the adsorption time was 2.8 minutes. The shorter adsorption time was mainly attributed to sulphur poisoning, as previously discussed, but also partly to the feed gas composition. With the addition of water and carbon dioxide, the oxygen concentration in the feed gas was reduced from 21% to 17%. Effective NOx storage during the adsorption period requires excess oxygen to oxidize nitric oxide (NO) to nitrogen dioxide (NO_2) as shown in Figure 1.2. Thus, with reduced oxygen concentration, the NOx storage efficiency of the LNT was reduced.

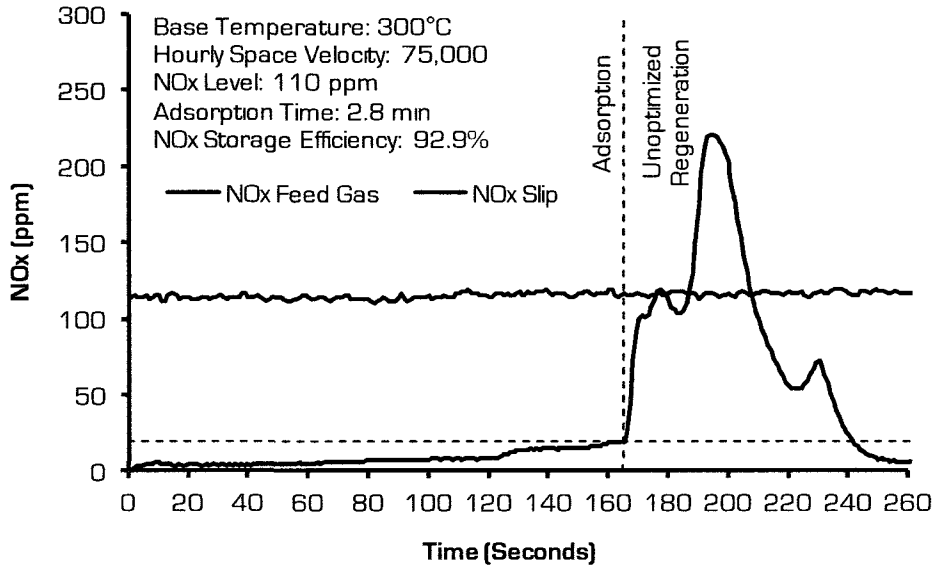

Figure 4.8: Adsorption Time for 110 ppm of NOx with Simulated Feed Gas

The results for 70 ppm of NOx are shown in Figure 4.9 and for 50 ppm of NOx in Figure 4.10. In both figures, a similar pattern was observed which contrasted with the observations made in Test 1. Similar to Test 1, the initial NOx slip was very low, 1 to 2 ppm, but instead of a steady and gradual increase as was observed in the Test 1 results, the NOx slip remained below 3 ppm for an extended period of time and then rose rapidly until the cut-off value was reached. Nevertheless, similar adsorption times were observed compared to Test 1; 22.5 minutes for 70 ppm of NOx and 47.6 minutes for 50 ppm of NOx. During regeneration, there was a considerable increase in the NOx slip. The NOx regeneration efficiency was 47.9% for the 70 ppm NOx test and 61.7% for the 50 ppm NOx test.

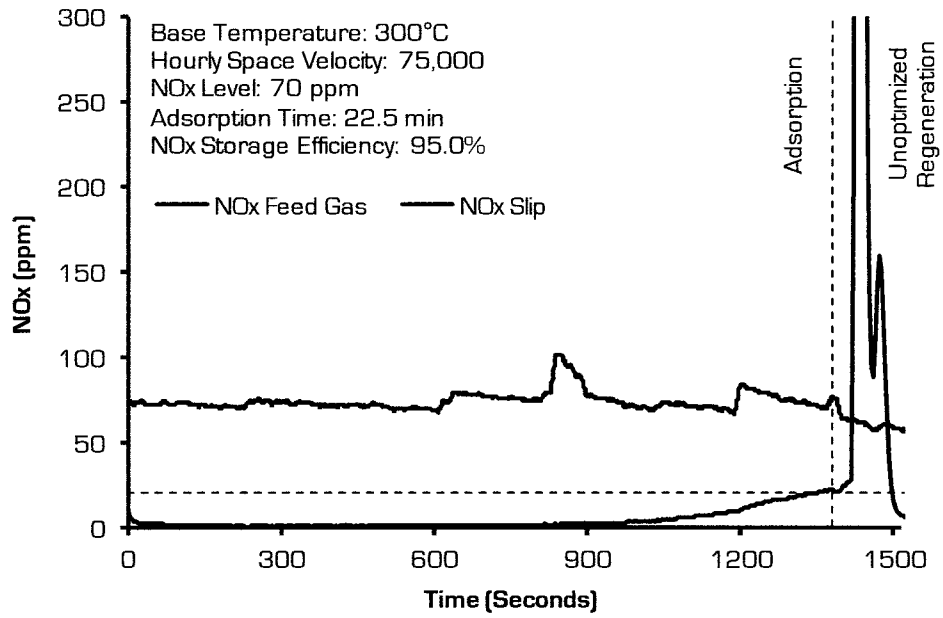

Figure 4.9: Adsorption Time for 70 ppm of NOx with Simulated Feed Gas

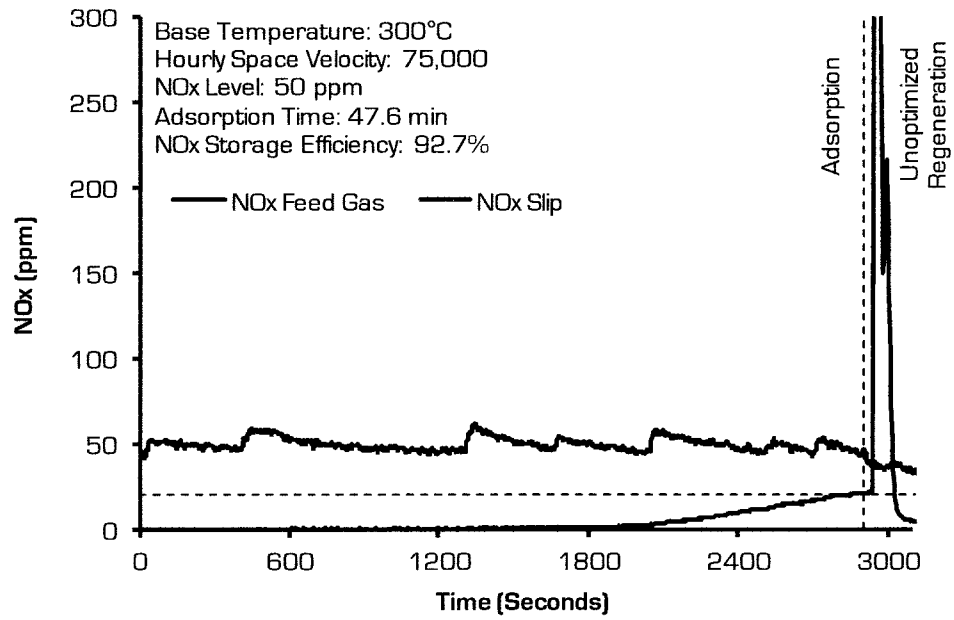

Figure 4.10: Adsorption Time for 50 ppm of NOx with Simulated Feed Gas

The test results are summarized in Figure 4.11 where a similar pattern was noticed compared to Test 1; the adsorption time appeared to increase exponentially as the

NOx level was reduced. Thus, even though there was a difference in the adsorption time at a given NOx level between Test 1 and Test 3, the overall pattern appeared to be the same. Looking at the resulting supplemental energy consumption of the LNT (Figure 4.12), a similar pattern was observed compared to Test 1; by reducing the NOx level from 110 ppm to 50 ppm, a significant reduction in the supplemental energy consumption was achieved.

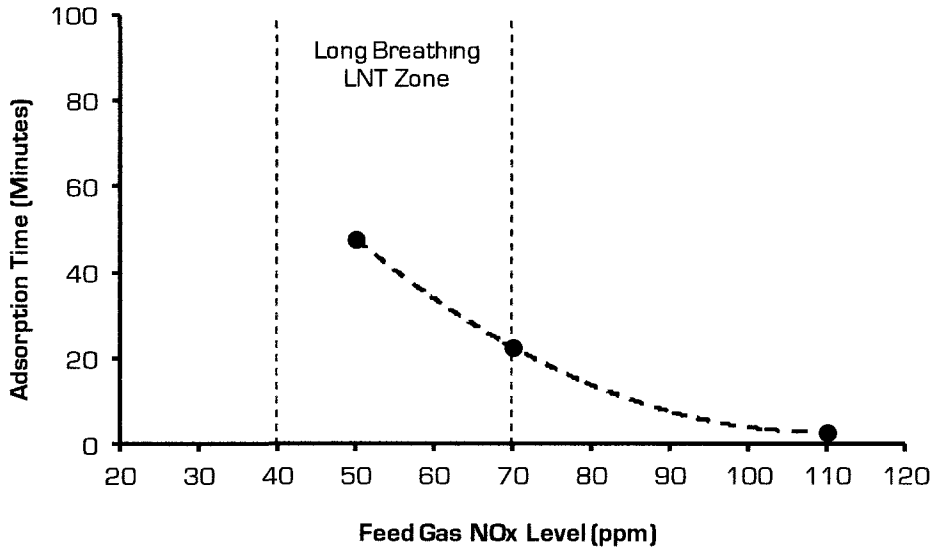

Figure 4.11: Summary of Test Results for Test 3

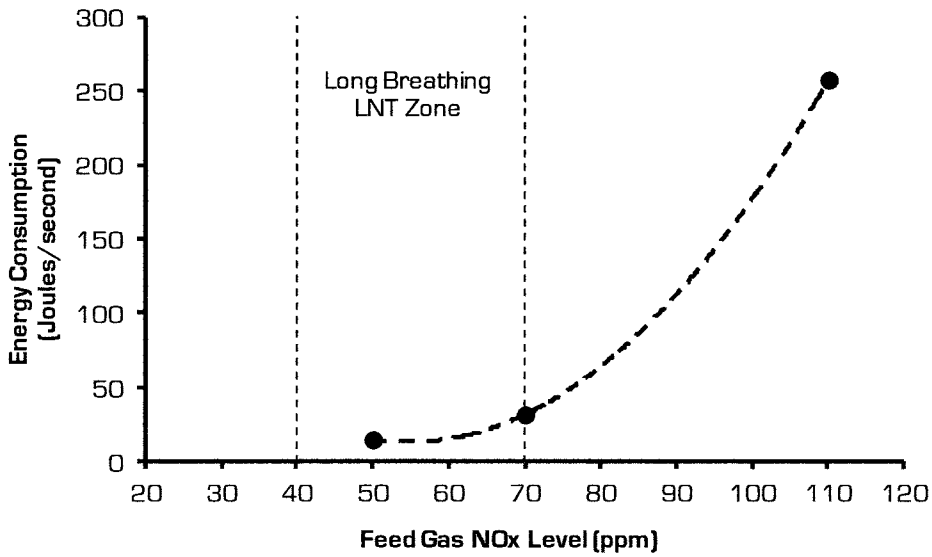

Figure 4.12: Supplemental Energy Consumption of the LNT with Simulated Gas

Additional tests were run under the same test conditions as Test 3 to confirm the trends observed with simulated exhaust gas. A summary of the results is shown in Figure 4.13. The same trend was observed as in the previous tests; the LNT adsorption time increased exponentially as the LNT feed gas level was reduced. In addition, the adsorption times were similar in Test 3 and Test 4 at 50 ppm and 70 ppm NOx. At 110 ppm NOx, the adsorption time in Test 4 was considerably longer, 11.3 minutes compared to 2.8 minutes. The adsorption time for 110 ppm NOx in Test 4 was taken as a truer representative value because in Test 3 the 110 ppm test was done with a sulphur poisoned catalyst. When the results were plotted in terms of the LNT supplemental energy consumption (Figure 4.14), a 78% reduction in the energy consumption with 50 ppm NOx compared to 110 ppm NOx was observed. In general, the trends and values were similar to those in previous tests. Thus, the long breathing LNT concept was validated for the simulated exhaust gas conditions.

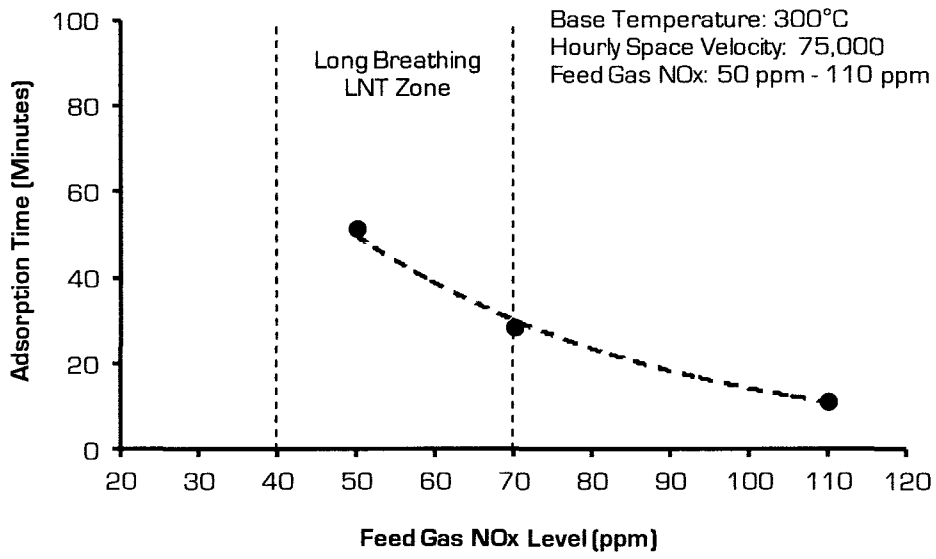

Figure 4.13: Summary of the Adsorption Times in the Repeatability Tests

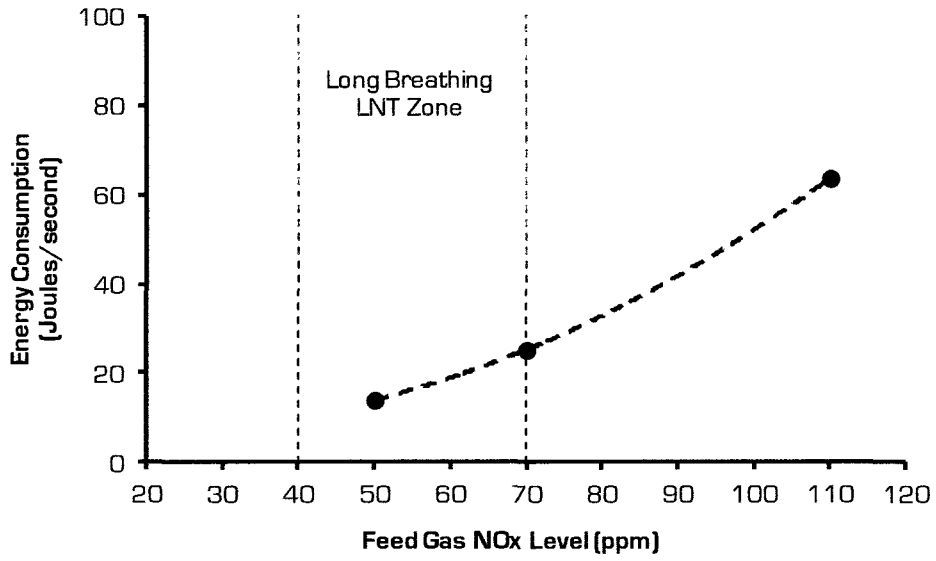

Figure 4.14: LNT Energy Consumption in the Repeatability Tests

4.3 Effects of Hourly Space Velocity and LNT Temperature

Tests 1 to 4 investigated the effects of the feed gas NOx level on the adsorption time of the LNT while the LNT temperature and the hourly space velocity were kept constant. Additional tests were done to investigate the effects of the hourly space velocity and the LNT temperature at a constant feed gas NOx level. For these tests, the LNT was installed on a flow bench set-up with an upstream DOC as shown in Figure 3.3. Test 6 explored the effect of the hourly space velocity on the LNT adsorption time at a constant LNT temperature of 300°C and at a constant feed gas NOx level of 50 ppm. The hourly space velocity was varied from 75,000 to 120,000 by adjusting the flow rate of the feed gas. Further test details were given in Table 2.1.

A representative adsorption cycle is shown in Figure 4.15. A similar trend was observed as in the previous tests. The NOx slip was initially low, 0 to 1 ppm, and then increased steadily to 20 ppm. The adsorption time was 33.8 minutes at an HSV of 90,000. As in previous tests, a considerable increase in NOx was observed during regeneration. The same pattern was observed at all the other space velocities.

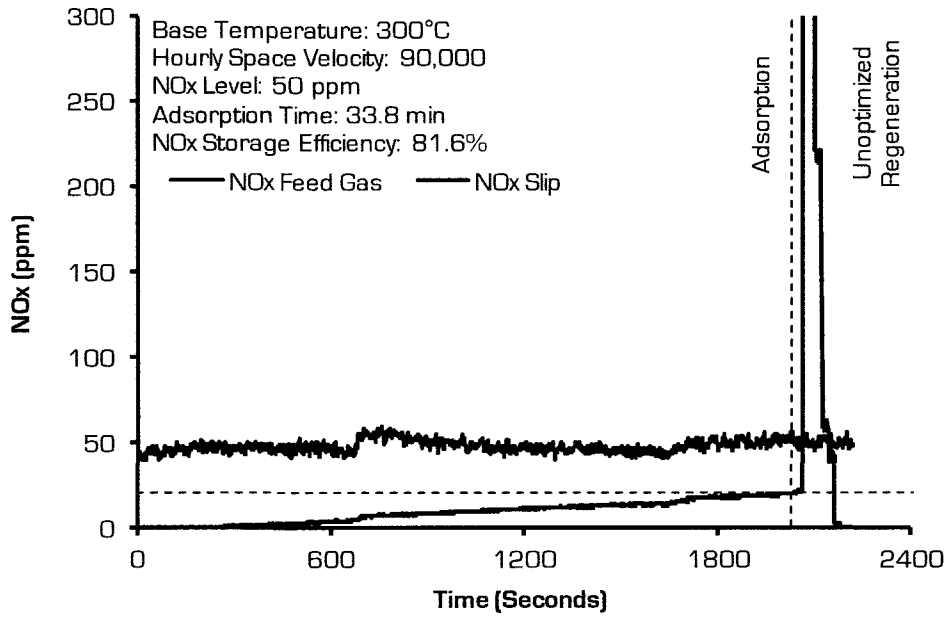

Figure 4.15: LNT Adsorption Response at a 90,000 Hourly Space Velocity

A summary of the adsorption times at different hourly space velocities is shown in Figure 4.16. It was observed that with a lower HSV the LNT adsorption time moderately increased. At an HSV of 75,000, the adsorption time was 55 minutes while at 120,000 it was 22 minutes. At higher space velocities, the feed gas mass flow rate was higher. Therefore, even though the NOx ppm level was constant for all space velocities, the LNT was exposed to a higher mass of NOx per unit of time at higher hourly space velocities; at an HSV of 75,000 the LNT was exposed to 0.36 mg/s of NOx while at 120,000 the LNT was exposed to 0.54 mg/s of NOx. This was a reason shorter adsorption times were observed at higher hourly space velocities. In addition, it was hypothesized that the adsorption time was shorter at higher space velocities due to shorter contact times between the feed gas and the catalyst which could decrease the NOx storage efficiency during adsorption. However, the results in Figure 4.17 suggested that

this was not the case; the NOx storage efficiency was about 80% across the tested HSV range.

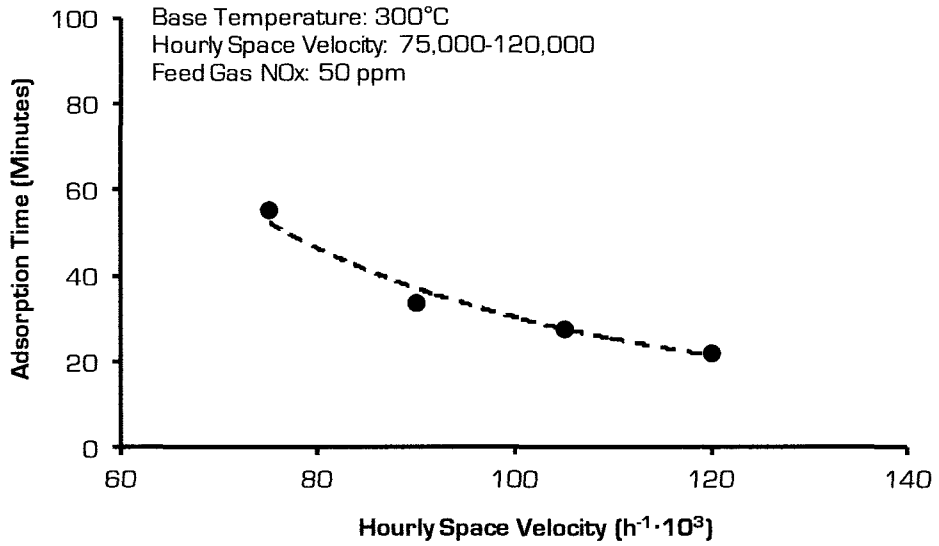

Figure 4.16: Effect of HSV on LNT Adsorption Time

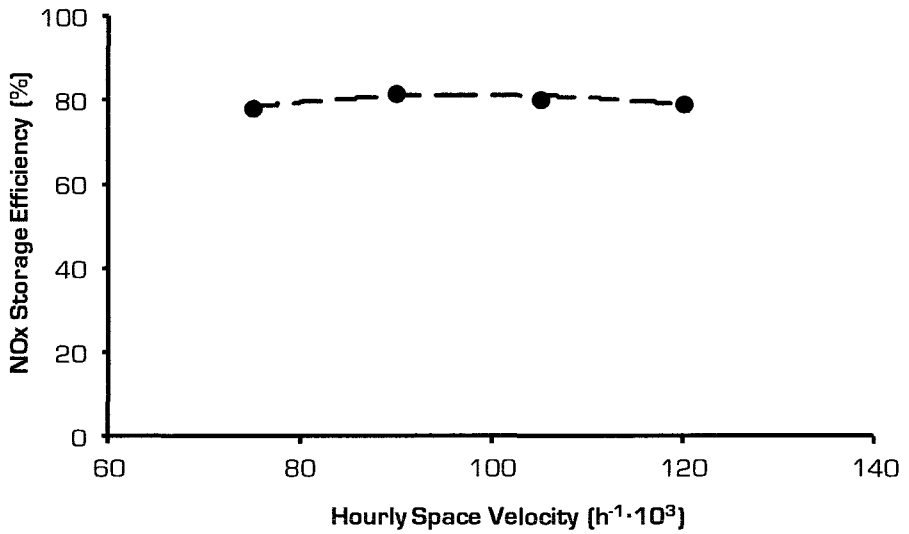

Figure 4.17: Impact of Hourly Space Velocity on NOx Storage Efficiency

Subsequent tests explored the effect of the LNT temperature on the LNT adsorption time at a constant hourly space velocity and at a constant feed gas NOx level. The LNT temperature was varied from 190°C to 310°C by adjusting the flow bench heater settings. The upper temperature limit was restricted by the flow bench system. Simulated diesel exhaust gas with 50 ppm NOx was used as the feed gas. More detailed test conditions were given in Table 2.1.

A similar pattern was noticed as in the previous tests with an initially low NOx slip followed by a steady increase. However, it was observed that at 300°C (Figure 4.18) the LNT adsorption time was considerably shorter than in previous tests with similar LNT temperature and feed gas NOx level (Figure 4.10). The difference was mainly attributed to the higher hourly space velocity. In the previous test (Figure 4.10), the HSV was 75,000 but for this test the hourly space velocity was 105,000. The effect of hourly space velocity was previously shown in Figure 4.16.

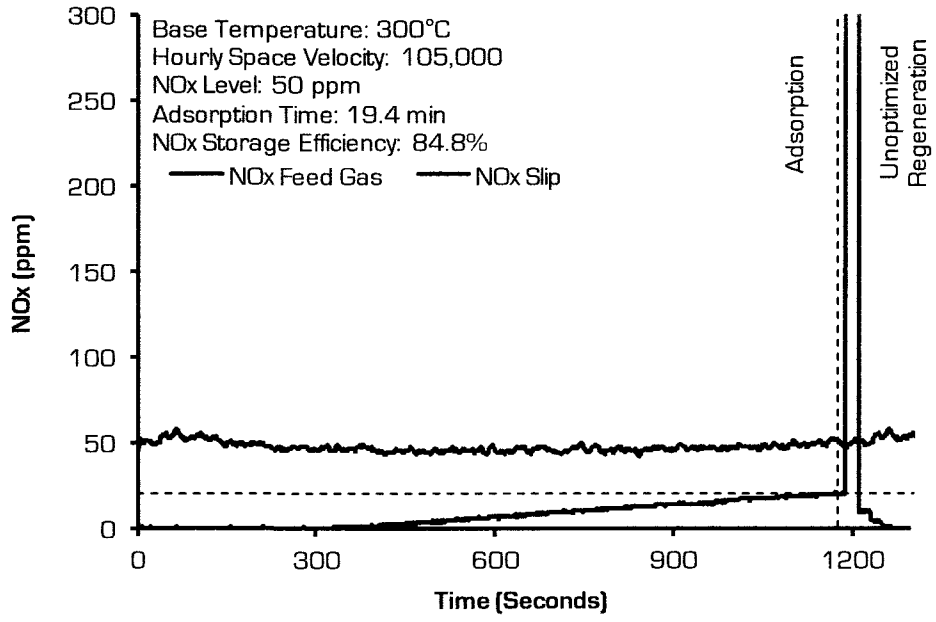

Figure 4.18: LNT Adsorption Response at an LNT Temperature of 300°C

At 190°C (Figure 4.19), the LNT adsorption time was only two minutes; this was a significant reduction compared to the adsorption time at 300°C. The relationship between temperature and adsorption time was not linear. The results were summarized in Figure 4.20 and it was observed that the LNT had similar adsorption times, about 20 minutes, in the temperature range between 290°C and 310°C. When the LNT temperature was decreased to 265°C, a slight decrease in the adsorption time occurred, it was 17.5 minutes. A further reduction in the LNT temperature to 235°C resulted in a moderate drop in the adsorption time to 11.8 minutes while a further reduction to 190°C resulted in a 2 minute adsorption time.

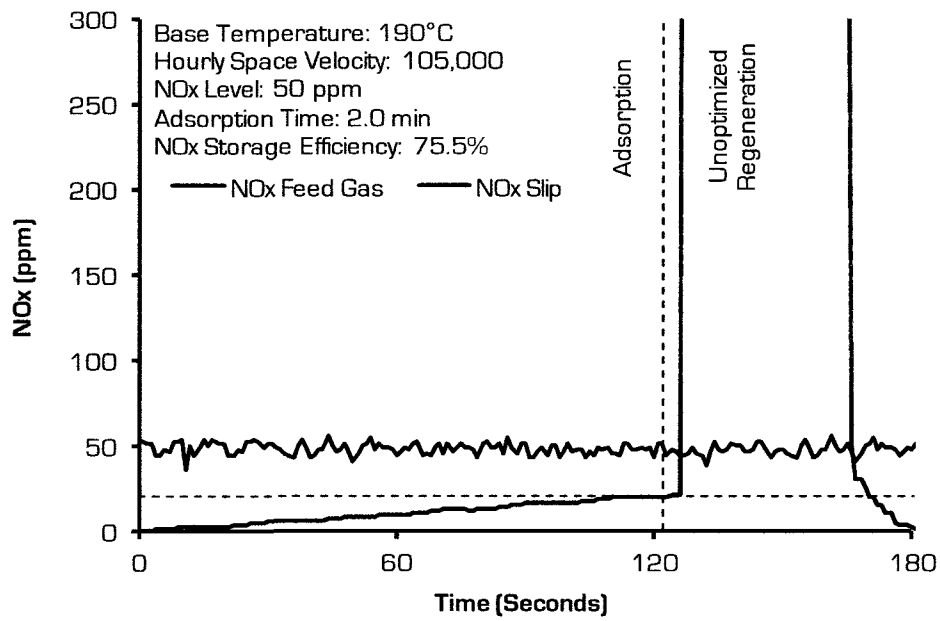

Figure 4.19: LNT Adsorption Response at an LNT Temperature of 190°C

The effect of temperature on the adsorption time was abrupt and dramatic. At higher temperatures, from 265°C to 310°C, the effect of temperature on the adsorption time was almost negligible. However, below temperatures of 265°C, there was a sharp drop in the adsorption time. These results seemed to be consistent with literature [29-30].

The authors in [29] and [30] suggested that below a temperature of 250°C there was a significant drop in the NOx storage ability of the LNT due to a lowering of the platinum catalyst oxidation activity which led to reduced oxidation of NO to NO_2; a critical step in the NOx storage process. The same conclusion could be applied for a long breathing LNT exposed to low temperatures as indicated by the results shown in Figure 4.20.

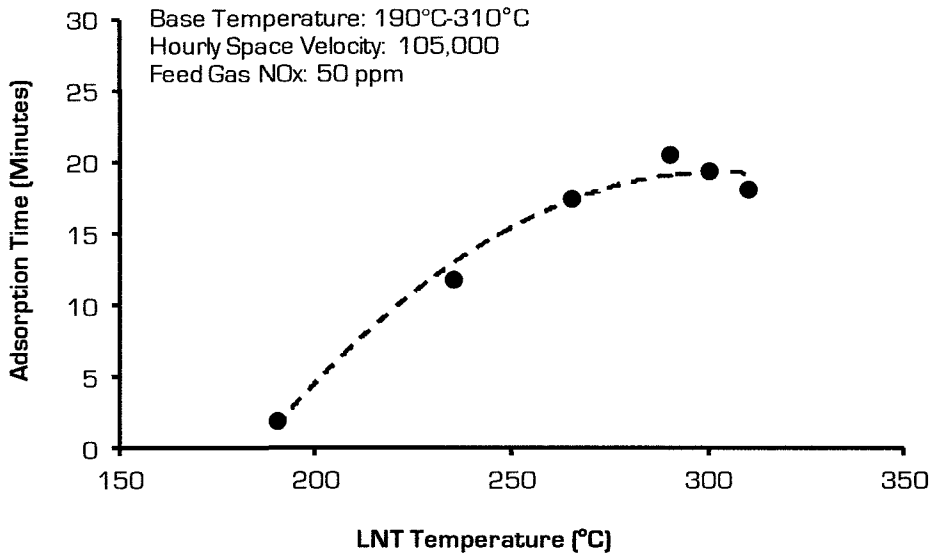

Figure 4.20: Effect of Temperature on LNT Adsorption Time

4.4 Long Breathing LNT Performance

The preceding tests focused on validating the long breathing LNT concept. Having accomplished this task, it was desired to investigate the NOx storage and NOx regeneration efficiencies of the long breathing LNT. The equations used for calculating the NOx storage and the NOx regeneration efficiencies are shown below.

$$NOx\ Storage\ Efficiency\ (\%) = \frac{m_{ads\_in} - m_{ads\_slip}}{m_{ads\_in}} \times 100 \qquad (4.1)$$

$$NOx\ Regeneration\ Efficiency\ (\%) = \frac{m_{total\_in} - m_{total\_slip}}{m_{total\_in} - m_{ads\_slip}} \times 100 \quad (4.2)$$

$$m_{total\_in} = m_{ads\_in} + m_{regen\_in} \quad (4.3)$$

$$m_{total\_slip} = m_{ads\_slip} - m_{regen\_slip} \quad (4.4)$$

Figure 4.21 and Figure 4.22 show representative NOx storage and regeneration efficiencies for 70 ppm and 50 ppm of NOx respectively. Both figures show that the NOx storage efficiency of the long breathing LNT was quite high, over 90% in both instances. The NOx regeneration efficiency during regeneration was 48% for the 70 ppm test and 62% for the 50 ppm test. Combining these results and the data from the engine test results shown in Figure 4.1 resulted in values of 0.14 g/kW·hr of tailpipe NOx for the 70 ppm test and 0.06 g/kW·hr of tailpipe NOx for the 50 ppm test. Therefore, the NOx emission target of 0.15g/kW·hr was satisfied in both instances.

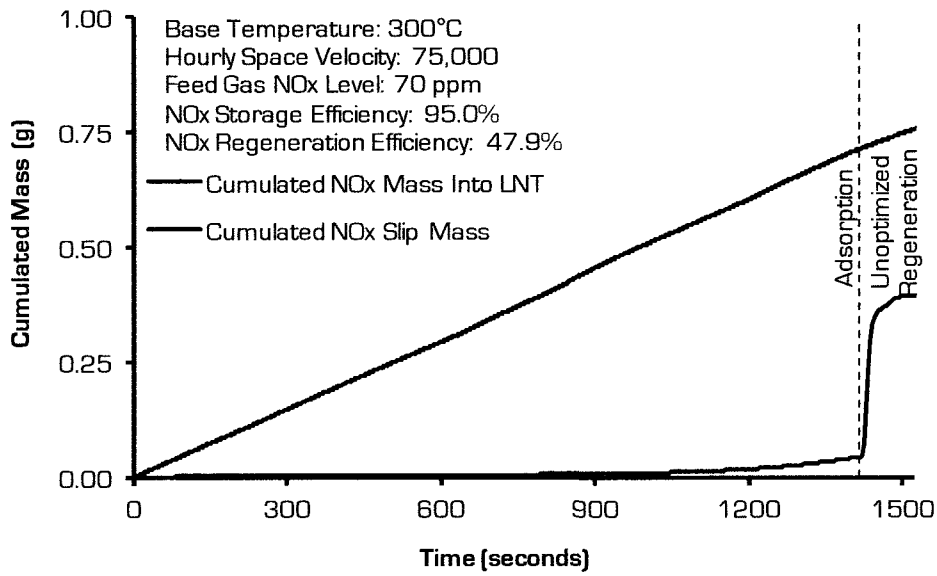

Figure 4.21: NOx Storage and Regeneration Efficiency at 70 ppm of NOx (Test 3)

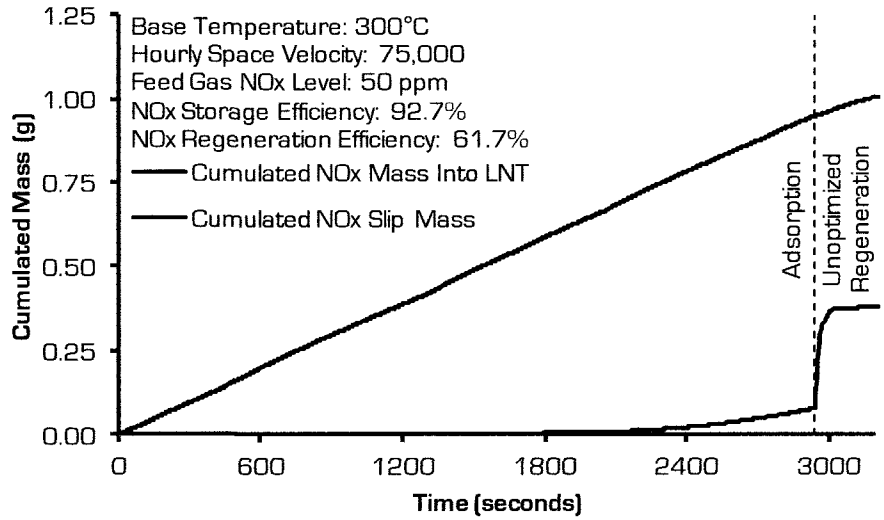

Figure 4.22: NOx Storage and Regeneration Efficiency at 50 ppm of NOx (Test 3)

Further analysis was done to compare the overall fuel consumption, in terms of g/hr, of the various NOx reducing strategies. The strategies which were compared were: no/low EGR with a traditional LNT; medium EGR with a long breathing LNT; and high EGR without deNOx after-treatment. Representative test results from Test 3, Test 4, and Test 5 and the engine test results from Figure 4.1 were used to evaluate the strategies. The LNT fuel consumption from the flow bench tests was added to the fuel consumption from the engine tests at the corresponding NOx range.

The results (Table 4.2) suggested that the long breathing strategy consumed the least amount of fuel for these engine test conditions. The long breathing LNT strategy and the low temperature combustion (high EGR) strategy showed similar total fuel consumption, 372.6 g/hr and 374.5 g/hr respectively. However, the long breathing LNT strategy had slightly lower total fuel consumption while having a slightly higher IMEP. The total fuel consumption of the high EGR (LTC) strategy probably would have been slightly higher if the IMEP was the same as for the medium EGR test. Conversely, the

total fuel consumption of the low EGR strategy was moderately higher due to the high fuel consumption of the traditional LNT which would require much more frequent LNT regenerations than the long breathing LNT. It should be noted that it was assumed that 7.1 grams of fuel were consumed per LNT regeneration because that was the fuel amount used during the LNT tests. However, it was calculated that if less than 4.7 grams of fuel could be used to regenerate the LNT, the low EGR with a traditional LNT strategy would consume less fuel than the LTC and the long breathing LNT strategies at these engine conditions. Further testing would be required to determine if fuel consumption savings could be obtained with the long breathing LNT with different engine test conditions and with different LNT fuelling strategies.

Table 4.2: Comparison of Different NOx Reduction Strategies

				Fuel Consumption		
EGR Range	After-treatment Type	NOx Range ppm	IMEP bar	Engine Test g/hr	LNT g/hr	Total g/hr
No/Low	Traditional LNT	300	5.16	281.2	133.1	414.3
Medium	Long Breathing LNT	50	5.27	364.3	8.3	372.6
High	No After-treatment	20	5.09	374.5	0.0	374.5

CHAPTER 5: HYDROGEN GENERATION TESTS

5.1 Motivation for On-board Hydrogen Generation

Utilizing hydrogen as a reductant can provide multiple benefits to an LNT such as improved regeneration and desulfation efficiencies. For this reason, on-board hydrogen generation was investigated with a DOC monolith on a flow bench set-up as shown in Figure 3.4 to determine if hydrogen can be generated on-board a diesel vehicle with typical diesel exhaust gas conditions and a typical diesel fuel. The purpose of these tests (Tests 8-11) was to determine the effects of various exhaust gas parameters, such as the temperature and the hourly space velocity, on the hydrogen production of the DOC. If the results show that on-board hydrogen generation is possible, for future work it is suggested to implement on-board hydrogen generation upstream of a long breathing LNT.

5.2 Air-to-Fuel Ratio Effects

The conditions for the hydrogen generation tests were shown in Table 2.1 (Tests 8-11) and the set-up was shown in Figure 3.4. The first test (Test 8) investigated the effects of the air-to-fuel ratio on the hydrogen yield. For this test, the DOC temperature, the hourly space velocity, and the fuel duration time were kept constant while the excess air ratio (λ) was varied from 0.54 to 1.11. The results are shown in Figure 5.1 and Figure 5.2 in terms of the peak hydrogen ppm value and the total hydrogen mass produced during the ten second fuel injection respectively. Both the peak ppm and the total hydrogen mass were plotted because the fuel injection time was not long enough to reach

a steady state value for hydrogen yield. Thus, a higher peak value for hydrogen did not necessarily correspond to a higher total mass.

The results generally showed that as the air-to-fuel ratio was decreased (direction of decreasing λ) the peak hydrogen yield and the total hydrogen mass generally increased. The peak hydrogen yield seemed to be relatively independent of the air-to-fuel ratio in the region of $0.54 \leq \lambda \leq 0.82$ while a significant drop was noticed when the air-to-fuel ratio was higher than stoichiometric (Figure 5.1). In contrast, a steady increase in the total hydrogen mass was observed as the air-to-fuel ratio was decreased. This seemed to suggest that $\lambda=0.54$ was the preferred condition for hydrogen generation.

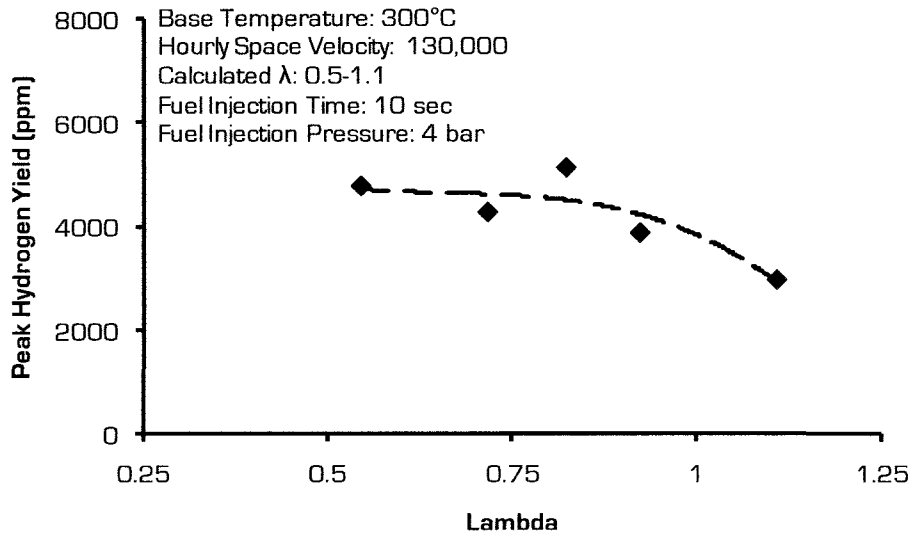

Figure 5.1: Effect of Air-to-Fuel Ratio on Peak Hydrogen Yield

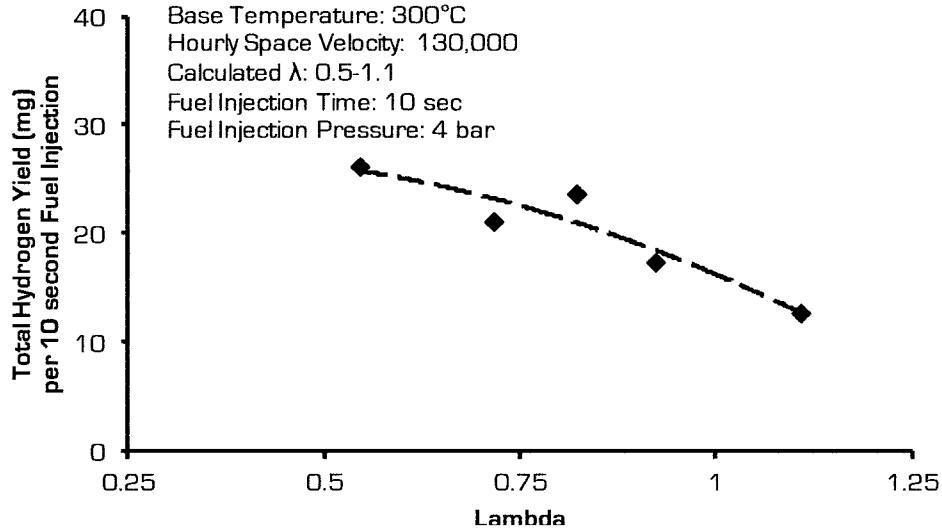

Figure 5.2: Effect of Air-to-Fuel Ratio on Total Hydrogen Mass

However, the air-to-fuel ratio was adjusted by injecting more diesel fuel at a given air amount while nitrogen was used to balance the flow rate. Thus, by lowering the air-to-fuel ratio, more fuel was available for reforming and more hydrogen was generally produced as a result. To account for fuel consumption, the total hydrogen mass in milligrams was normalized with respect to the total diesel fuel injected in grams (Figure 5.3). These results showed a relatively flat trend; however it was noticed that the minimum values occurred at the ends (λ=0.54 and λ=1.1) while the peak occurred at λ=0.82. Taking this into consideration, it was decided that the preferred condition for hydrogen generation was at approximately λ=0.82 and therefore, subsequent hydrogen generation tests were conducted at this air-to-fuel ratio.

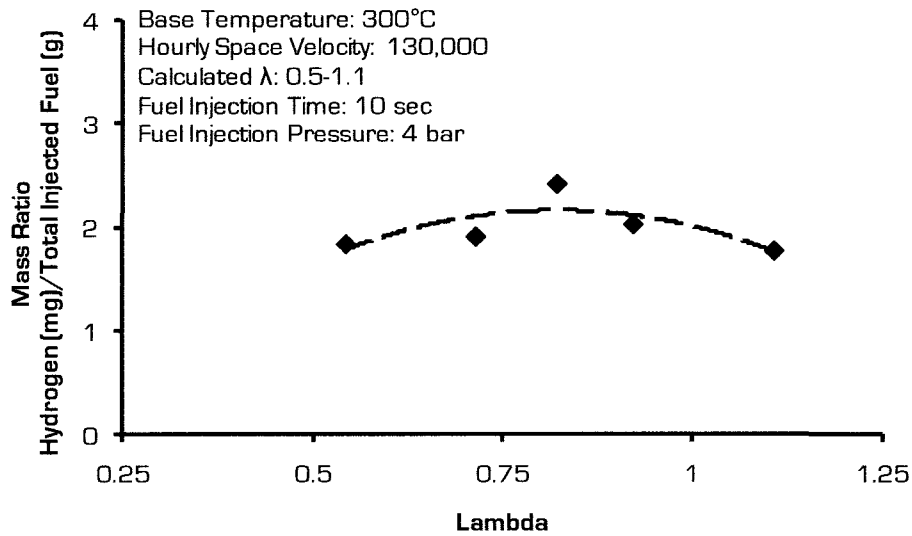

Figure 5.3: Normalized Hydrogen Yield as a Function of Air-to-Fuel Ratio

5.3 Temperature Effects

The effects of the DOC temperature on the hydrogen yield were investigated (Test 9). For this test, the air-to-fuel ratio, the hourly space velocity, the feed gas composition, and the fuel injection duration were kept constant while the DOC temperature was changed from 257°C to 373°C. The DOC temperature was controlled by the flow bench heater. The DOC temperature measurements were obtained from four evenly spaced thermocouples, as shown in Figure 5.4, distributed along the central flow axis of the DOC.

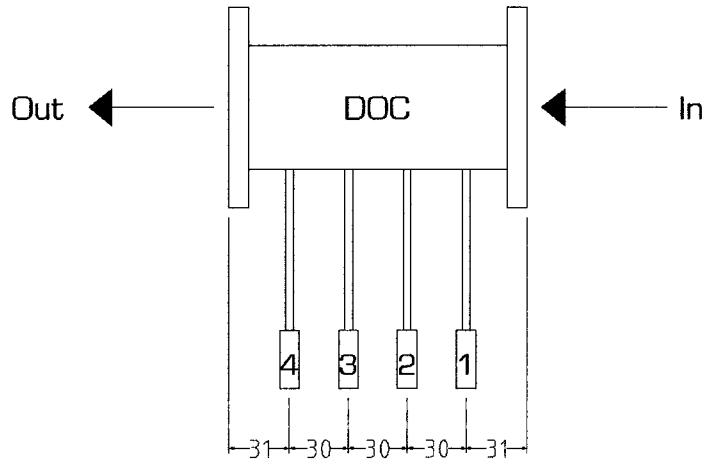

Figure 5.4: DOC Thermocouple Layout (Units in Millimetres)

The effects of the DOC temperature on the peak hydrogen yield and the total hydrogen mass are shown in Figure 5.5 and Figure 5.6 respectively. From the results it was observed that the effects of the DOC temperature on hydrogen production were significant. The pattern was the same in terms of both the peak hydrogen yield and the total hydrogen mass. At lower temperatures, below 275°C, no hydrogen production was noticed. At 257°C, the thermocouple readings indicated that the diesel fuel did not combust (Figure 5.7) and thus, the DOC temperature was too low for hydrogen generation. At 275°C, supplemental fuel combustion occurred, at least in the back half of the DOC, but hydrogen was not produced due to the still too low DOC temperatures, below 450°C (Figure 5.8).

As the DOC temperature was incrementally increased, a steady increase in hydrogen concentration was observed and when the DOC temperature was over 350°C, the hydrogen concentration exceeded 0.8%. What made this more impressive was that the fuelling was actually decreased as the temperature was increased as a result of maintaining a constant hourly space velocity and air-to-fuel ratio. By increasing the

temperature, the air density decreased and the air mass flow rate had to be reduced to maintain the same hourly space velocity, which is based on volume. Thus, the total injected fuel mass was also reduced to maintain the same air-to-fuel ratio. Nevertheless, even with reduced fuelling, the hydrogen concentration increased as a result of a higher DOC temperature. Compared to literature [20,21], where hydrogen yields between 10% and 20% are commonly reported, the maximum hydrogen yield achieved in this test (0.86%) was quite low. However, the purpose of this test was not focused on achieving high hydrogen yields but on investigating whether hydrogen can be generated under typical diesel exhaust temperatures and it was found that hydrogen can be generated but only at initial DOC temperatures exceeding 300°C.

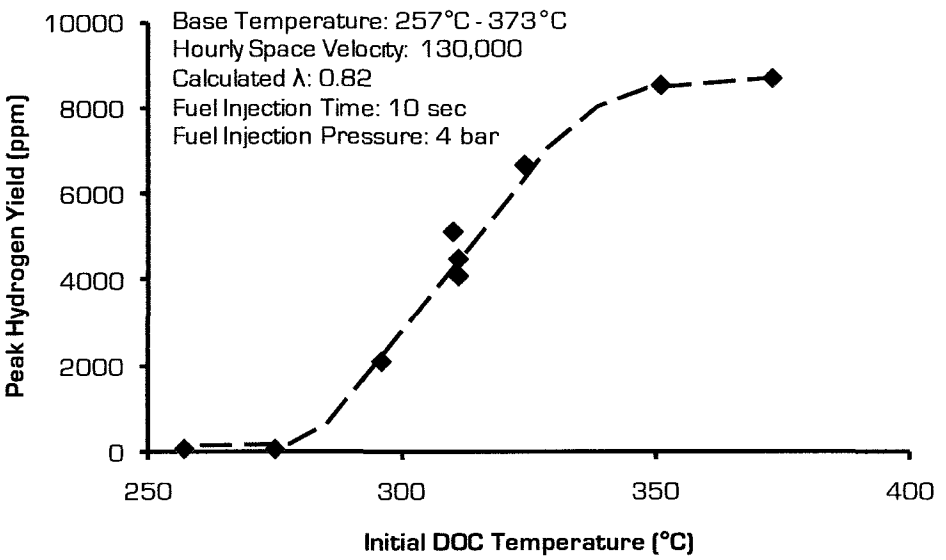

Figure 5.5: Effect of DOC Temperature on Peak Hydrogen Yield

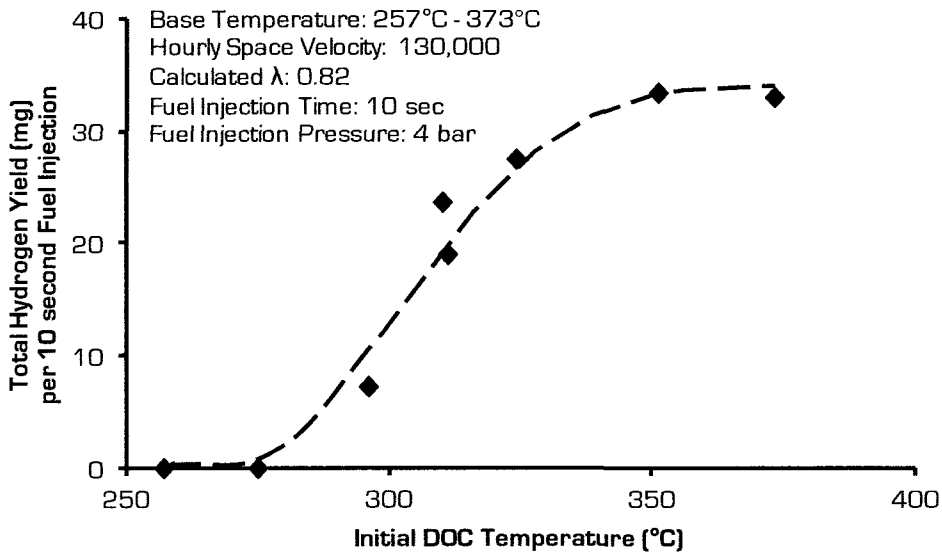

Figure 5.6: Effects of DOC Temperature on Total Hydrogen Mass

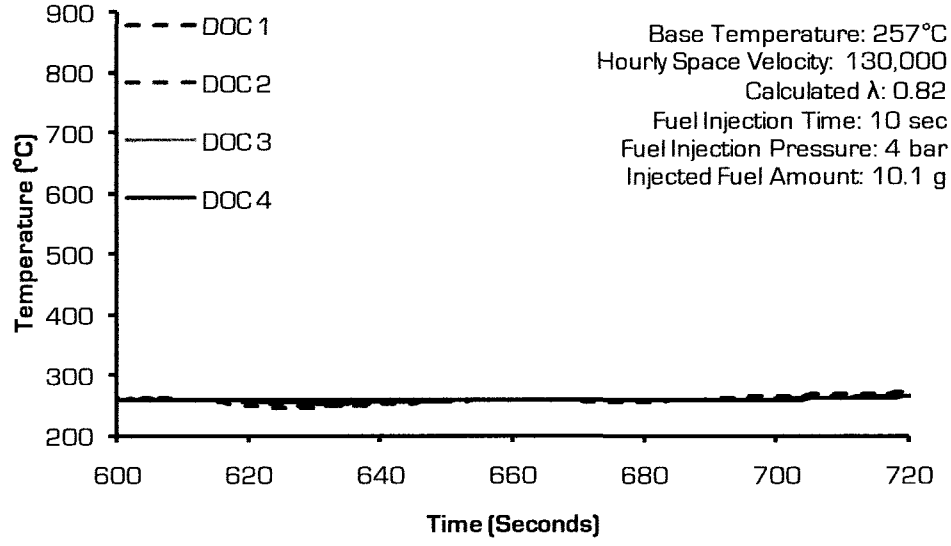

Figure 5.7: DOC Temperature Response at a 257°C DOC Temperature

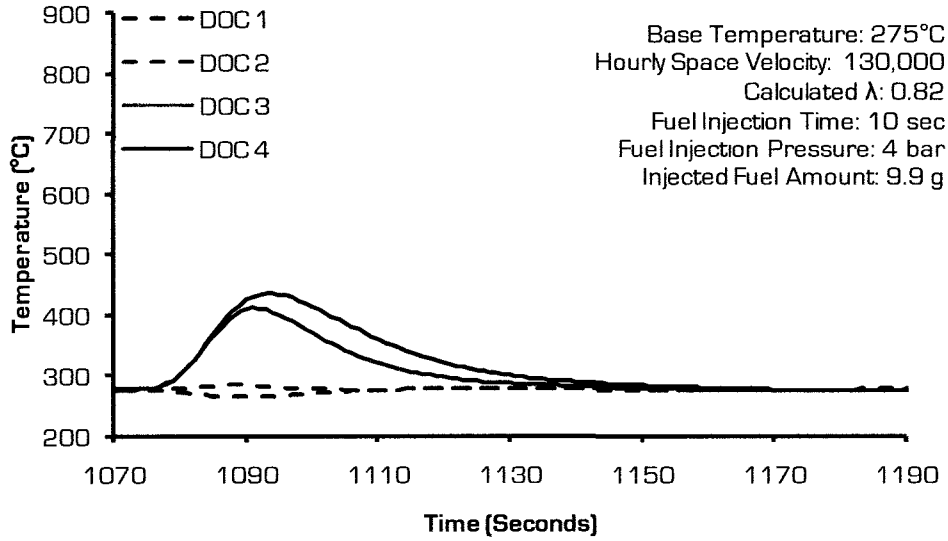

Figure 5.8: DOC Temperature Response at a 275°C DOC Temperature

Thus, it was concluded that the effect of increasing the DOC temperature was to increase the hydrogen production. At higher temperatures, the hydrogen producing reactions, such as the steam reforming reaction and the partial oxidation reaction, usually tend to be more preferred than at lower temperatures [22,31]. Conversely, the reverse water gas shift reaction typically consumes hydrogen at temperatures exceeding 700-750°C [31,32]. This could explain why the hydrogen concentration did not significantly increase from 350°C to 373°C. When fuel was injected at a DOC temperature of 350°C, the peak combustion temperature was 710°C (Figure 5.9) but when the fuel was injected at a DOC temperature of 373°C, the peak combustion temperature was 753°C (Figure 5.10). Thus, with the fuel injection at 373°C, the steam reforming and partial oxidation reactions produced slightly more hydrogen due to the slightly higher peak temperature compared to the fuel injection at 350°C. However, the reverse water gas shift reaction consumed moderate amounts of hydrogen with fuel injected at 373°C due to combustion temperatures exceeding 750°C.

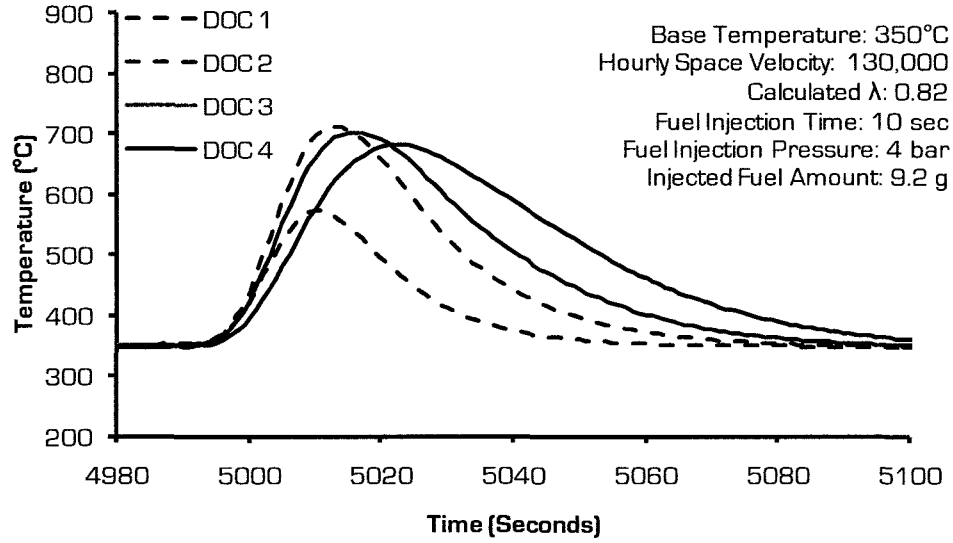

Figure 5.9: DOC Temperature Response at a 350°C DOC Temperature

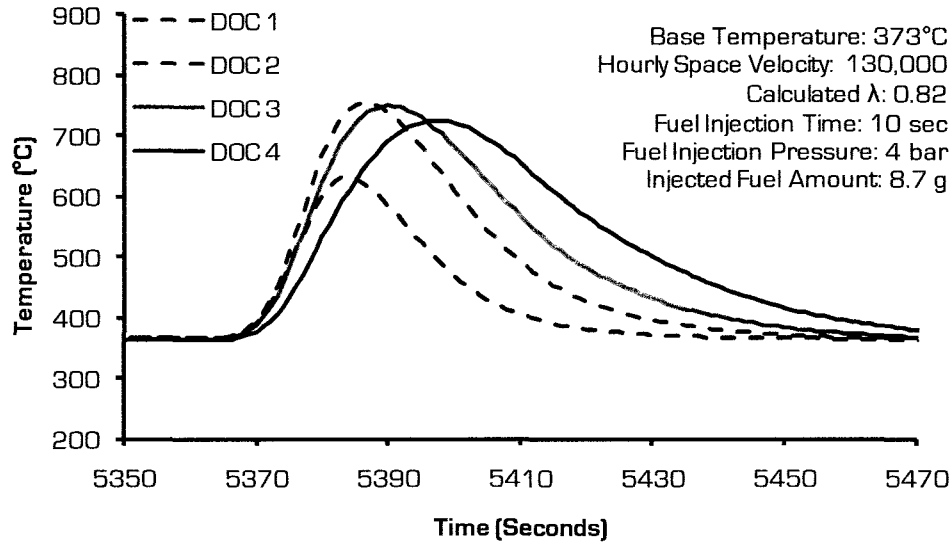

Figure 5.10: DOC Temperature Response at a 373°C DOC Temperature

5.4 Hourly Space Velocity Effects

The effects of the hourly space velocity on hydrogen generation were investigated utilizing the conditions shown for Test 10 in Table 2.1 and the flow bench set-up shown

in Figure 3.4. The DOC temperature, the air-to-fuel ratio, the feed gas composition, and the fuel injection duration were kept constant while the hourly space velocity was adjusted from 75,000 to 130,000. The hourly space velocity was defined as the number of DOC volumes of feed gas displaced in one hour of operation. The space velocity was calculated based on the DOC geometry and the data obtained from the DOC thermocouples and the MAF sensor.

The results in terms of the peak hydrogen yield are shown in Figure 5.11 and in terms of the total hydrogen mass in Figure 5.12. Both figures showed a similar trend; the hydrogen production generally increased as the hourly space velocity was increased. This was initially attributed to a higher fuelling amount at higher space velocities. The hourly space velocity was increased by increasing the feed gas mass flow rate. Thus, the total injected fuel mass was also increased to maintain a constant air-to-fuel ratio.

To account for this, the total hydrogen mass was normalized with respect to the total fuel injected as shown in Figure 5.13. This figure showed the same pattern as in the previous two figures. This led to the conclusion that increasing the hourly space velocity promoted hydrogen production. Literature suggested that this was because higher space velocities improved mass transfer within the DOC reactor [31,32] and further analysis of the temperature profiles also revealed that the peak DOC temperatures were higher when the space velocities were increased as shown in Figure 5.14 and Figure 5.15. Increasing hydrogen levels were observed from an HSV of 75,000 to 115,000 but at an HSV of 130,000 the hydrogen production decreased (Figure 5.16) compared to 115,000. A literature search indicated that at very high space velocities the improved mass transfer

effect was offset by low contact times between the reactants and the catalyst, thus producing less hydrogen [31].

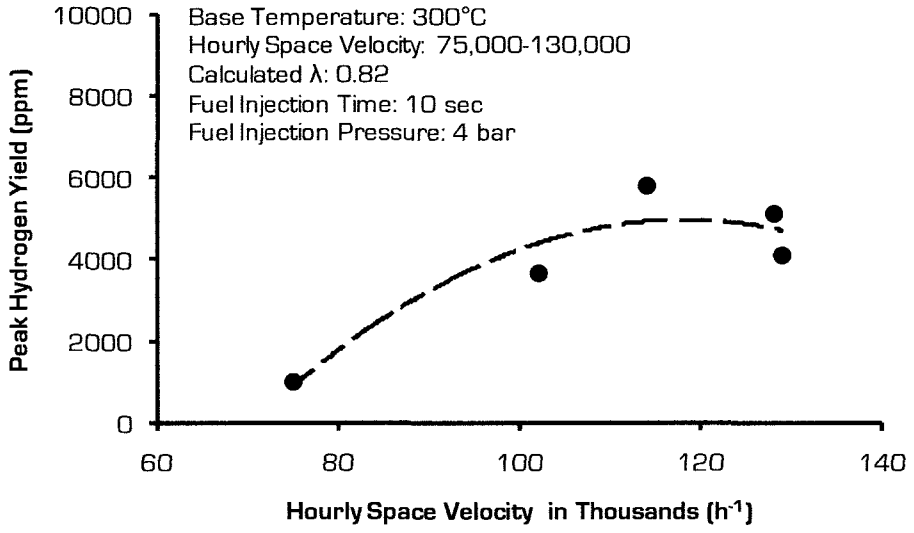

Figure 5.11: Effect of Hourly Space Velocity on Peak Hydrogen Yield

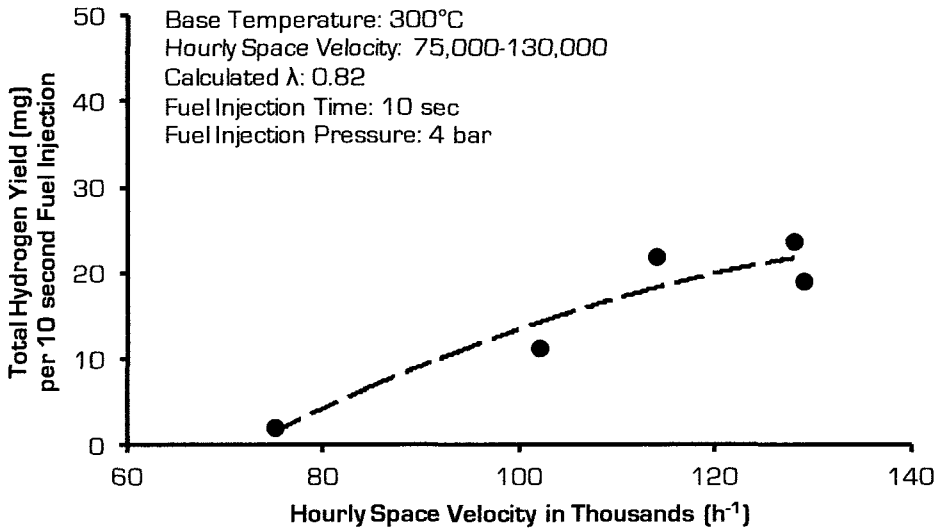

Figure 5.12: Effect of Hourly Space Velocity on Total Hydrogen Mass

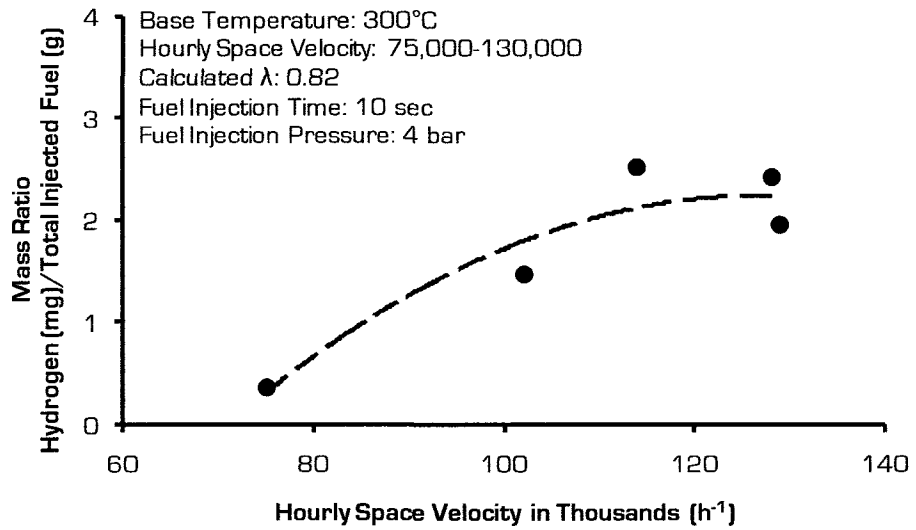

Figure 5.13: Normalized Hydrogen Yield as a Function of Hourly Space Velocity

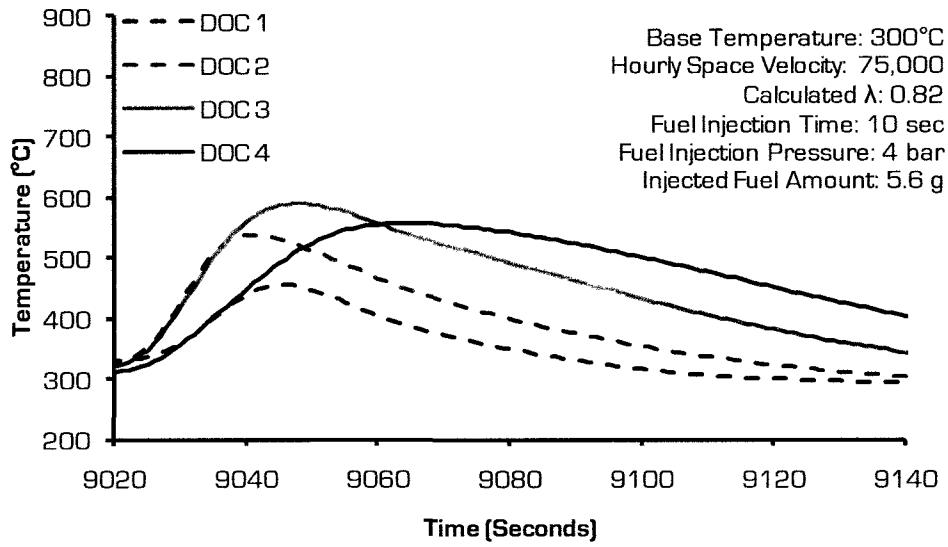

Figure 5.14: DOC Temperature Profile at a 75,000 Hourly Space Velocity

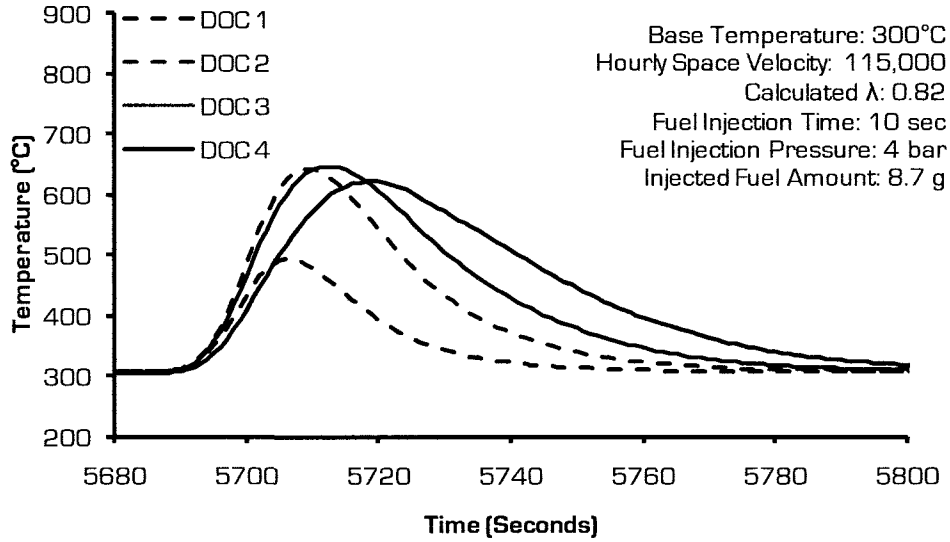

Figure 5.15: DOC Temperature Profile at a 115,000 Hourly Space Velocity

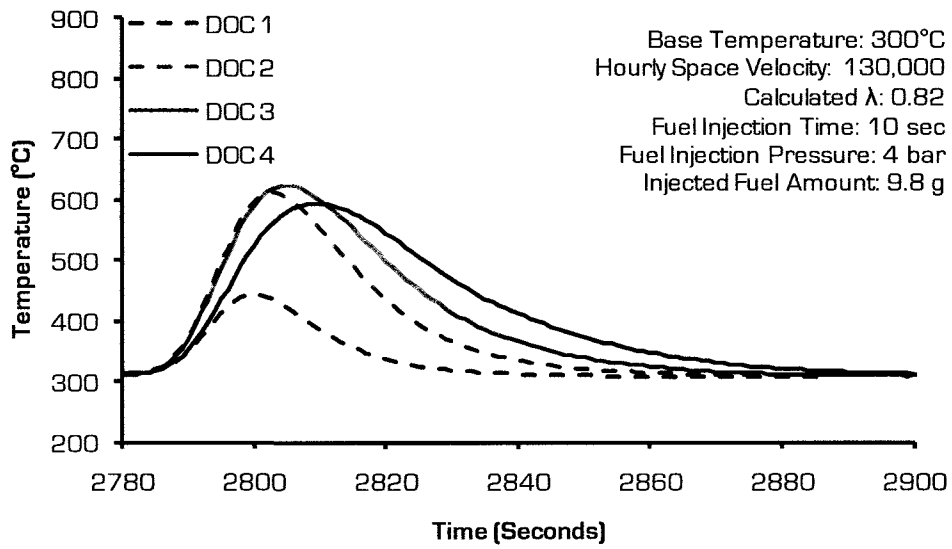

Figure 5.16: DOC Temperature Profile at a 130,000 Hourly Space Velocity

5.5 Fuel Injection Duration Effects

The hydrogen generation tests were concluded with an investigation of the effects of the fuel injection duration on the hydrogen production of the DOC. The test

conditions were shown in Table 2.1 as Test 11. For these tests, the air-to-fuel ratio, the DOC temperature, and the hourly space velocity were kept constant and the fuel injection duration was changed from 10 seconds to 15 seconds. The process was repeated at three different hourly space velocities.

The results are shown in Figure 5.17 and Figure 5.18. It was observed that as the fuel injection duration was prolonged, the peak hydrogen yield and the total hydrogen mass increased. This was true at all three hourly space velocities. At first, this was thought to be the effect of injecting a greater amount of fuel due to a longer injection duration. Therefore, the results were normalized with respect to the injected fuel (Figure 5.19). It was evident that the longer fuel injection duration still produced significantly more hydrogen per gram of injected fuel at all hourly space velocities.

Further analysis was undertaken and it was found that the fuel injection duration had an effect on the DOC temperature profile. The ten second fuel injection duration temperature profile (Figure 5.15) was compared with the fifteen second fuel injection duration temperature profile (Figure 5.20). It was observed that significantly higher peak combustion temperatures were achieved with the longer injection duration; with a ten second fuel injection the peak temperature was 640°C but with a fifteen second fuel injection the peak temperature was 860°C.

At higher temperatures, the steam reforming and the partial oxidation reactions are generally more favoured than at lower temperatures [22]. This was the reason why more hydrogen was produced with a longer injection duration. It was previously mentioned that temperatures in excess of 700°C-750°C tended to inhibit the water gas shift reaction and thus reduce the hydrogen production via this mechanism. However, in

this instance, it seemed that the additional hydrogen produced by the steam reforming and the partial oxidation reactions, due to higher temperatures, more than offset the reduced hydrogen production from the water gas shift mechanism.

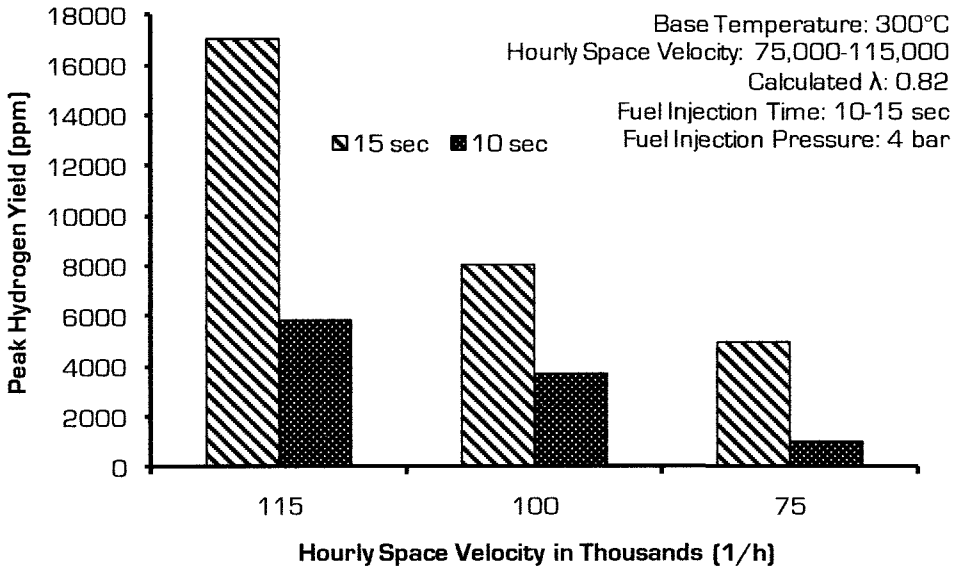

Figure 5.17: Effect of Fuel Injection Duration on Peak Hydrogen Yield

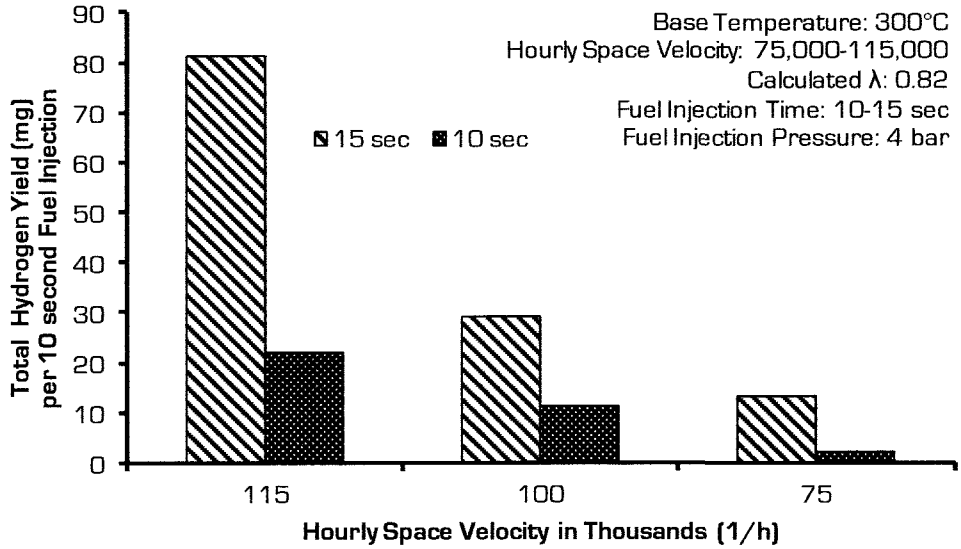

Figure 5.18: Effect of Fuel Injection Duration on Total Hydrogen Mass

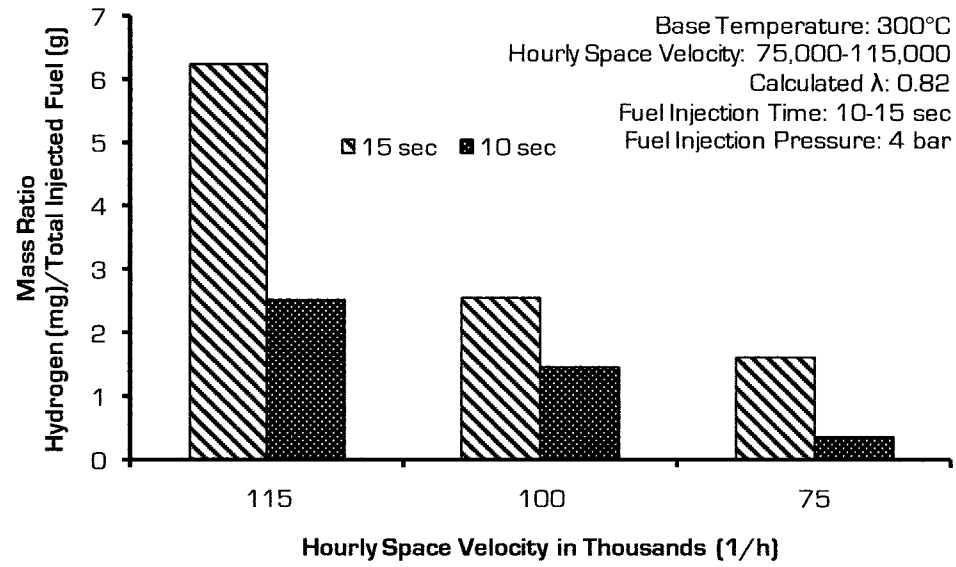

Figure 5.19: Effect of Fuel Injection Duration on Normalized Hydrogen Yield

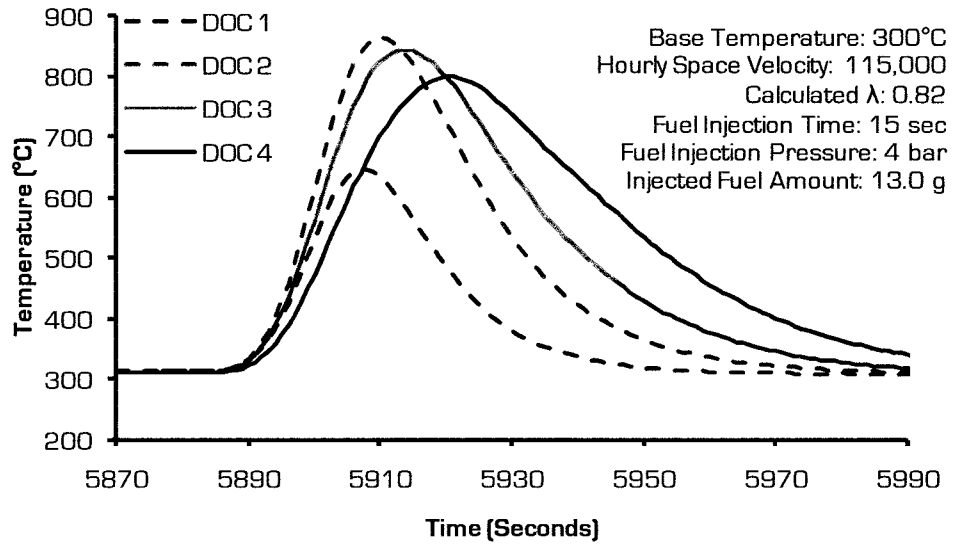

Figure 5.20: Temperature Profile with a 15 Seconds Fuel Injection Duration

CHAPTER 6: FLOW REVERSAL TESTS

6.1 Motivation for Flow Reversal

The previous tests (Tests 8-11) investigated the effects of different parameters on hydrogen production in a DOC fuel reformer. It was observed that the effects of temperature were significant. It was shown in Test 9 that no hydrogen was produced below an initial DOC temperature of 275°C while at higher initial DOC temperatures, over 300°C, there was a steady increase in hydrogen production. Furthermore, the effects of other parameters, such as fuel injection duration and hourly space velocity, on hydrogen production were usually related to their effects on temperature. It was concluded that maintaining an optimal DOC temperature was vital to hydrogen production. Literature [14,33] suggested that flow reversal can provide temperature retention benefits for a reactor. Thus, a flow reversal system was proposed for effective hydrogen generation at low exhaust gas temperatures. To demonstrate the effectiveness of a flow reversal system of maintaining a desired temperature range, a numerical investigation was carried out. This was followed by a brief empirical investigation to confirm the numerical trends.

6.2 Numerical Modelling Set-up

The numerical investigation was done in C++ programming language. The monolith temperatures were calculated by equations derived from heat transfer theory and energy balance equations. The monolith system was modelled as a one-dimensional single channel system. Only the heat transfer modes of convection, between the gas and

the solid, and conduction, along the axial direction of the solid, were considered. Radial conduction and radiation were assumed to be negligible. Energy addition was modelled as surface energy generation and was distributed evenly along the length of the monolith.

The thermal and geometric properties of the monolith (Table 6.1) were assumed to be independent of the monolith temperature. It was also assumed that the flow was uniformly distributed among all of the channels of the monolith. The aforementioned assumptions were consistent with studies done by other authors [14,33]

Table 6.1: Monolith Properties for the Numerical Investigation

Monolith Properties	
Thermal Conductivity	11.7 W/m·K
Monolith Density	1700 kg/m^3
Heat Capacity	800 J/kg·K
Monolith Diameter	0.100 m
Monolith Length	0.304 m
Cells per Square Inch	400

With these assumptions, the first law of thermodynamics and heat transfer equations were utilized to derive the governing equation for the energy balance of the monolith solid as shown in Equation 6.1. The variables were defined in the nomenclature section.

$$\rho_s A_s c_s \frac{\partial Ts}{\partial t} = A_s k_s \left(\frac{\partial^2 Ts}{\partial x^2}\right) - c_h h\left(T_s - T_g\right) + \dot{q} \qquad (6.1)$$

From this differential equation, finite difference formulas were used to approximate the derivative terms and to derive an equivalent numerical equation solvable by a programming language.

First order forward finite difference:

$$\frac{\partial Ts}{\partial t} = \frac{Ts_m^{n+1} - Ts_m^n}{\Delta t} \tag{6.2}$$

Second order forward finite difference:

$$\frac{\partial^2 Ts}{\partial x^2} = \frac{Ts_{m+2}^n - 2Ts_{m+1}^n + Ts_m^n}{\Delta x^2} \tag{6.3}$$

Second order central finite difference:

$$\frac{\partial^2 Ts}{\partial x^2} = \frac{Ts_{m+1}^n - 2Ts_m^n + Ts_{m-1}^n}{\Delta x^2} \tag{6.4}$$

Second order backward finite difference:

$$\frac{\partial^2 Ts}{\partial x^2} = \frac{Ts_m^n - 2Ts_{m-1}^n + Ts_{m-2}^n}{\Delta x^2} \tag{6.5}$$

The governing equation for the first node of the monolith:

$$Ts_m^{n+1} = \lambda(Ts_{m+2}^n - 2Ts_{m+1}^n) + (1 + \lambda - \beta)Ts_m^n + \beta Tg_m^n + \delta\dot{q} \tag{6.6}$$

The governing equation for the middle nodes of the monolith:

$$Ts_m^{n+1} = \lambda(Ts_{m-1}^n + Ts_{m+1}^n) + (1 - 2\lambda - \beta)Ts_m^n + \beta Tg_m^n + \delta\dot{q} \tag{6.7}$$

The governing equation for the last node of the monolith:

$$Ts_m^{n+1} = \lambda(Ts_{m-2}^n - 2Ts_{m-1}^n) + (1 + \lambda - \beta)Ts_m^n + \beta Tg_m^n + \delta\dot{q} \tag{6.8}$$

Where:

$$\alpha = \frac{k_s}{\rho_s c_s},\ \beta = \frac{c_h h \Delta t}{\rho_s c_s A_s},\ \delta = \frac{\Delta t}{\rho_s c_s A_s \Delta x},\ \lambda = \frac{\alpha \Delta t}{\Delta x^2}$$

Heat transfer equations and finite difference formulas were also utilized to develop the governing equation for the gas phase.

Energy balance:

$$\dot{m}_g \frac{\partial(c_{pg}Tg)}{\partial x} = c_h h(Ts\text{-}Tg) \tag{6.9}$$

First order forward finite difference:

$$\frac{\partial(c_{pg}Tg)}{\partial x} = c_{pg}\left(\frac{Tg^n_{m+1}\text{-}Tg^n_m}{\Delta x}\right) \tag{6.10}$$

The governing equation for the gas phase temperature:

$$Tg^n_{m+1} = Tg^n_m + \frac{c_h h \Delta x(Ts^n_m\text{-}Tg^n_m)}{\dot{m}_g c_{pg}} \tag{6.11}$$

6.3 Results of the Numerical Investigation

The numerical tests compared the thermal response of a warm unidirectional flow monolith and a warm flow reversal monolith exposed to a cold feed gas. It was assumed that the initial temperature of the monolith was 600°C and that the feed gas temperature was 200°C. The time for the monolith to cool down below 300°C was investigated. A ten second cycling period was chosen for the flow reversal system. The results of the numerical investigation are shown in Figure 6.1 for a unidirectional flow case and in Figure 6.2 for a flow reversal case.

With unidirectional flow, the dependence of the monolith temperature on the feed gas temperature was evident. The monolith was initially at 600°C but after only ten second of exposure to 200°C feed gas, it was noticed that the front 10% of the monolith had already cooled down below 300°C. After 40 seconds of exposure, 60% of the

monolith was cooled down below 300°C and after 80 seconds of exposure, the monolith had already reached thermal equilibrium and was entirely cooled below 300°C.

Under the same temperatures and flow conditions, it was noticed that the flow reversal monolith was less dependent on the feed gas temperature than the unidirectional flow monolith. The thermal response with flow reversal was identical to the unidirectional flow response for the first ten seconds of operation. However, after ten seconds, the flow direction was switched and it was noticed that the front of the monolith started to heat up while the rear of the monolith started to cool down. The biggest advantage seemed to be that the temperature drop was almost negligible at the center of the monolith. After the next ten seconds, the flow direction was switched again and the front of the monolith was cooling down again while the rear was heating back up.

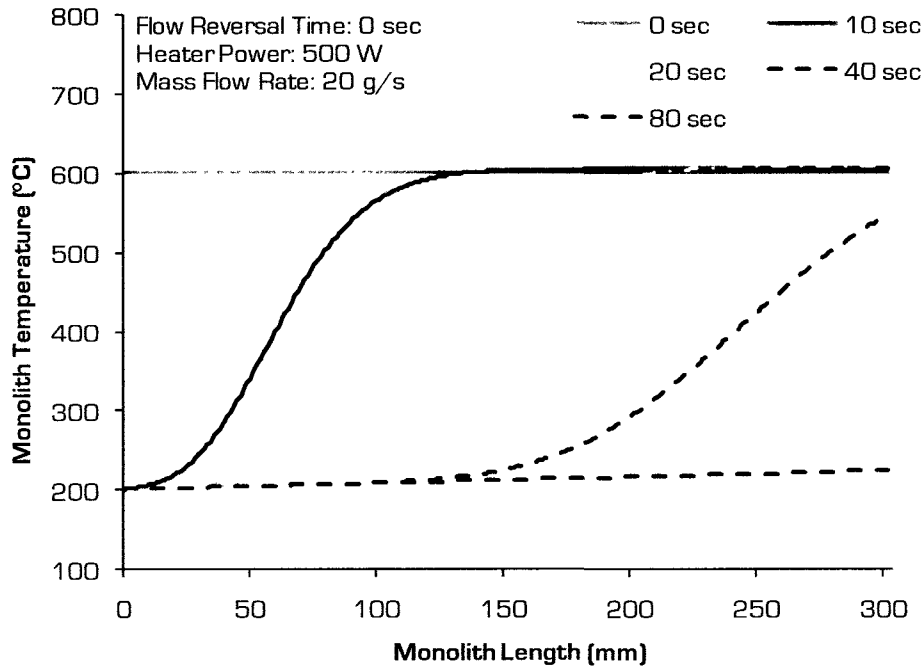

Figure 6.1: Thermal Response of the Monolith with Unidirectional Flow

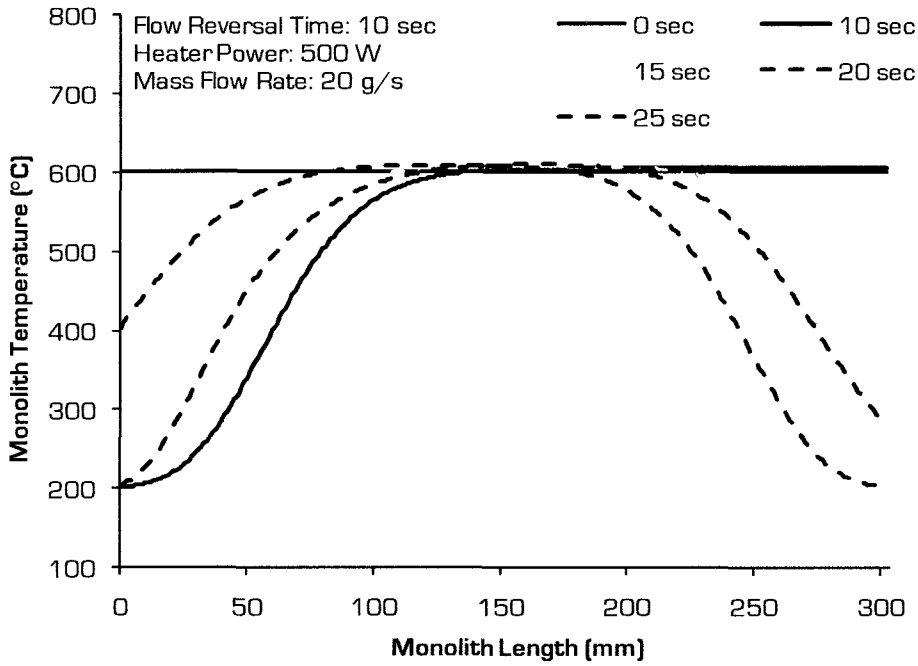

Figure 6.2: Thermal Response of the Monolith with Ten Second Flow Reversal

A direct comparison of the unidirectional flow monolith and the flow reversal monolith is shown in Figure 6.3. It was observed that after 20 seconds of operation, there was already an advantage to using the flow reversal system. After 20 seconds, 68% of the unidirectional flow monolith was above 300°C while 85% of the flow reversal monolith was above 300°C. The advantage of flow reversal was further witnessed from the temperature profiles after half an hour of exposure to low temperature feed gas. The unidirectional flow monolith had already reached thermal equilibrium after 80 seconds of exposure (Figure 6.1) but Figure 6.3 showed that 40% of the flow reversal monolith was still above 300°C even after half an hour of exposure. Thus, the numerical investigation clearly demonstrated the temperature retention advantage of a flow reversal system compared to a unidirectional flow system.

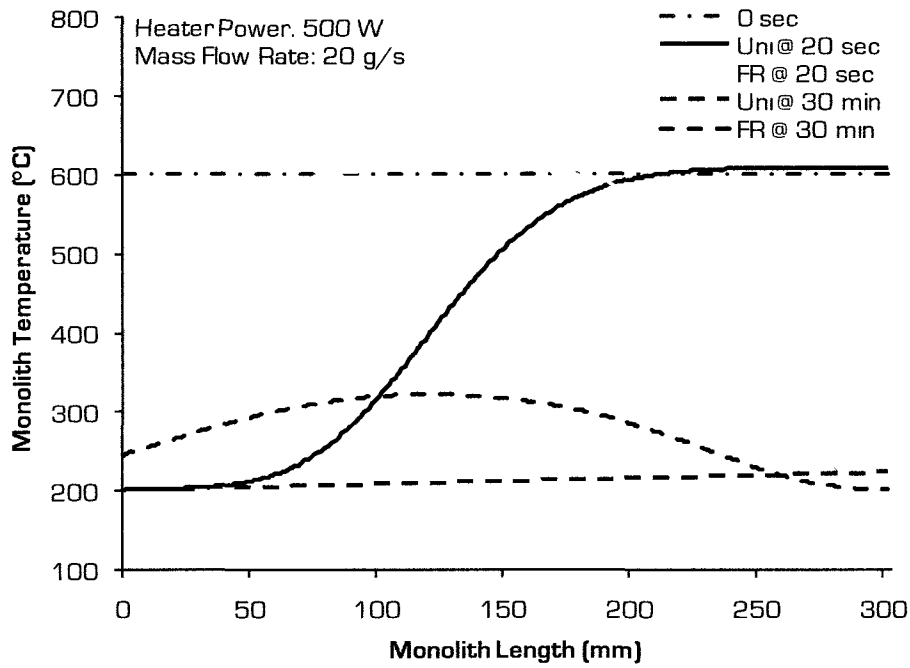

Figure 6.3: Unidirectional Flow (Uni) vs. Flow Reversal (FR) - Cooling

6.4 Adaptive Flow Reversal Control

The temperature retention ability of the flow reversal monolith was demonstrated in the previous section and it was shown to be of advantage when a warm monolith was being cooled by a cold feed gas. However, the temperature retention ability of the flow reversal monolith could be a disadvantage if a cold monolith was being heated by a warm feed gas. To demonstrate this, numerical tests were done with an initially cold monolith at 200°C exposed to a feed gas at 400°C. The time for the monolith to heat up to 300°C was investigated.

Figure 6.4 showed that the unidirectional flow monolith reached equilibrium after 80 seconds of operation. The entire monolith was heated up to 300°C by 50 seconds of exposure to warm feed gas. Conversely, Figure 6.5 showed that after 80 second of

operation, 42% of the flow reversal monolith was still below 300°C. This was because of the temperature retention ability of the flow reversal monolith. With flow reversal, the central section of the monolith was less responsive to the feed gas temperature and while this was an advantage with a hot monolith exposed to a cold feed gas, it was a disadvantage with a cold monolith exposed to a warm feed gas. This led to the conclusion that a unidirectional flow monolith outperformed the flow reversal monolith by heating up more quickly to the desired temperature.

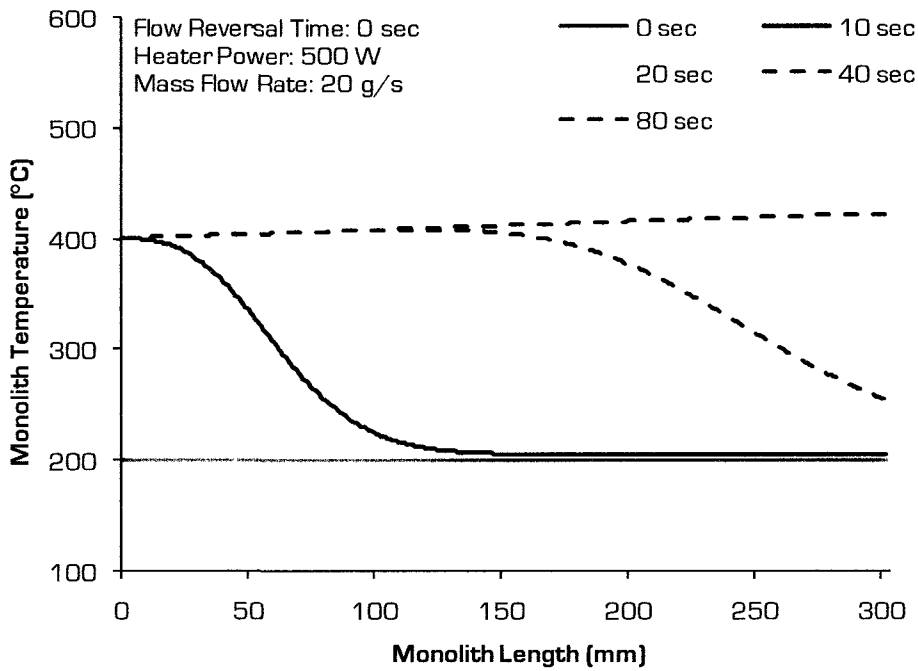

Figure 6.4: Thermal Response of a Unidirectional Flow Monolith to Heating

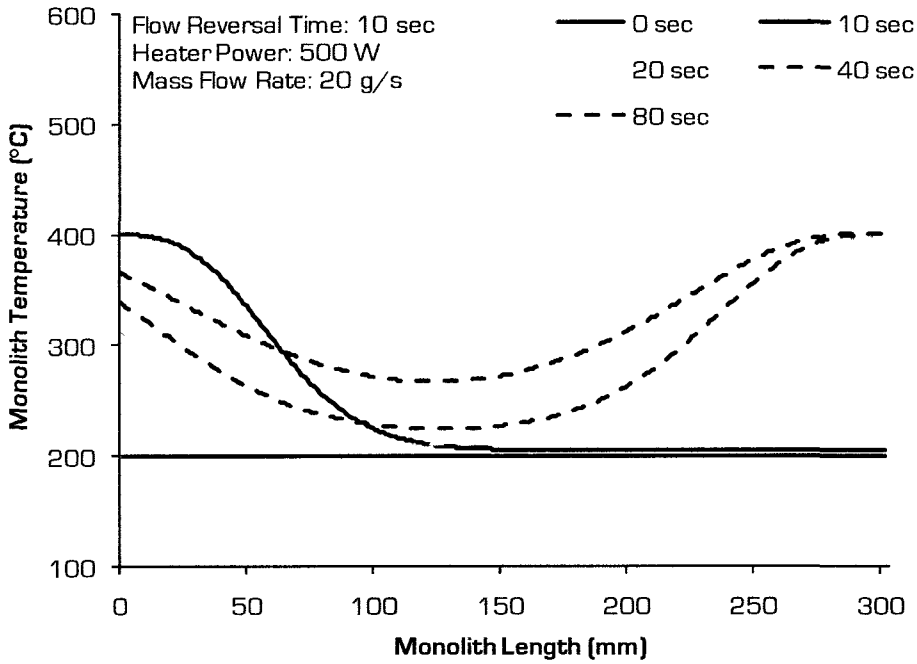

Figure 6.5: Thermal Response of a Flow Reversal Monolith to Heating

Further analysis found that after extended exposure to warm feed gas, the flow reversal monolith reached higher temperatures than the unidirectional flow monolith. Figure 6.6 showed that the entire unidirectional flow monolith was in the range of 400°C to 420°C while the flow reversal monolith exceeded temperatures of 500°C, even though the feed gas temperature was only 400°C. This would be an advantage for on-board hydrogen generation where temperatures over 500°C are generally required. However, high monolith temperatures could also present a disadvantage because uncontrolled supplemental fuel or engine-out hydrocarbon oxidation could result in monolith temperatures in excess of 1000°C, potentially leading to monolith overheating. Thus, an adaptive control flow reversal strategy was proposed to provide faster heating of the monolith and to maintain the monolith within a desired temperature window.

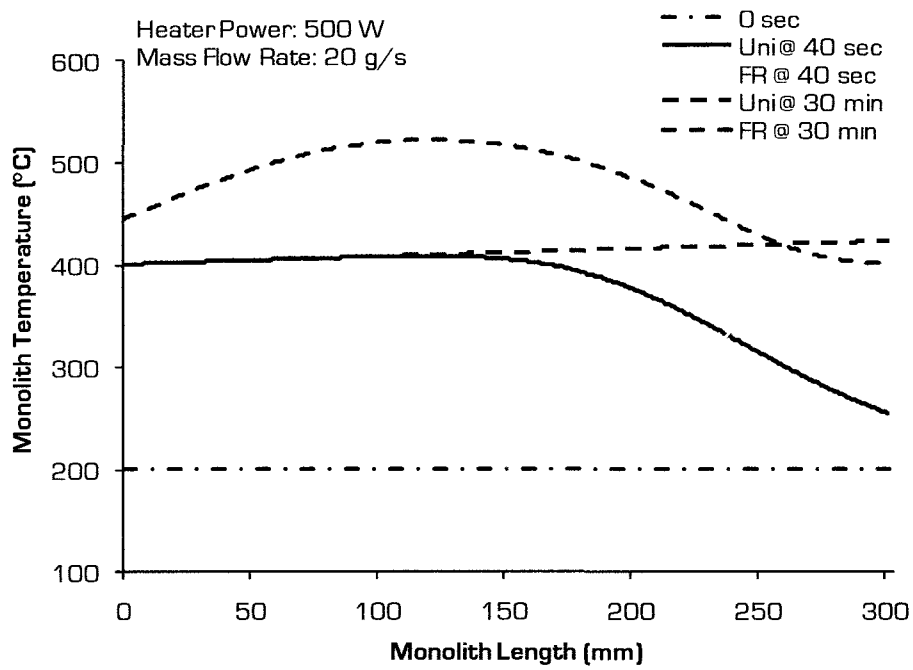

Figure 6.6: Unidirectional Flow (Uni) vs. Flow Reversal (FR) - Heating

To investigate the adaptive control strategy, the numerical code was adjusted to include an adaptive control scheme as shown in Table 6.2. With this strategy, the flow reversal time would be set to zero seconds if the minimum temperature in the monolith was less than 300°C, to heat up the monolith as fast as with unidirectional flow, or if the maximum temperature inside the monolith was higher than 450°C, to maintain the monolith temperature within the hypothetically desired range of 300°C to 450°C. Within the desired temperature range, the flow reversal cycle time was set to ten seconds.

The results (Figure 6.7) showed that the addition of the adaptive control strategy improved the thermal response of the flow reversal monolith. With adaptive control, the flow reversal monolith responded like a unidirectional flow monolith for the first 50 seconds until it was thoroughly heated to above 300°C. At that point, the flow reversal cycle time was switched to ten seconds and the flow reversal monolith continued to heat

up. After 80 second of exposure, the entire monolith was at about a 400°C temperature while without adaptive control, 42% of the monolith was still below 300°C (Figure 6.5).

Table 6.2: Adaptive Control Strategy for Heating a Flow Reversal Monolith

Temperature Range	Flow Reversal Time
Tmax > 450°C	0 seconds
Tmin < 300°C	0 seconds
Else	10 seconds

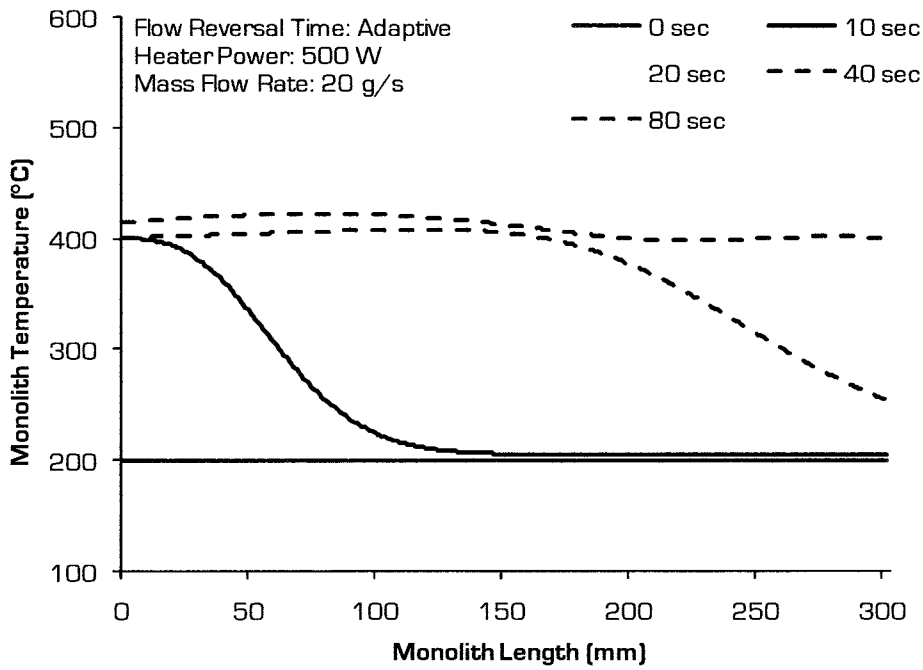

Figure 6.7: Improved Thermal Response with Adaptive Control

The advantage of the adaptive control strategy was further observed in Figure 6.8. Previously, without adaptive control the maximum temperature of the flow reversal monolith was 522°C and 40% of the monolith was at a temperature over 500°C. With

adaptive control the maximum temperature of the monolith was 460°C. This was accomplished by switching the flow reversal time to zero, thereby cooling the monolith, once a temperature over 450°C was detected. When the maximum temperature dropped below 450°C, the flow reversal time was switched back to ten seconds and the monolith heated back up. This process continued so that throughout half an hour of operation, the entire monolith temperature remained within a temperature range of 400°C to 460°C. Thus, the adaptive control strategy was shown to benefit the flow reversal monolith by enabling it to heat up more quickly and by maintaining the monolith temperature within the hypothetically desired temperature range.

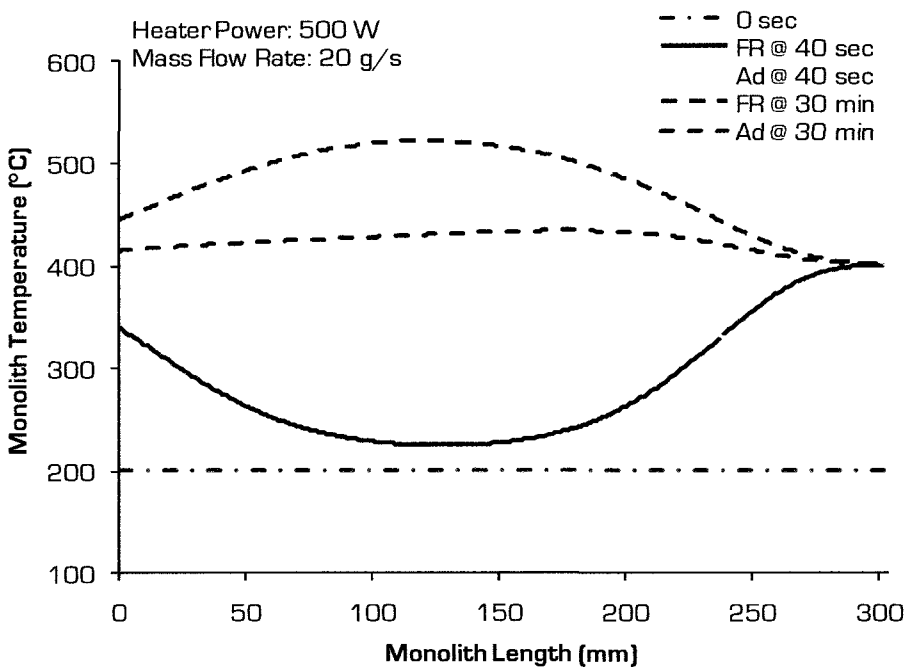

Figure 6.8: Comparison of Flow Reversal (FR) and Adaptive Control (Ad) Monoliths

6.5 Confirmation with Empirical Tests

A brief unoptimized empirical investigation was carried out to confirm the trends observed in the numerical investigation. For the empirical tests, a DOC monolith was installed inside a flow reversal canister which was then installed on the flow bench set-up as shown in Figure 3.5. Further details, including the flow reversal thermocouple set-up, were presented in the experimental-set up section.

The empirical tests compared the thermal response of a cold unidirectional flow DOC and a cold flow reversal DOC to heating. The initial temperature of the DOC monolith was 25°C and the DOC was then heated by two heating elements placed inside the canister as shown in Figure 3.13. The heater power was first set at 200 W and later increased to 500 W. It should be noted that due to their location, the heating elements only heated Side B (Figure 3.13) of the DOC for the unidirectional flow tests but for the flow reversal tests both Side A and Side B were heated. This meant that the tests were biased in favour of the unidirectional flow DOC because it used the same heating power but for only half the DOC volume compared to the flow reversal tests.

The thermal response of the unidirectional flow DOC to 200 W of heating is shown in Figure 6.9. The figure showed that the initial temperature of the DOC was 25°C to 30°C. When heating was applied, Side B started to heat up while Side A remained at about 25°C throughout the tests. For Side B, it was observed that the thermal response was similar to what was observed in the numerical investigation (Figure 6.4). Initially, in the first five minutes of heating, the front of the DOC (front of side B) started to heat up quickly, experiencing a temperature increase of 74°C, while the back had a temperature increase of only 16°C.

In the next five minutes, the temperature rise at the front of the DOC was much slower, only a 21°C increase, while the back experienced a temperature rise of 57°C. After 30 minutes of heating, the DOC temperature approached steady state with temperatures of about 150°C throughout the DOC. This corresponded to a maximum temperature increase of 120°C after 30 minutes of operation. The tests were repeated with heating at 500 W. The thermal response of the DOC with 500 W heating (Figure 6.10) followed the same trend as with 200 W.

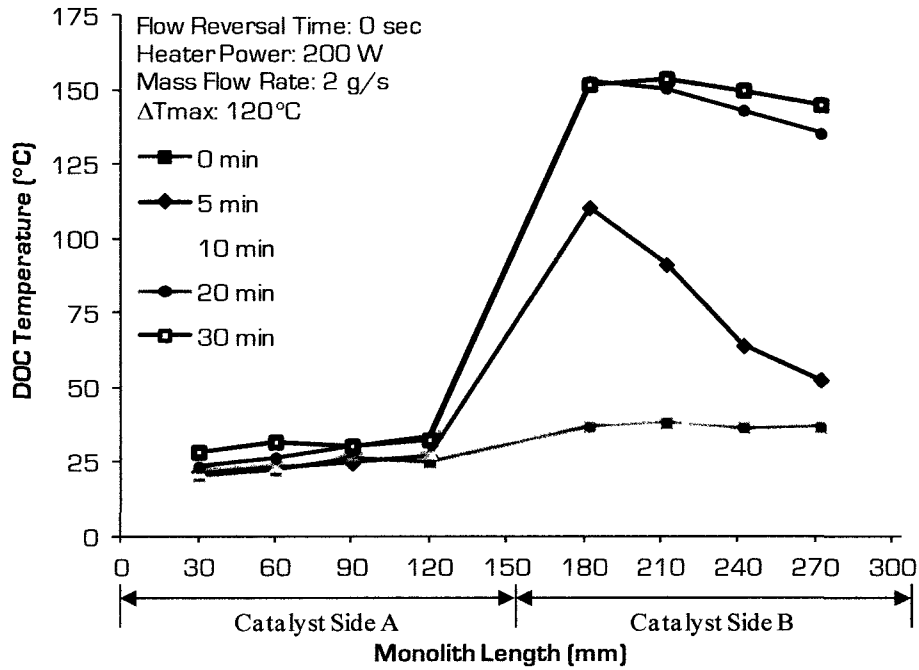

Figure 6.9: Heating a Unidirectional Flow DOC with 200 W

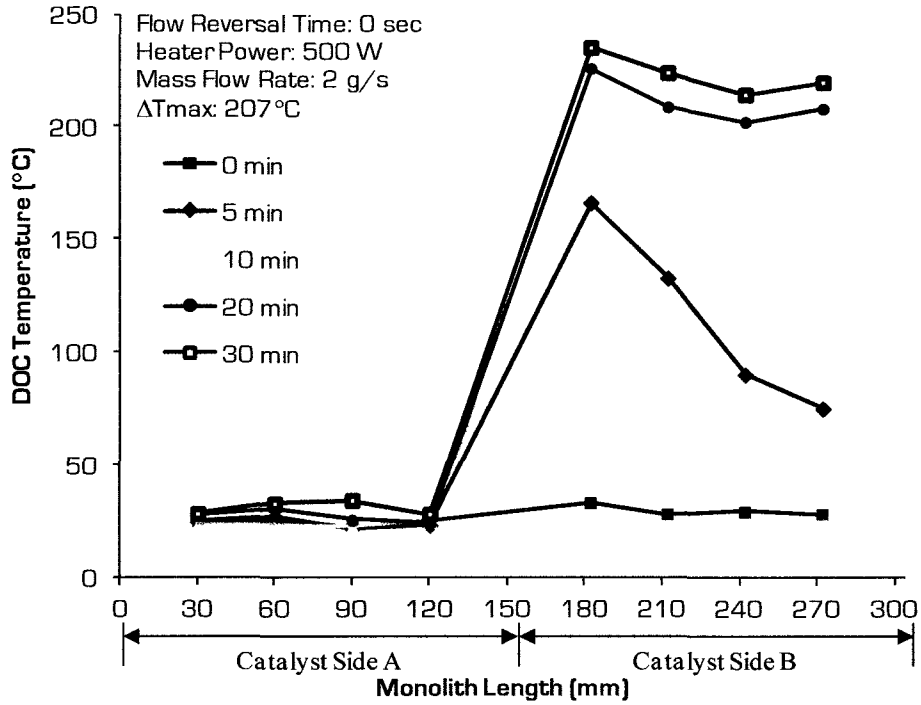

Figure 6.10: Heating a Unidirectional Flow DOC with 500 W

The tests were repeated with a flow reversal DOC operating at a ten second flow reversal time. The results for 200 W heating are shown in Figure 6.11 and for 500 W heating in Figure 6.12. It was observed that the thermal response of the empirical tests matched the thermal response of the numerical tests but that the maximum temperatures occurred in different locations. In the numerical tests, the maximum temperature occurred at the ends of the reactor while in the empirical tests the maximum temperature occurred at the centre of the reactor. This was attributed to the location of the heaters in the empirical tests. In the numerical tests, the hot feed gas entered the reactor from its ends to provide a direct comparison between the temperature response of a flow reversal reactor and a unidirectional flow reactor. Thus, in the numerical tests, the end sections of the reactor initially experienced the fastest temperature rise. Conversely, in the empirical

tests, the location of the heating elements was restricted due to the availability of hardware. Thus, in the empirical tests, the central sections of the DOC were exposed to the hot feed gas before the end sections and this was why the maximum temperature occurred in the central sections of the DOC.

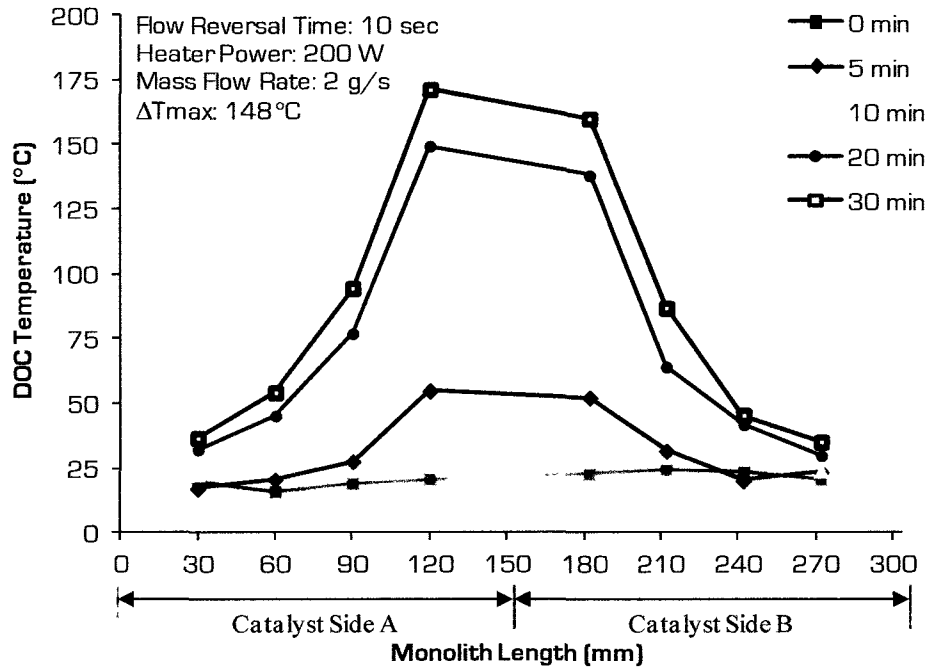

Figure 6.11: Heating a Flow Reversal DOC with 200 W

Nevertheless, the empirical tests confirmed the advantage of flow reversal compared to unidirectional flow. For both the 200 W and 500 W settings, the flow reversal DOC had at least a 23% higher maximum temperature rise at steady state compared to the unidirectional flow DOC. This was accomplished despite the fact that the unidirectional flow DOC utilized the same heating power but heated only half the volume compared to the flow reversal DOC. However, the weakness of the flow reversal system was also observed because the unidirectional flow DOC was able to heat up faster than the flow reversal DOC as can be witnessed from the temperature profiles at five

minutes of heating. Overall, the empirical results were consistent with the numerical trends. Therefore, it was concluded that flow reversal, especially with adaptive control, would be of benefit for on-board hydrogen generation due to its ability to retain more suitable temperatures compared to traditional unidirectional flow systems.

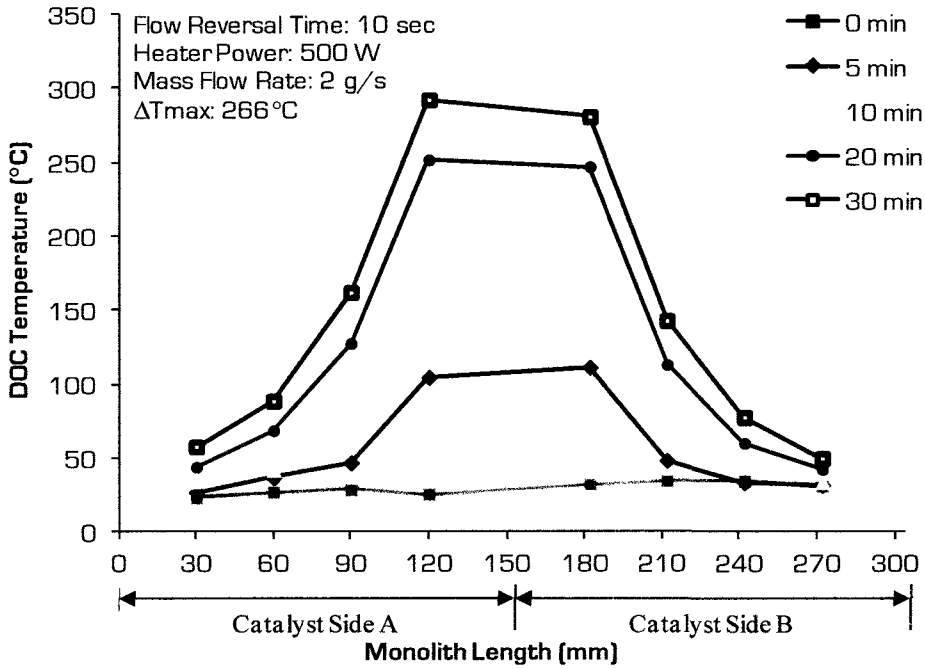

Figure 6.12: Heating a Flow Reversal DOC with 500 W

CHAPTER 7: CONCLUDING REMARKS

7.1 Summary of the Test Results

A long breathing strategy, capable of providing supplemental energy savings, was proposed for a diesel lean NOx trap. The long breathing strategy was investigated on a flow bench set-up. Initially, a feed gas consisting of air and NOx was used. The tests were later repeated with a simulated feed gas consisting of carbon dioxide, water, air, and NOx. The tests results led to the following conclusions:

- The adsorption time increased exponentially when the feed gas NOx level was reduced due to an improved LNT storage efficiency
- Even with an unoptimized catalyst, the adsorption of the long breathing LNT exposed to 50 ppm of NOx was consistently over three times longer than the adsorption of a conventional LNT exposed to 110 ppm of NOx
- Due to longer adsorption, the long breathing LNT exposed to 50 ppm of NOx was able to achieve supplemental fuel savings, in excess of 70%, compared to a conventional LNT exposed to 110 ppm of NOx
- At a sample engine test condition, it was calculated that the long breathing LNT strategy had a lower overall fuel consumption (372.6 g/hr) than the conventional LNT strategy (414.3 g/hr) and the low temperature combustion strategy (374.5 g/hr); however, if the LNT fuelling could be reduced to below 4.7 grams per regeneration than the conventional LNT strategy would have had the lowest fuel consumption at this engine condition

Literature suggested that hydrogen addition could improve the performance of an LNT. Thus, on-board hydrogen generation tests were done with an unoptimized catalyst on a flow bench set-up to investigate whether hydrogen can be generated on-board a diesel vehicle with typical diesel exhaust conditions. The following trends were observed:

- The DOC temperature was the most significant parameter for on-board hydrogen generation with no hydrogen generated below initial DOC temperatures of 275°C while over 0.8% of hydrogen was generated at initial DOC temperatures exceeding 350°C
- Increasing the hourly space velocity from 75,000 to 115,000 increased the peak DOC temperature which led to an improvement in hydrogen yield from 1006 ppm to 5799 ppm
- Lengthening the fuel injection duration from ten to fifteen seconds resulted in higher DOC temperatures and increased hydrogen yield per gram of injected fuel

It was concluded in the hydrogen generation tests that the DOC temperature was a significant factor for hydrogen production. However, on-board a vehicle, the DOC could be exposed to low exhaust gas temperatures at which hydrogen generation could be ineffective. A flow reversal hydrogen reformer was proposed for mitigating the effects of the exhaust gas temperature on the DOC temperature. Numerical and empirical tests were carried out to compare the temperature response of a unidirectional flow system, a flow reversal system, and a flow reversal system with adaptive control. In the numerical investigation it was found that:

- The flow reversal system maintained 40% of the monolith above 300°C after 30 minutes of exposure to cold feed gas (at 200°C) while the unidirectional flow monolith was entirely cooled down below 220°C after 80 seconds of exposure
- The unidirectional flow monolith was able to heat up faster than a flow reversal monolith when exposed to hot feet gas
- An adaptive control strategy was shown to improve the heating response of a flow reversal monolith and to be able to maintain the monolith within a desirable temperature range

Subsequent empirical tests were done to compare the temperature response of a flow reversal DOC monolith and a unidirectional flow DOC monolith exposed to a hot feed gas. In general, the empirical tests confirmed the numerical trends.

7.2 Suggestions for Future Work

The following investigations are suggested for providing further insight into each of the studied topics.

- Investigate the performance of a long breathing LNT integrated with a diesel engine to get a more direct comparison between the long breathing LNT and other NOx reduction strategies such as a conventional LNT and low temperature combustion
- Optimize the regeneration strategy of the long breathing LNT
- Study the effects of different fuel blends on the long breathing LNT performance (e.g. biofuels)

- Integrate on-board hydrogen generation with a long breathing LNT to explore the potential benefits, such as improved NOx regeneration efficiency, of hydrogen on the long breathing LNT
- Validate the benefits of adaptive control flow reversal with empirical tests
- Combine adaptive control flow reversal on-board hydrogen generation with a long breathing LNT on a diesel test engine set-up and study the performance of the combined system
- Compare the performance of a long breathing LNT, on-board hydrogen generation with a long breathing LNT, and flow reversal on-board hydrogen generation with a long breathing LNT to determine the optimal system design

REFERENCES

1. Parks, J., West, B., Swartz, M., and Huff, S., "Characterization of Lean NOx Trap Catalysts with In-Cylinder Regeneration Strategies," SAE 2008-01-0448, 2008, doi:10.4271/2008-01-0448.
2. Yao, M., Zhang, Q., Liu, H., Zheng, Z., Zhang, P., Lin, Z., Lin, T., and Shen, J., "Diesel Engine Combustion Control: Medium or Heavy EGR?," SAE 2010-01-1125, 2010, doi: 10.4271/2010-01-1125.
3. Koči, P., Plat, F., Stepanek, J., Bartova, S. et al., "Global Kinetic Model for the Regeneration of NOx Storage Catalyst with CO, H_2 and C_3H_6 in the Presence of CO_2 and H2O," *Catalysis Today* **147S:**S257-S264, 2009, doi:10.1016/j.cattod.2009.07.036.
4. Monroe, D.R, and Li, W., "Desulfation Dynamics of NOx Storage Catalysts," SAE 2002-01-2886, 2002, doi:10.4271/2002-01-2886.
5. Johnson, T.V., "Diesel Emission Control in Review," SAE 2011-01-0304, 2011, doi: 10.4271/2011-01-0304.
6. Johnson, T.V., "Diesel Emission Control in Review," SAE 2009-01-0121, 2009, doi:10.4271/2009-01-0121.
7. US Department of Transportation, "Recent Examinations of Mobile Source Air Toxics: Change in Heavy-Duty Truck Emission Standards, 1988 – 2010," http://www.fhwa.dot.gov/environment/air_quality/air_toxics/research_and_analysis/mobile_source_air_toxics/index.cfm, May 2010.

8. Kitano, K., Nishiumi, R., Tsukasaki, Y., Tanaka, T., and Morinaga, M., "Effects of Fuel Properties on Premixed Charge Compression Ignition Combustion in a Direct Injection Diesel Engine," SAE 2003-01-1815, 2003, doi:10.4271/2003-01-1815.

9. de Ojeda, W., Bulicz, T., Han, X., Zheng, M., and Cornforth, F., "The Impact of Fuel Properties on Diesel Low Temperature Combustion," SAE 2011-01-0329, 2011, doi:10.4271/2011-01-0329.

10. Hountalas, D.T., Kouremenos, D.A., Binder, K.B., Schwarz, V., and Mavropoulos, G.C., "Effects of Injection Pressure on the Performance and Exhaust Emissions of a Heavy Duty DI Diesel Engine," SAE 2003-01-0340, 2003, doi:10.4271/2003-01-0340.

11. Hu, H., Reuter, J., Yan, J., and McCarthy, J., "Advanced NOx Aftertreatment System and Controls for On-highway Heavy Duty Diesel Engines," SAE 2006-01-3552, 2006, doi:10.4271/2006-01-3552.

12. Zannis, T.C., Hountalas, D.T., Papagiannakis, R.G., and Levendis, Y.A., "Effect of Fuel Chemical Structure and Properties on Diesel Engine Performance and Pollutant Emissions: Review of the Results of Four European Research Programs," SAE 2008-01-0838, 2008, doi:10.4271/2008-01-0838.

13. Tatur, M., Koehler, E., Laermann, M., Tomazic, D., Holland, T., Robinson, D., Dowell, J., and Price, K., "Lean NOx Trap for Heavy-Duty On-road Applications – A Feasible Alternative?," SAE 2007-01-4179, 2007, doi:10.4271/2007-01-4179.

14. Zheng M. and Reader, G.T., "Energy Efficiency Analyses of Active Flow Aftertreatment Systems for Lean Burn Internal Combustion Engines," *Energy Conversion and Management* **45**(15-16):2473-2493, 2004,

doi:10.1016/j.enconman.2003.11.006.

15. Burch, R. and Coleman, M., "An Investigation of Promoter Effects in the Reduction of NO by H2 under Lean-burn Conditions," *Journal of Catalysis* **208**(2):435-447, 2002, doi:10.1006/jcat.2002.3596.
16. Eränen, K., Klingstedt, F., Arve, K., Lindfors, L., and Murzin, D.Y., "On the Mechanism of the Selective Catalytic Reduction of NO with Higher Hydrocarbons over a Silver/Alumina Catalyst," *Journal of Catalysis* **227**(2):328-343, 2004, doi:10.1016/j.jcat.2004.07.026.
17. West, B., Huff, S., Parks, J., Lewis, S. et al., "Assessing Reductant Chemistry During In-Cylinder Regeneration of Diesel Lean NOx Traps," SAE 2004-01-3023, 2004, doi:10.4271/2004-01-3023.
18. Kong, Y., Crane, S., Patel, P., and Taylor, B., "NOx Trap Regeneration with an On-Board Hydrogen Generation Device," SAE 2004-01-0582, 2004, doi:10.4271/2004-01-0582.
19. Tsolakis, A. and Megaritis, A., "Catalytic Exhaust Gas Fuel Reforming for Diesel Engines—Effects of Water Addition on Hydrogen Production and Fuel Conversion Efficiency," *International Journal of Hydrogen Energy* **29**(13):1409-1419, 2004, doi:10.1016/j.ijhydene.2004.01.001.
20. Tsolakis, A., Megaritis, A., and Yap, D., "Application of Exhaust Gas Fuel Reforming in Diesel and Homogeneous Charge Compression Ignition (HCCI) Engines Fuelled with Biofuels," *Energy* **33**(3):462-470, 2008, doi:10.1016/j.energy.2007.09.011.

21. Tsolakis, A., Megaritis, A., and Wyszynski, M.L., "Low Temperature Exhaust Gas Fuel Reforming of Diesel Fuel," *Fuel* **83**(13):1837-1845, 2004, doi:10.1016/j.fuel.2004.03.012.

22. Holladay, J.D., Hu, J., King, D.L., and Wang, Y., "An Overview of Hydrogen Production Technologies," *Catalysis Today* **139**(4):244-260, 2009, doi:10.1016/j.cattod.2008.08.039.

23. Kang, I. and Bae, J., "Autothermal Reforming Study of Diesel for Fuel Cell Application," *Journal of Power Sources* **159**(2):1283-1290, 2006, doi:10.1016/j.jpowsour.2005.12.048.

24. Parvary, M., Jazayeri, S.H., Taeb, A., Petit, C., and Kiennemann, A., "Promotion of Active Nickel Catalysts in Methane Dry Reforming Reaction by Aluminum Addition," *Catalysis Communications* **2**(11-12):357-362, 2001, doi:10.1016/S1566-7367(01)00060-7.

25. Joo, O.S. and Jung, K.D., "CH_4 Dry Reforming on Alumina-Supported Nickel Catalyst," *Bull. Korean Chem. Soc.* **23**(8):1149-1153, 2002.

26. Liu, B., Hayes, R.E., Checkel, M.D., Zheng, M., and Mirosh, E., "Reversing Flow Catalytic Converter for a Natural Gas/Diesel Dual Fuel Engine," *Chemical Engineering Science* **56**(8):2641-2658, 2001, doi:10.1016/S0009-2509(00)00535-2.

27. Boreskov, G.K. and Matros, Y.S., "Flow Reversal of Reaction Mixture in a Fixed Catalyst Bed – A Way to Increase the Efficiency of Chemical Processes," *Applied Catalysis* **5**(3):337-343, 1983, doi:10.1016/0166-9834(83)80161-4.

28. Poulston, S. and Rajaram, R., "Regeneration of NOx Trap Catalysts," *Catalysis Today* **81**(4):603-610, 2003, doi:10.1016/S0920-5861(03)00158-5.

29. Centi, G., Arena, G.E. and Perathoner, S., "Nanostructured Catalysts for NOx Storage-reduction and N_2O Decomposition," *Journal of Catalysis* **216**(1-2):443-454, 2003, doi:10.1016/S0021-9517(02)00072-6.

30. Fornasari, G., Trifiro, F., Vaccari, A., Prinetto, F., Ghiotti, G. and Centi, G., "Novel Low Temperature NOx Storage-reduction Catalysts for Diesel Light-duty Engine Emissions based on Hydrotalcite Compounds," *Catalysis Today* **75**(1-4):421-429, 2002, doi:10.1016/S0920-5861(02)00092-5.

31. Tsolakis, A. and Golunski, S.E., "Sensitivity of Process Efficiency to Reaction Routes in Exhaust-gas Reforming of Diesel Fuel," *Chemical Engineering Journal* **117**(2):131-136, 2006, doi:10.1016/j.cej.2005.12.017.

32. Abu-Jrai, A., Tsolakis, A., Theinnoi, K., Megaritis, A., and Golunski, S.E., "Diesel Exhaust-gas Reforming for H_2 Addition to an Aftertreatment Unit," *Chemical Engineering Journal* **141**(1-3):290-297, 2008, doi:10.1016/j.cej.2007.12.028.

33. Algieri, A., Amelio, M., and Morrone, P., "A Numerical Analysis of Energetic Performances of Active and Passive Aftertreatment Systems," *International Journal of Energy Research* **33**(7):696-708, 2009, doi:10.1002/er.1505.

34. Jeftić, M., "Orifice Flow Meter Design," Clean Diesel Engine Laboratory Internal Report: 1-60, 2009.

APPENDIX A: ORIFICE FLOW METER

The orifice flow meter is one of several flow meters categorized as differential pressure flow meters. These meters function on the principle of creating a restriction in the fluid flow which causes a change in the flow area and in the pressure of the fluid. The pressure change can then be used to calculate the flow rate of the fluid. Examples of differential pressure meters include Venturi meters, orifice flow meters, and flow nozzles.

The main components of an orifice flow meter are the upstream and the downstream piping, the orifice plate, and the pressure taps. Upstream of the orifice, enough piping should be provided to allow the formation of fully developed turbulent flow. Once the flow reaches the orifice plate, the plate creates a flow restriction, causing a change in the flow area and creating a pressure difference. Downstream of the orifice plate, the flow will continue to converge due to the momentum of the flow until the minimum flow area is reached, called the vena contracta. The flow will then diverge but the pressure will not return to its original, upstream value due to permanent pressure losses. The pressure change across the orifice plate can then be used to calculate the flow rate of the fluid according to the Bernoulli equation (Equation A-1).

$$p_1 + \frac{\rho V_1^2}{2} + \gamma z_1 = p_2 + \frac{\rho V_2^2}{2} + \gamma z_2 \qquad \text{(A-1)}$$

Where:

p – Fluid Pressure (Pa)

V – Fluid Velocity (m/s)

ρ – Fluid Density (kg/m^3)

γ – Specific Weight (N/m^3)

z – Altitude (m)

The Bernoulli equation can be re-arranged and substitutions can be made to obtain an expression for the mass flow rate in terms of the pressure change as shown in Equation A-2.

$$q_m = \frac{1}{\sqrt{1-\beta^2}} \frac{\pi}{4} d^2 \sqrt{2\Delta p \rho_1} \tag{A-2}$$

Where:

q_m – Mass Flow Rate (kg/s)

d – Orifice Diameter (m)

β – Ratio of the Orifice Diameter (d) to the Internal Pipe Diameter (D)

Δp – Pressure Drop (Pa)

ρ_1 – Upstream Fluid Density (kg/m^3)

Finally, various standards have modified this equation by introducing coefficients which account for compressibility and viscosity effects. One of these is the ISO 5167-2:2003 standard which utilizes the discharge coefficient (C) and the expansibility factor (ε) as shown in Equation A-3. This equation is only applicable for single-phase, homogenous, Newtonian fluids.

$$q_m = \frac{C}{\sqrt{1-\beta^2}} \varepsilon \frac{\pi}{4} d^2 \sqrt{2\Delta p \rho_1} \tag{A-3}$$

Equation A-3, along with the ISO 5167-2:2003 standard was used to design the orifice flow meter. A u-tube manometer was chosen as the device for measuring the pressure drop. The desired pressure drop range was chosen as 10 cm to 140 cm of water column due to the readability and space restrictions. Thus, for the selected pressure drop range, six different orifice plates with different orifice sizes were designed to be able to measure flow rates ranging from 4 g/s to 90 g/s. A summary is shown in Figure A.1.

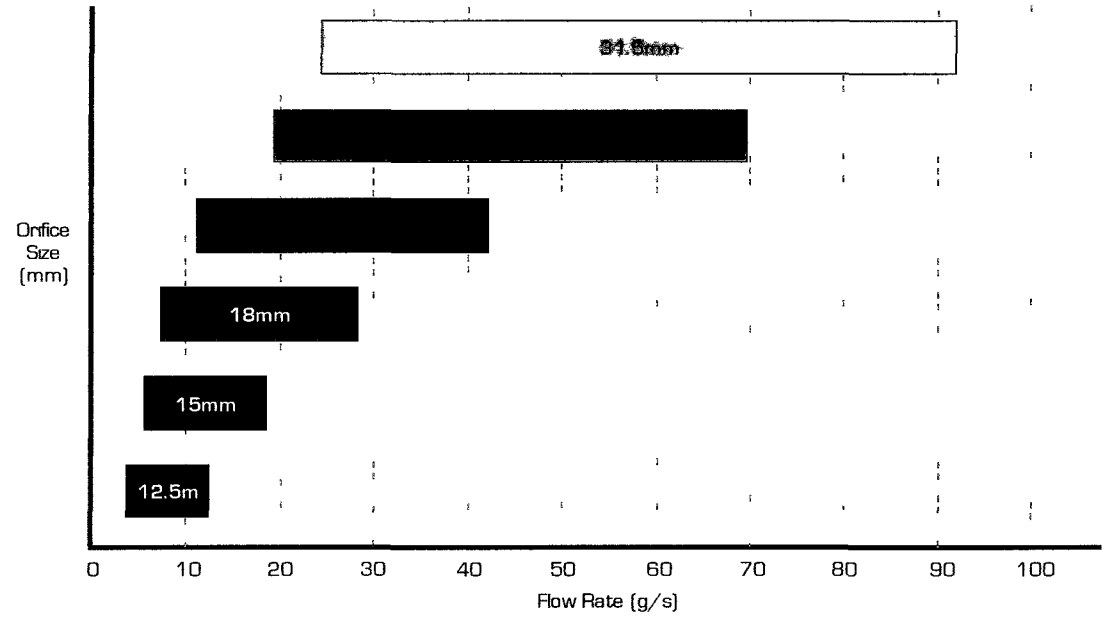

Figure A.1: Six Orifice Plates Designed to Measure a Range of Flow Rates

A drawing of the overall orifice flow meter system was made in Autodesk Mechanical Desktop and is shown in Figure A.2 and Figure A.3. A photo of the completed and machined orifice flow meter is shown in Figure A.4. Detailed information about the design of this orifice flow meter can be found in [34].

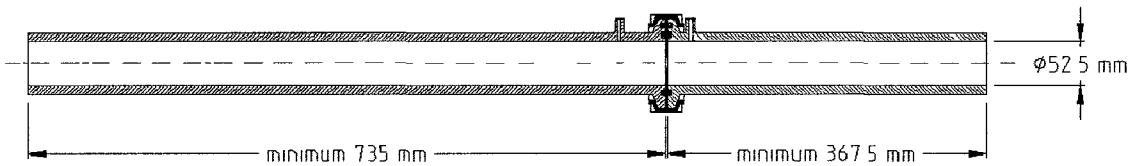

Figure A.2: Mechanical Desktop Cross-section View of the Orifice Flow Meter

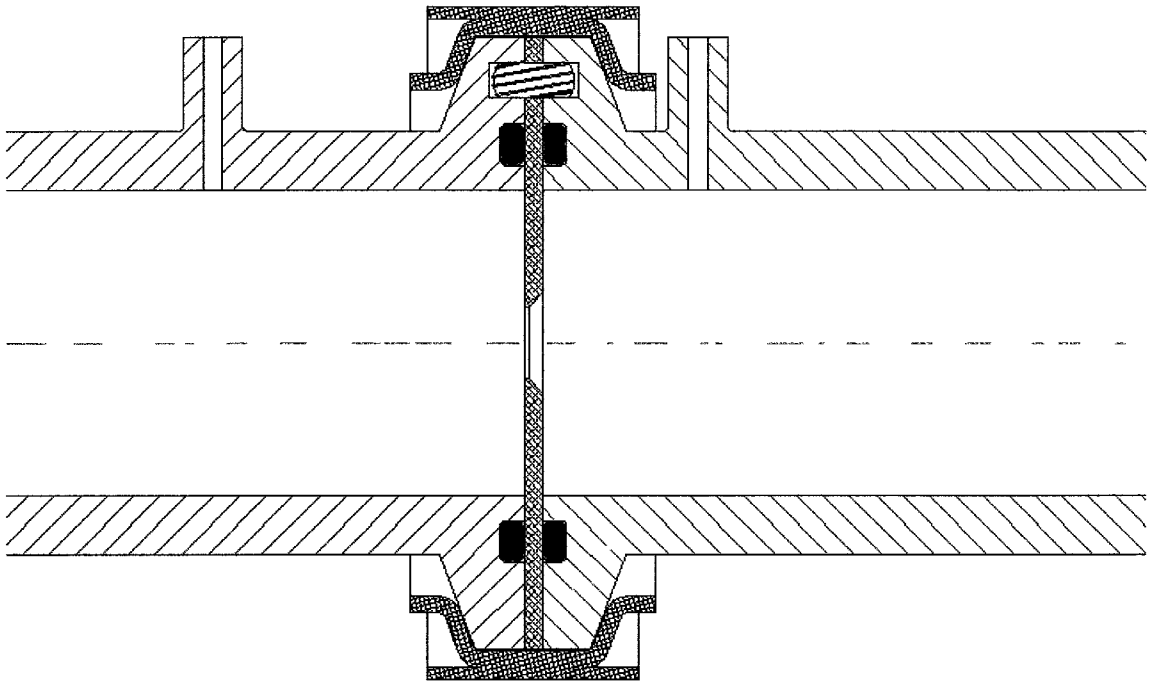

Figure A.3: Cross-section Close-up of the Orifice Flow Meter

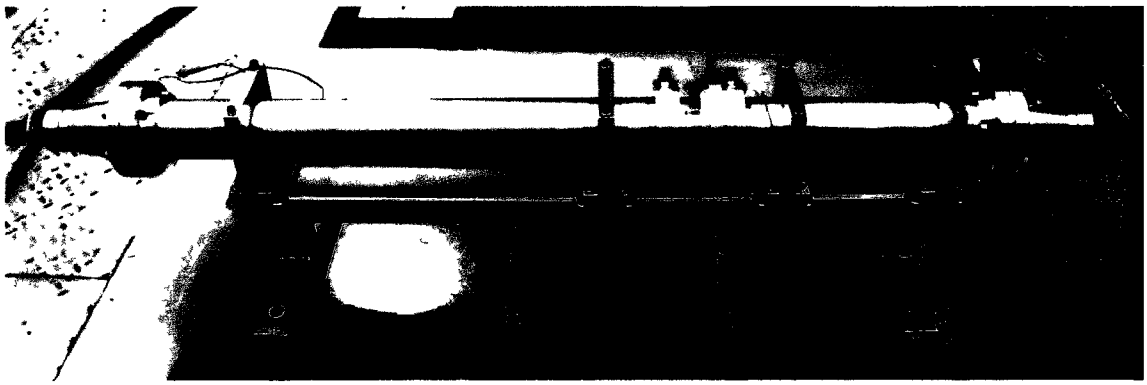

Figure A.4: Orifice Flow Meter at the Clean Diesel Engine Laboratory

APPENDIX B: FLOW REVERSAL CODE

```
#include <iostream>
#include <fstream>
#include <math h>
#include <windows h>
#include <stdlib h>

using namespace std,

int main() {


int nodes=305,totaltimesteps=182000, treset=101, savefreq=500,

float timestep=0 01, nodestep,

float Tgas_initial=400, Tsolid_initial=200, Tgas_m=300,

float ks=11 7, cs=800, densitys=1700,

float  cg=1075, densityg, Rg=287, mug=0 00003388, kg=0 0524, pg=101375,

float vg, mg_all=0 02, mg, hg, reynolds, nusselt, prandtl, friction, pressure_drop,

float dh, t=0 00035, dia_monolith=0 1, numcells, cpsi=400, cpsim, areas, areaf, ch, length=0 304,

float alpha, beta, delta, lambda,

float powersupply=500  qmax  qgen,

float temp, Tmax  Tmin,

int flowreversaltime=1000, reversal=2, count=0, arraycount=0,

float T[nodes][treset], Tgas[nodes][treset],


ofstream c_file ( "ad7 20gs txt", ios  app ),



nodestep=length/(nodes-1),
cout<<"\nlength="<<length,
cout<<"\nnode step="<<nodestep,

cpsim=cpsi*1550,
numcells=floor(cpsim*dia_monolith*dia_monolith/4*3 14),
cout<<"\nNumber of Cells="<<numcells,
dh=sqrt(3 14*dia_monolith*dia_monolith/4/numcells)-t,
cout<<"\ndh="<<dh,
ch=4*dh,
cout<<"\nch="<<ch,
areaf=dh*dh,
cout<<"\nflow area="<<areaf,
areas=(2*dh*t)-(t*t),
cout<<"\nsolid area="<<areas,


alpha=ks/(cs*densitys),
cout<<"\nalpha="<<alpha,
beta=ch*timestep/densitys/areas/cs,
cout<<"\nbeta="<<beta,
delta=timestep/densitys/cs/areas/nodestep,
cout<<"\ndelta="<<delta,
lambda=alpha*timestep/(nodestep*nodestep),
cout<<"\nlambda="<<lambda,
```

```
densityg=pg/Rg/(Tgas_m+273 15),
cout<<"\ngas density="<<densityg,
mg=mg_all/numcells,
vg=mg/densityg/areaf,
reynolds=vg*densityg*dh/mug,
prandtl=(cg*mug)/kg,

if (reynolds<=2300)
{
  nusselt=3 66+((0 065*dh/length*reynolds*prandtl)/(1+0 04*pow((dh/length*reynolds*prandtl),2/3))),
  friction=64/reynolds,
}
else
{
  if (Tgas_initial<Tsolid_initial)
    nusselt=(pow(0 023*reynolds,0 8))*(pow(prandtl,0 4)),
  else
    nusselt=(pow(0 023*reynolds,0 8))*(pow(prandtl,0 3)),
  friction=pow((0 790*log(reynolds)-1 64),-2),
}
pressure_drop=friction*length/dh*densityg*vg*vg/2/1000,
hg=nusselt*kg/dh,
cout<<"\nPressure Drop="<<pressure_drop,
cout<<"\nPrandtl="<<prandtl,
cout<<"\nGas Velocity="<<vg,
cout<<"\nReynolds="<<reynolds,
cout<<"\nNusselt="<<nusselt,
cout<<"\nFriction Factor="<<friction,
cout<<"\nmg_all="<<mg_all,
cout<<"\nmg="<<mg,
cout<<"\nhg="<<hg,


qgen=powersupply/numcells/(nodes-1),
cout<<"\nq ="<<qmax


for ( int r=0  r<=nodes-1  r++ )
{
  T[r][0]=Tsolid_initial+273 15,
  if(r==0)
    Tgas[r][0]=Tgas_initial+273 15,
  else
    Tgas[r][0]=(mg*cg*Tgas[r-1][0]+hg*ch*nodestep*(T[r-1][0]-Tgas[r-1][0]))/mg/cg,
}


for (int tstep=1, tstep<=totaltimesteps, tstep++)
{


  count=count+1,


  if (flowreversaltime!=0)
  {
    if (count%flowreversaltime==0)
    {

      reversal=reversal+1,


      for(int c=0, c<((nodes+(nodes%2))/2)-1 , c++ )
      {
        temp=T[c][tstep-1],
        T[c][tstep-1]=T[nodes-1-c][tstep-1],
        T[nodes-1-c][tstep-1]=temp,
        temp=Tgas[c][tstep-1],
        Tgas[c][tstep-1]=Tgas[nodes-1-c][tstep-1],
        Tgas[nodes-1-c][tstep-1]=temp,
```

```
        }


        Tgas[0][tstep-1]=Tgas_initial+273.15;
      }
    }


    if (tstep%treset==0)
    {


      for ( int r=0; r<=nodes-1 ; r++ )
      {
        T[r][0]=T[r][tstep-1];
        Tgas[r][0]=Tgas[r][tstep-1];
      }

      totaltimesteps=totaltimesteps-treset+1;

      tstep=1;

      arraycount=arraycount+1;
    }


    for ( int m=0; m<=nodes-1 ; m++ )
    {









      if(m==0)
      {
        Tgas[m][tstep]=Tgas_initial+273.15;
        T[m][tstep]=lambda*(T[m+2][tstep-1]-2*T[m+1][tstep-1])+(1+lambda-hg*beta)*T[m][tstep-1]+hg*beta*Tgas[m][tstep-
1]+delta*qgen;
      }
      else if(m==(nodes-1))
      {
        T[m][tstep]=lambda*(T[m-2][tstep-1]-2*T[m-1][tstep-1])+(1+lambda-hg*beta)*T[m][tstep-1]+hg*beta*Tgas[m][tstep-
1]+delta*qgen;
        Tgas[m][tstep]=(hg*ch*nodestep/mg/cg*(T[m-1][tstep]-Tgas[m-1][tstep]))+Tgas[m-1][tstep];
      }
      else
      {
        T[m][tstep]=lambda*(T[m+1][tstep-1]+T[m-1][tstep-1])+(1-2*lambda-hg*beta)*T[m][tstep-1]+hg*beta*Tgas[m][tstep-
1]+delta*qgen;
        Tgas[m][tstep]=(hg*ch*nodestep/mg/cg*(T[m-1][tstep]-Tgas[m-1][tstep]))+Tgas[m-1][tstep];
      }
    }


    if(count%savefreq==0)
    {
      c_file<<"Time = "<<count*timestep<<"(s)\n";

      if (reversal%2==0)
      {
        for (int aa=0;aa<=nodes-1;aa++)
        {
          c_file<<T[aa][tstep]-273.15<<"\n";
        }
      }
```

```
    else
    {
      for (int aa=nodes-1;aa>=0;aa--)
      {
        c_file<<T[aa][tstep]-273.15<<"\n";
      }
    }
  }


  Tmax=T[0][tstep];
  Tmin=T[0][tstep];

  for (int m=1; m<=nodes-1 ; m++)
  {
    if (T[m][tstep]>Tmax)
      Tmax=T[m][tstep];
    if (T[m][tstep]<Tmin)
      Tmin=T[m][tstep];
  }


  if (Tmax>725)
    flowreversaltime=0;
  else if(Tmin<575)
    flowreversaltime=0;
  else
    flowreversaltime=1000;

}


c_file.close();
}
```

VITA AUCTORIS

Marko Jeftić was born in Tuzla, Yugoslavia in 1985. In early childhood, he immigrated with his parents to Windsor, Canada. After completing his high school studies at Riverside Secondary School in Windsor, Ontario, he attended the University of Windsor's mechanical engineering program. He received his Bachelor's Degree of Applied Science with Distinction in 2007. He is currently a candidate for the Master's Degree in Applied Science at the University of Windsor with research focus on diesel deNOx after-treatment and diesel post injection combustion.

LIST OF PUBLICATIONS

Papers in Refereed Journals

1. **Jeftić, M.**, Yu, S., Han, X., Reader, G.T., Wang, M. and Zheng, M., "Effects of Postinjection Application with Late Partially Premixed Combustion on Power Production and Diesel Exhaust Gas Conditioning," Journal of Combustion, **2011**:9 pages, 2011, doi:10.1155/2011/891096.

Papers in Refereed Conference Proceedings

1. **Jeftić, M.**, Asad, U., Han, X., Xie, K., Yu, S., Wang, M. and Zheng, M., "An Analysis of the Production of Hydrogen and Hydrocarbon Species by Diesel Post Injection Combustion," Proceedings of the ASME 2011 Internal Combustion Engine Division Fall Technical Conference, Morgantown, WV, USA, October 2011, ICEF2011-60135, 2011.
2. **Jeftic, M.**, Yu, S., Chen, X., Xu, X., Wang, M. and Zheng, M., "Diesel Active-Flow Aftertreatment Control on a Heated Flow Bench," Proceedings of the ASME 2010 International Mechanical Engineering Congress & Exposition, Vancouver, BC, Canada, November 2010, IMECE2010-39057, 2010.
3. Asad, U., Mendoza, A., Xie, K., **Jeftic, M.**, Wang, M. and Zheng, M., "Speciation Analysis of Light Hydrocarbons and Hydrogen Production during Diesel Low Temperature Combustion," Proceedings of the ASME 2011 Internal Combustion Engine Division Fall Technical Conference, Morgantown, WV, USA, October 2011, ICEF2011-60130, 2011.

4. Yu, S., Xie, K., Han, X., **Jeftic, M.**, Gao, T. and Zheng, M., "A Preliminary Study of the Spark Characteristics for Unconventional Cylinder Charge with Strong Air Movement," Proceedings of the ASME 2011 Internal Combustion Engine Division Fall Technical Conference, Morgantown, WV, USA, October 2011, ICEF2011-60132, 2011.

Papers in Non-refereed Conference Proceedings

1. **Jeftic, M.**, Asad, U., Tjong, J., Wang, M., Reader, G.T. and Zheng, M., "Ultra-low NOx with Diesel Enhanced Premixed Combustion and a Long-breathing Lean NOx Trap Strategy," Proceedings of the Emissions 2011 Conference, Ann Arbor, MI, USA, June 2011.
2. **Jeftic, M.**, Meng, Z., Xu, X. and Zheng, M., "Heated Flow Bench Test for Aftertreatment Control," Proceedings of Combustion Institute – Canadian Section Spring Technical Meeting, Ottawa, ON, Canada, May 2010.